UNIVERSITÀ DI PARMA

UNIVERSITA' DEGLI STUDI DI PARMA

DOTTORATO DI RICERCA IN
"SCIENZE DELLA TERRA"

CICLO XXXII

Field and experimental investigations on the Monte Marine Fault (Central Apennines, Italy): constraints on the evolution of a seismogenic fault zone in carbonate rocks

Coordinatore:
Chiar.mo Prof. Mario Tribaudino

Tutori:
Chiar.mo Prof. Fabrizio Balsamo
Chiar.mo Prof. Giulio Di Toro

Dottorando: Dott.ssa Silvia Cortinovis

Anni 2016/2018

A chi mi incoraggia sempre a credere in me stessa.

Table of contents

Riassunto

Questa tesi è una collezione di lavori legati dal comune obiettivo di investigare la formazione e l'evoluzione di zone di faglia sismogenetiche in rocce carbonatiche attraverso lo studio della faglia di Monte Marine (MMF) e di campioni di rocce di faglia provenienti dalla faglia di Fiamignano, in Appennino Centrale.

Questa tesi consta di tre capitoli principali e si apre con uno studio metodologico volto alla revisione delle più comuni tecniche analitiche utilizzate per la caratterizzazione delle rocce di faglia in carbonati. In questo studio, pubblicato sulla rivista *Journal of Structural Geology*, si analizza il modo in cui le procedure analitiche influenzano il calcolo della dimensione frattale in rocce di faglia in carbonati, prendendo in esame dei campioni raccolti lungo il piano di faglia di Fiamignano. Alla fine del capitolo vengono fornite delle line guida generali per la caratterizzazione delle rocce di faglia in carbonati.

Il secondo capitolo di questa tesi si focalizza sull'analisi dell'architettura strutturale e delle proprietà petrofisiche delle rocce di faglia affioranti nel blocco di letto della Faglia di Monte Marine (MMF), in provincia de L'Aquila, attraverso analisi di terreno e di laboratorio. Lo scopo di questo studio è capire la formazione e l'evoluzione della zona di faglia attraverso l'interpretazione delle eterogeneità strutturali e delle proprietà microstrutturali delle rocce di faglia, mediante mappatura sul terreno e caratterizzazione in laboratorio delle proprietà granulometriche e morfometriche di cataclasiti e brecce. Il risultato finale di questo studio consiste in un modello evolutivo che spiega la formazione di ingenti volumi di rocce brecciate in un'alternanza di fasi di *fault creeping* e di rottura cosismica durante il ciclo sismico.

Il terzo ed ultimo capitolo di questa tesi riporta i risultati degli esperimenti frizionali condotti con l'apparato SHIVA (*Slow to High Velocity Apparatus*, INGV, Roma) su un *gouge* naturale raccolto lungo la MMF. Gli esperimenti sono stati condotti a diverso slip rate (1 m/s e 0.001 m/s) e sforzo normale efficace (1 MPa e 5 MPa) in condizioni *dry* (usando Argon come fluido di poro) e *wet* (usando acqua come fluido di poro). Lo scopo di questo lavoro è stato quello di capire il ruolo dei fluidi durante la rottura cosismica e applicare queste conoscenze al caso studio della MMF. I risultati di questo lavoro mostrano che i meccanismi di indebolimento dinamico ad es. per formazione di nanoparticelle e pressurizzazione termica del fluido) avvengono a velocità cosismiche e specialmente in presenza di acqua. La comparazione tra microstrutture prodotte sperimentalmente e microstrutture osservate

sul terreno mostra come la rottura cosismica lungo la Faglia di Monte Marine sia avvenuta prevalentemente in condizioni *dry*.

Abstract

This thesis is a collection of works linked by the common purpose of investigating the formation and evolution of seismogenic fault zones in carbonate rocks through the study of the Monte Marine Fault (MMF), a seismogenic fault located in the central Apennines (Italy).

This thesis is organized in three chapters. It starts with a methodological study that consists of a review of the most common techniques used for the characterization of carbonate fault rocks. In this study, new methodologies for the characterization of granular/poorly cohesive materials are also presented. The aim of this study is to compare 2D multi-scale image analysis on coherent samples with results from 3D laser granulometry and 3D optical granulometry on loose materials to test the influence of analytical procedure on the calculation of fractal dimension. The final results of this study prove that analytical procedures influence the calculation of fractal dimension in faulted carbonates. Guidelines for the characterization of carbonate materials are also provided.

The second chapter of this thesis focuses on the analysis of the structural architecture and petrophysical properties of fault rocks along the MMF, through fieldwork and laboratory analyses. The aim of this study is to understand the formation and evolution of the fault rocks along the Monte Marine fault zone by studying heterogeneities in structural architecture and microstructural properties of fault rocks with field mapping, and grain size and shape characterization of faulted materials and *in situ* shattered rocks. The final result of this study consists of an evolutionary model that presents alternated phases of fault creeping and seismic rupture that occur during the seismic cycle.

The third and last chapter of this thesis reports the results of friction experiments performed with SHIVA (Slow to High Velocity Apparatus, INGV, Rome) on a natural fault gouge collected from the MMF. Experiments were performed at different slip rates (1 m/s and 0.001 m/s) and effective normal stress (1 MPa and 5 MPa) at both dry conditions (with argon as pore fluid) and wet conditions (with water as pore fluid). The principal aim of this work is to understand the role of fluids during the seismic rupture and apply these founding at the case of the MMF. The final results of this work show that mechanisms favoring weakening (e.g. nanoparticles formation and pore fluid pressurization) mostly occur at seismic slip velocities and especially in water. The comparison between experimentally produced microstructures and naturally produced microstructures demonstrated that seismic rupture along the MMF likely occurred in dry conditions.

1 Aim and introduction

1.1 State of the art

1.1.1 Active faults and seismicity

Seismicity causes significant issues in many active regions around the world due to the presence of seismogenic and active faults, whose activity and related destructiveness are still unpredictable and cause every year several human life losses and serious damage to buildings and infrastructures. The most powerful earthquakes on Earth develop along the Circum-Pacific belt, where the occurrence of particular geodynamic conditions (oceanic subduction and associated mountain belts) generate structural instability and related earthquakes up to M_w9. These earthquakes are also able to trigger tsunami on the surrounding coasts thus increasing the overall potential destructiveness and dangerousness of the phenomenon itself. Seismogenic and active faults recognizable in various geological settings (i.e. contractional and extensional regimes) develop in sedimentary, magmatic and metamorphic rocks. Continental crust, made by prevalent quartz and feldspar, can display a brittle behavior responsible for earthquake rupture down to 15-20 km depth only when the geothermic gradient and the heat flow are particularly low (< 20°C/km and < 55 mW/m^2 respectively). Seismogenic and active faults have different length, from few tens of kilometers (e.g. faults in the Central Apennines) to several hundreds of kilometers (e.g. San Andreas Fault) and more or less complex shapes depending on the tectonic history of the area.

Almost all the most important seismically active regions around the world have been recognized and partially studied. Nevertheless, earthquake rupture can not be predicted and arrested. What we can concretely do to protect population and reduce damage and human life loss is constructing earthquakes-proof buildings in seismically active areas and in the regions where earthquakes occurred in the past. In fact, every fault is characterized by a peculiar recurrence interval, thus the study of past seismicity could help to predict or hypothesize other fault reactivations in the future. Basing on these assumptions, it is fundamental to acquire a deep knowledge on the formation and evolution of active and seismogenic faults and monitor them continuously in order to understand the mechanisms and effects of fault reactivation and, where possible, the premonitory signals of new earthquake ruptures in the future. To gain this purpose, it is necessary to study seismogenic faults using a multi-disciplinary and multi-scale approach that help to get several information on seismic rupture mechanisms and on the effects of earthquake along seismogenic and active fault zones. The use of different methodologies including geological, geophysical and geochemical

analyses (at different scales), together with experimental studies at monitored conditions, allows to unravel the deformation mechanisms associated with the formation and evolution of seismogenic fault zones. For example, field mapping can help to describe the structural architecture of faults. Kinematic analysis can help to reconstruct the geological history of faults through the observation of kinematic indicators preserved along slip surfaces. Geophysical surveys can be useful to investigate fault structure at depth, while photogrammetry and laser scanner help to reconstruct 3D structure of fault zones and thus elaborate geostatistical models to study fracture network and permeability properties.

In the Mediterranean area, earthquakes develop mainly in thick sedimentary sequences and thick carbonate successions (preferentially carbonate and dolomitic rocks) at shallow depth (down to 15-20 km of depth), where crust is characterized by brittle behaviour. Even when the mainshock is located in the rock basement, the seismic rupture propagates into the shallower carbonate sequences and its effects are strongly influenced by the rheology of the transmitting material. Moreover, most of the foreshocks and aftershocks develop and propagate directly into the shallow levels corresponding to carbonate successions (Fondriest et al., 2012; Demurtas et al., 2016). In Italy, the major seismogenic sources are hosted in carbonate rocks and produce earthquakes up to Mw 6-6.5 (i.e. Friuli earthquake, 1976, Mw = 6.4; Colfiorito, 1997, Mw = 5.7-6; Emilia, 2012, Mw = 6.0; L'Aquila, 2009, Mw =6.1, Amatrice, 2016, Mw = 6.0) (Tondi and Cello, 2003, Galli et al., 2012). Even though seismicity is widespread around the whole peninsula, the areas of Italy characterized by the highest hazard caused by the presence of high magnitude earthquakes (up to Mw 6.5) correspond to the SE Sicily, the Calabrian Arc, the neckbone of both southern and central Apennines, and the NE edge of the Friuli Region. The greatest predicted horizontal acceleration (>0.275 g) characterizes the area of the Crati Basin (North Calabria).

Recently, powerful seismic episodes destroyed the city of L'Aquila and the neighbor villages, and caused several human life losses in the central Apennines, where seismicity is well aligned in a NW-SE direction (Fig. 1) recognizable by mapping the distribution of the hypocenters of the recent earthquakes (Tondi and Cello, 2003).

The Central Apennines are characterized by a very complex seismotectonic history. During the Tortonian times, compressive tectonics originated NW-SE trending thrusts. These crustal discontinuities were partially exploited by NW-SE extensional faults formed starting from the Pliocene and bordering km-wide intermontane basins along the Apennine chain (Vezzani et al.,

2010). Extensional faults cut through Quaternary continental deposits and show spectacular carbonate bedrock fault scarps (Galadini, 1999). The stiffness of the carbonates and dolostones in the Central Apennine favors the brittle response of the rocks to the propagation of co-seismic rupture. This results in a high volume of deformed rocks due to the occurrence of high fracture density. To the North-west of the L'Aquila town, the Aterno Valley hosts series of extensional faults with sigmoidal shape. One of these faults is the Monte Marine fault, which was reactivated during the 1703 earthquake. The active fault segment is 8 km long and extends from the village of Arischia (to the SE) to the village of Barete (to the NW). This fault represents a seismic gap area in the seismic active area of the Central Apennine and presents significant volumes of shattered rocks that increase in the step-over zone near the Pizzoli village. The Monte Marine Fault together with the Fiamignano fault, another NW-SE oriented extensional and seismogenic fault located near Rieti (It), developed on partially dolomitized carbonate platform rocks and represent the study areas of this doctoral thesis.

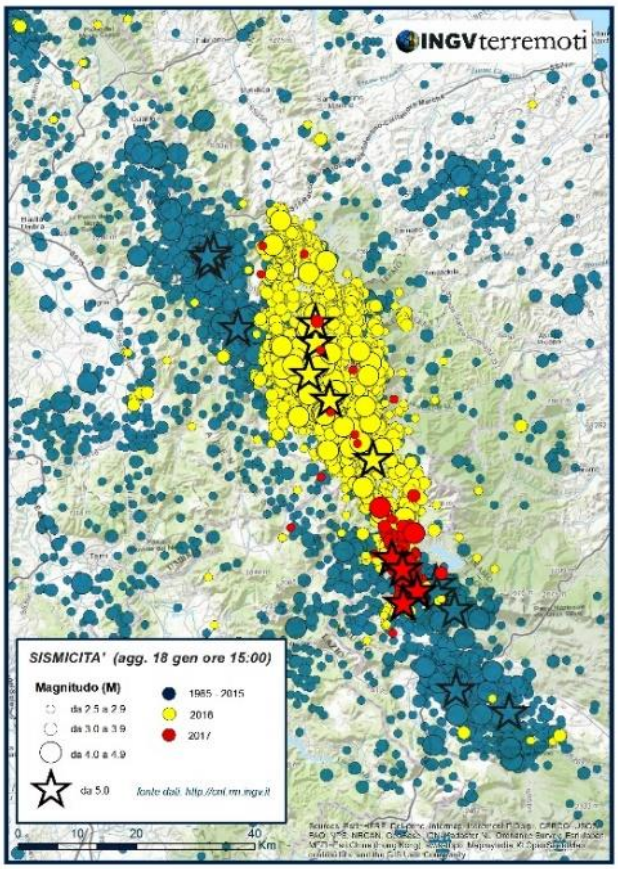

Figure 1: Map of seismicity in the Central Apennines with location of earthquakes mainshock from the 1985 to the 2017. Source: http://terremoti.ingv.it/.

1.1.2 The role of fluids along seismogenic/active fault zones

In the Central Apennines and other seismogenic fault zones, fluids play an important role to drive the earthquake rupture. The presence of fluids in seismogenic areas depends primarily on rock porosity and permeability. In case of carbonates, permeability is increased by the occurrence of a well-developed fracture network with high interconnectivity between fractures (this is also fundamental in the study of oil and gas explorations along fault zones). This situation is usually found in damage zone, where the fault-related deformation produces different sets of fractures. On the contrary, fault core usually acts as barrier or seal for cross-fault fluid flow due to the occurrence of dm- to cm- thick fault gouges and cataclasites (Agosta and Aydin, 2006; Agosta et al., 2007; Solum and Huisman, 2016).

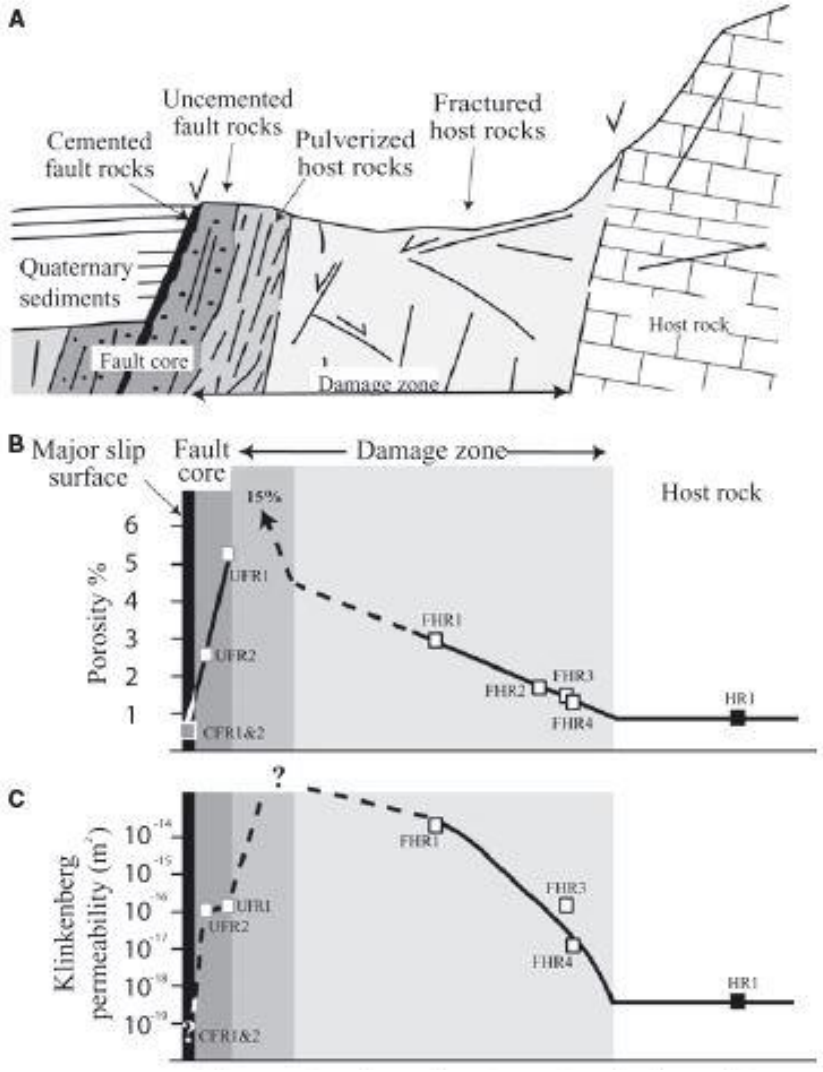

Figure 2: Porosity and permeability evolution from fault core to damage zone. From Agosta et al., 2007.

During earthquakes, transient pathways can develop in the fault core and permeability may evolve during the seismic cycle. Permeability usually increases immediately after earthquake due to the

increase of the number of fractures. Then, it usually decreases over time because of compaction. This “fault-valve behaviour” was described for the first time by Sibson (1990b and 1992) and invokes the rupture of a seal compartmentalizing high-pressure fluids during foreshock deformation, which might infiltrate through the seismic fault zone triggering the main shock (Steve Miller’s model for the Colfiorito 1997 earthquake). Seismological studies firstly proved that pore fluid increases near active faults in carbonate rocks by the study of the ratio between Vp and Vs. Even friction experiments performed in fluid-pressurized conditions on calcite gouges testified that the presence of water can facilitate earthquake nucleation by favoring fault surface lubrication (Rempe et al., 2017) and consequent weakening. It is proved that, during the Umbria-Marche and L’Aquila sequences, over-pressured fluids were present at depth (Miller et al., 2004; Di Luccio et al., 2010) and Violay et al. (2013, 2014) demonstrated, with friction experiments on carbonate gouges, that slip along carbonate bearing faults is facilitated in presence of pressurized fluids in the pore space.

1.2 Objectives and thesis structure

The general aim of this thesis is to enhance the knowledge on the formation and evolution of seismogenic faults in carbonate rocks by 1) testing the advantages and disadvantages of different analytical procedures used for the characterization of carbonate fault rock, 2) studying the Monte Marine Fault (MMF) (Central Apennines, Italy), which represents a complex seismogenic area where multiple effects of seismic rupture and fault deformation affect carbonates rocks, and 3) performing friction experiments under fluid-pressurized conditions in the laboratory of the INGV-Rome, Italy.

The comparison between different methodologies used in carbonate fault rocks was performed on carbonate samples coming from the Fiamignano Fault (Central Apennines Italy), which is a NW-SE seismogenic fault located NE of the Fiamignano Lake. Along this fault we were able to collect, from the same fault plane, a pair of representative samples characterized by different cohesion but same composition. The two samples used for our tests even experienced the same tectonic history.

The Monte Marine Fault zone is another fault developed in the Central Apennines with NW-SE orientation. The Monte Marine Fault constitutes an analogue to study how fault nucleation occurs in carbonate rocks and what kind of damage can be produce by earthquakes in shallow carbonate rocks. The comprehension of fault mechanisms, in this case, is gained by the study of the effects induced by the earthquake rupture. The MMF constitutes a seismic gap area in the recent seismic sequences of L’Aquila 2009 and Amatrice 2016. It was lastly reactivated during the 1703 seismic sequence and the reasons for the recent silent behavior still need to be understood, as well as the formation of the huge amounts of shattered material recognisable along the main fault. In this study

we used a multi-disciplinary and multi-scale approach including fieldwork investigations, laboratory analyses on representative fault rock samples, and friction experiments performed with SHIVA (INGV-Rome) (Di Toro et al., 2010) on a natural fault gouge (mixture of dolomite 80% and calcite 20%) collected from the fault. The methodological approach used in this thesis helped to better understand the formation of the MMF and define its complex structural architecture. With fieldwork, we mapped different fault rocks (i.e. ultra-cataclasites, cataclasites, proto-cataclasites and breccias), documented fault architecture in relation to inherited thrust faults, and collected structural data along the fault. We also performed petrophysical analyses to study grain size and shape distributions in fault rock samples. We used optical microscopy, scanning electron microscopy and EMPA to study evidences of co-seismic slip (e.g. truncated clasts, fluid-like structures, nanoparticles, mirror-like slip surface) (e.g. Fondriest et al., 2013). Finally, we performed friction experiments to investigate the role of fluids during fault deformation at different conditions of normal stress and pore fluid (Argon to simulate dry conditions and water to simulate wet conditions) at different slip rates (slow 0.001 m/s and fast 1 m/s rupture). The experimentally produced microstructures were compared with the natural samples collected from the fault to constrain fault deformation conditions.

This PhD thesis is organized in three main chapters linked by the common purpose to investigate the origin and the evolution of a seismogenic normal fault in carbonate rocks. This aim was gained by merging data and observations coming from different fields of study.

The first chapter concerns a methodological study that describes and compares different methodologies used in the petrophysical study of fault rocks (i.e. wet and dry laser granulometry, optical granulometry and multi-scale image analysis) following the approach described by Storti and Balsamo, 2010. This work was fundamental to recognize the most common biases encountered during characterization of carbonate fault rocks and avoid the wrong estimate of grain size and shape distribution in the samples analysed. The main conclusion of this chapter is that carbonate rocks constitute a very fragile material which is easily affected by biases induced by the analytical procedures. This means that analytical procedures constitute one of the major controls on particle size distribution in fault carbonate rocks.

The second chapter of this thesis is about the study of the structural architecture and petrophysical properties of fault rocks along the Monte Marine Fault. This study was aimed to characterize the structural architecture of the Monte Marine Fault and understand the genesis and the evolution of fault rocks, through a multi-scale and multi-disciplinary approach including fieldwork and laboratory

analyses (petrophysical characterization of loose and coherent materials). During fieldwork, we collected structural data on the main structural elements and reconstructed timing of faults basing on cross-cutting relationships. During laboratory analyses, we studied the grain size and shape distribution of fault rocks on the sample collected at progressive distance from the master fault. We also described heterogeneities along fault by performing field mapping and two geological cross-sections traced in the Barete and in the Pizzoli area, respectively. With this work, we found that the actual configuration of the Monte Marine Fault, which presents increased amounts of shattered rocks in the central areas with major structural complexity, derives from different deformation mechanisms (from rock fracturing to cataclasis) occurred during alternated episodes of fault creeping and seismic rupture.

The third chapter of this thesis presents friction experiments conducted with SHIVA (INGV-Rome) on a natural fault gouge of mixed dolomite (80%) and calcite (20%) collected from the Monte Marine Fault. This study was aimed at investigating the role of fluids at seismic (1 m/s) and sub-seismic (0.001 m/s) slip rates and different conditions of effective normal stress (1 MPa and 5 MPa). During experiments, we used water to simulate wet conditions and Argon to simulate dry conditions. For the first time, we were able to control pore fluid pressure during slip at co-seismic slip rates. This was fundamental to study the mechanisms controlling weakening along slip surfaces (e.g. thermal pressurization) at co-seismic slip rates in carbonate rocks. We also compared experimentally produced microstructures with natural samples to constrain the P-T conditions and pore fluid pressure at which deformation occurred along the MMF. The main conclusion of this work is that water can induce physic-chemical reactions (e.g. pressurization, nanoparticles formation) responsible for the weakening of faults. Nevertheless, we proved that deformation along the MMF likely occurred in absence of water.

2 Influence of analytical operating procedures on particle size distributions in carbonate cataclastic rocks

S. Cortinovis, F. Balsamo, F. Storti

S. Cortinovis, F. Balsamo, F. Storti (2019). Influence of analytical operating procedures on particle size distributions in carbonate cataclastic rocks, Journal of Structural Geology, Vol. 128, 103884 https://doi.org/10.1016/j.jsg.2019.103884.

2.1 Abstract

Fractal dimensions of fault core rocks provide a suitable tool to estimate amounts of comminution and describe processes associated with faulting, such as hydraulic sealing, and nucleation and propagation of coseismic ruptures. It is thus important to be aware of possible biases produced by different analytical procedures on given materials, to prevent unsupported interpretations of granulometric data. The aim of this paper is to minimize the method-induced variability in the calculation of fractal dimensions. We present a comparison among different 2D and 3D analytical techniques that are commonly used to calculate grain size distributions, even introducing and discussing new analytical techniques never used before in the study of fault core rocks. The studied samples are loose and coherent carbonate cataclastic rocks collected at the same field site along the Fiamignano Fault in the Central Apennines (Italy). Our results provide further support to the evidence that analytical procedures can significantly influence particle size distributions and related D-values. It follows that direct comparison between different datasets is not straightforward if rigorous analytical protocols are not systematically used and described. Guidelines for fractal analysis of carbonate fault rocks are provided.

2.2 Introduction

2.2.1 Overview and objectives

Faulting in platform carbonate rocks produces cataclastic rock localized in narrow fault cores, where most shear strain is accommodated. The spatial distribution, volume, and deformation intensity of fault core rocks depend on several factors including 1) depth of deformation, 2) host rock properties, 3) amount of displacement, 4) fault architecture and kinematic history, 5) seismic vs aseismic slip, 6) structural inheritance (Pace et al., 2002; Morewood and Roberts, 2000; Roberts

and Michetti, 2004; Papanikolaou et al., 2005; Han et al., 2007; Soliva et al., 2008; Balsamo et al., 2016; Demurtas et al., 2016). This is proved by the high variability of fractal dimensions among the different fault zones (Table 1 reports data from the literature for faulted carbonates).

Grain size distributions and related fractal dimensions (D) (Sammis & Biegel, 1989; Blenkinsop, 1991) are commonly used to quantify fault-related deformation intensity in fault core rocks and to make inferences on comminution mechanisms, namely bulk fragmentation vs particles grinding and abrasion (Turcotte, 1986; Storti et al., 2003; Storti et al., 2007). In fact, the link between D values and particle fragmentation mechanisms has a straightforward impact on fault friction and seismic behaviour (Keulen et al., 2007; Stunitz et al., 2010; De Paola et al., 2015), and on the physical characterization of pulverized rocks in fault damage zones (e.g. Fondriest et al., 2015).

Early models of cataclasis (Allègre et al., 1982; Turcotte, 1986; Sammis et al., 1987) assumed that fragmentation results in fractal dimensions that provide a measure of the fragility of the fragmented materials (Turcotte, 1986). By using both natural data and mechanical modelling, Sammis et al. (1987) questioned the notion that particle size distributions in fault gouges have log-normal probability functions (Epstein, 1947) and proposed self-similar distributions produced by fragmentation models where the nearest neighbours of the same size are most likely to fracture. This results in particle size distributions evolving towards minimum numbers of equal-sized particles at any scale. In natural phenomena, self-similar processes occur only within a precise range defined by a lower and an upper fractal limit, known as fractal range (e.g. Blenkinsop, 1991). Euclidian geometry imposes that the maximum value of self-similar processes corresponds to 3 (Zhong Yan Zhao et al., 1990; Sammis and King, 2007). However, the evidence that fractal dimensions higher than 3 may occur in natural carbonate fault core rocks (Storti et al., 2003) questions the possibility that self-similar cataclasis comprehensively governs rock comminution in fault core rocks, and favours evolutionary pathways involving the transition through time from dominant particle fracturing to dominant particle chipping and abrasion (e.g. Storti et al., 2003; Billi and Storti, 2004). The importance of D in fault core mechanics requires a deep understanding of the factors that can influence this value, such as fault kinematics and displacement, fault zone architecture, host rock properties, tectonic environment, and analytical methods (Tab. 1). The importance of the latter, despite initially neglected (Zhong Yan Zhao et al., 1990), is now widely recognized as the primary source of variability of D values from cataclastic rocks developed in poorly layered platform carbonates (Storti and Balsamo, 2010a,b). Overall, such variations in fractal dimension may indicate the complexity and heterogeneity of cataclasis in carbonate rocks, which is described as a process

that varies in time and space producing immature to mature cataclasites (Balsamo & Storti, 2011; Ferraro et al., 2018) under aseismic, sub-seismic and co-seismic slip.

To further contribute to reduce uncertainties associated with data acquisition and sample cohesion, we present results from the study of poorly cohesive and loose carbonate cataclastic rocks sampled in the core of the Fiamignano Fault in the Central Apennines (Italy), which were analysed by different methods and analytical procedures, following the approach described in Storti and Balsamo (2010a, b). In particular, for adjacent samples characterised by different cohesion, we compared results obtained by 3D laser granulometry and optical granulometry in loose material, with results from 2D image analysis in poorly cohesive rock. This allowed us to (i) identify advantages and disadvantages of the various analytical techniques, (ii) estimate the influence of fault rock cohesion and, eventually, (iii) contribute to reduce the method-induced variability in the study of fault core rocks developed in poorly layered platform carbonates. The comparison with data from the literature testifies that our fractal dimensions fall in the range of the published data for carbonate fault core rocks (Table 1 and Fig. 9b), particularly for laser wet granulometry. Results of this study provide general guidelines to analyse fault core rocks that can be applied to all lithologies.

STUDIED FAULT	LITHOLOGY (AGE)	KINEMATICS	TECTONIC ENVIRONMENT	SAMPLE DESCRIPTION	REAL FAULT CORE THICKNESS (M)	ESTIMATED MAX. DISPLACEMENT (M)	ANALYTICAL TECHNIQUE	3D D VALUES	P. LOW EXTENT (MM) L. BOUND	REFERENCES
MATTINATA FAULT	Jurassic dolomitic limestone	Reverse, Strike Slip (transpressive)	Foreland	Fault core	26	~2000 (o)	Sieving, Image analysis	2.15-2.77 (G) 2.54-3.48 (A) 2.09-2.93 (B) 2.00-3.04 (C) 1.91-3.38 (D)	0.01 (G) 0.0005 (A) 0.125 (B) 0.1 (C) 0.1 (D)	Billi, 2007 (A), Billi and Storti, 2004 (B) Billi, 2005 (C), Storti et al., 2003 (D), Billi et al., 2003 (G), Billi, 2003 (G)
VIGLIANO FAULT	Mesozoic platform limestone	Reverse	Thrust belt	Fault core	-	100	Sieving, Image analysis	2.85-2.95	< 0.0005	Billi, 2007 (A)
MT. SERRONE FAULT	Cretaceous platform limestone	Extensional	Thrust belt	Fault core	-	1000	Sieving, Image analysis	1.96-2.08	< 0.0005	Billi, 2007 (A)
ASSERGI FAULT	Triassic platform carbonate	Extensional	Thrust belt	Fault core breccia	-	1000 (N)	Image analysis, Sieving, Laser diffraction particle size analysis	2.52-2.87*	-0.01	Storti and Balsamo, 2010 (E), Pizzi et al., 2012 (N)
VENERE FAULT	Mesozoic platform carbonate	Extensional, strike slip	Thrust belt	Fault core	≤1	600	Sieving	2.23-2.95	-0.1	Agosta and Aydin, 2006 (F)
SAGITTARIO FAULT	Jurassic dolomitic limestone	Extensional	Thrust belt	Fault core	-	400	Sieving, Image analysis	2.24-2.60 (G) 2.54-2.58 (A) 1.88-1.95 (D)	0.01 (G) 0.001<>0.002 (A) - (D)	Billi, 2007 (A), Billi et al., 2003 (G), Storti et al., 2003 (D)
PRESENZANO FAULT	Shallow-water layered limestone	Extensional	Thrust belt	-	-	-	Sieving	2.48-2.57 (G) 2.51 (D)	0.01 (D)	Billi et al., 2003 (G), Storti et al., 2003 (D)
GRAN SASSO	Platform limestone	Strike-Slip, Extensional	Thrust Belt	Fault core	-	-	Sieving	2.09-3.49	-	Storti et al., 2003 (D)
MONTI ALBURNI	Platform carbonate	Strike-Slip, Extensional		-	-	-	Sieving	2.26-2.74	-	Storti et al., 2003 (D)
DENT FAULT	Lower Carboniferous limestone	Strike-slip, Reverse	Foreland	Fault core breccia/ coarse cataclasite	-	-	Image analysis	2.68*	0.9	Mort and Woodcock, 2008 (H), Woodcock and Rickards, 2003 (M)
GARGANO FAULTS	Cretaceous slope to basin succession of chert and limestone	Strike-Slip	Foreland	Fault core (limestone)	cm	cm	Image analysis	2.34	0.125	Korneva et al., 2016b (I)
SEMP FAULT (ENNSTAL SEGMENT)	Massive Late Permian to Cretaceous limestone and dolomite	Strike slip	Thrust belt	Fault core, transition zone, damage zone	10	60000	Image analysis	2.92-2.99*	-	Frost et al., 2009 (J)
BORCOLA PASS FAULT ZONE	Sedimentary dolostone and dolomitic marbles	Strike-slip	Thrust belt	Slip zone	cm-m	Not available	Image analysis	<2.3-3.54*	-	Fondriest et al., 2012 (K)
FIAMIGNANO FAULT	Jurassic-Cretaceous carbonates	Extensional	Thrust belt	Fault core	cm-m (P)	500-2000 (L)	LDPSA, IA, MorphologiG3	2.33 -2.86 *	0.68-3000 (P)	Bigi and Costa Pisani, 2005 (L), This study (P)

Table 1: Most relevant geological factors reported for the main fault zones developed in carbonate rocks, with D values calculated for each fault, power low extent (lower boundary) and related data acquisition techniques (values from the literature). In the last raw, values and parameters calculated within this study.

2.2.2 Review of common techniques for grain size characterization

Grain size can be calculated using many different techniques like classical sieving, sedimentation, electrozone sensing microscopy, X-ray attenuation, laser diffraction, and image analysis (Kimura et al., 2018 and references therein). Sieving, laser granulometry and optical granulometry are typically used for loose granular materials while image analysis is one of the most common techniques used to obtain fractal dimension from cohesive rock samples (Heilbronner and Barrett 2014). Classical sieving and sedimentation were the first methods used by sedimentologists to separate particles of different size, often applied by structural geologists. Nowadays, laser granulometry has become a fundamental tool to fast calculate particle size distribution from an elevate number of particles. It works with the principle of laser diffraction for which the instrument measures the diffraction angle of a laser beam that hit particles flowing in a fluid (usually water or air) and then converts this signal in values of equivalent diameter measured assuming perfectly spherical particles. Optical granulometry is another innovative instrument consisting of an optical microscope connected to a computer that automatically measures 3D grain size and shape distribution of particles dispersed over a sample lid. In this case, the results are given as CE diameter (Circle Equivalent diameter), corresponding to the diameter of a circle with the same area as the 2D image of the particle. Even if the shape of particle can influence the CE diameter, this is a single number that gets larger or smaller. Electrozone sensing microscopy and X-ray attenuation are more familiar to chemists and physicists than geologists. The first exploits the capacity of a particle in a conductive fluid to change a constant voltage set between two electrolytes. It is based on the assumption that changes in current are proportional to the volume of the particles analysed. The second, X-ray attenuation (or absorption), is based on the principle that the average transmitted intensity of radiation in a heterogeneous absorber depends, among the others factors, on particle size (Burek, 1976). The intensity of transmitted X-rays increases together with grain size. A widespread technique for measuring 2D particle size is image analysis. A common approach used in image analysis is that of converting the areal values of particles, automatically calculated by a software of image analysis (e.g. the open access ImageJ software), in equivalent particle diameter (Deq) using the Eq. (1).

$$Deq = 2 * \sqrt{\frac{A}{\pi}}. \quad (1)$$

The equivalent diameter is in fact the diameter of a circular particle with the same area of the particle analysed. A similar approach is described by Keulen et al. (2007) that used image analysis

to compare grain size distributions of experimentally produced cataclasites from intact samples of the Verzasca Gneiss and natural granitoids rocks from the Nojima Fault Zone. This method consists of acquiring the values of area and perimeter of particles and convert them in equivalent radii (req) with the Eq. (2).

$$req = \sqrt{(A + P)/\pi}. \quad (2)$$

where P is the area of the pixels composing the particles boundary.

2.3 Study area and sampling strategy

The Fiamignano Fault (Central Apennines, Italy) is a ~ 12 km long, NW-SE trending extensional fault zone cutting through Jurassic to Cretaceous carbonate platform rocks overlain by Miocene carbonate ramp deposits in the footwall and Lower Messinian turbiditic siliciclastic deposits in the hangingwall (Fig. 3a). Estimates of the maximum displacement for the Fiamignano Fault are still affected by significant uncertainty, spanning from 500 to 2000 m (Smeraglia et al., 2016b), or 500 to 1000 m (Bigi and Pisani, 2005). The main fault core of the Fiamignano Fault crops out in an abandoned quarry along the central sector of the fault zone (Fig. 3a) and consists of a ~ 3 - 5 m-thick cataclastic rocks, mainly composed of dolostone fragments, juxtaposed to an extremely polished surface (Fig. 3b). A pair of adjacent representative samples (FI1a and FI1b, respectively) were collected at the same site (Fig. 3b) after having removed ~ 10 cm of loose material to avoid biases due to surface weathering. The fact that the two samples were collected at ~ 10 cm of distance from each other ensures that the two materials likely underwent the same deformation mechanism and intensity, and reasonably developed the same grain size distribution. This assumption, together with the lack of cement in the cohesive sample, gives the possibility to compare the loose sample with the cohesive one by assuming to have exactly the same starting faulted material. The different cohesion of the two samples was enhanced by the sampling strategy: sample FI1a was removed from the fault plane, manually disaggregated and put in a small plastic bag without taking care to preserve its cohesion. On the contrary, sample FI1b was carefully removed from the fault plane using sharp tools, packed and subsequently impregnated. The variability in sample cohesion provided the possibility to test the influence of 2D (image analysis) and 3D (wet and dry laser granulometry, optical granulometry) analytical techniques and to compare the related fractal dimensions in the best natural conditions.

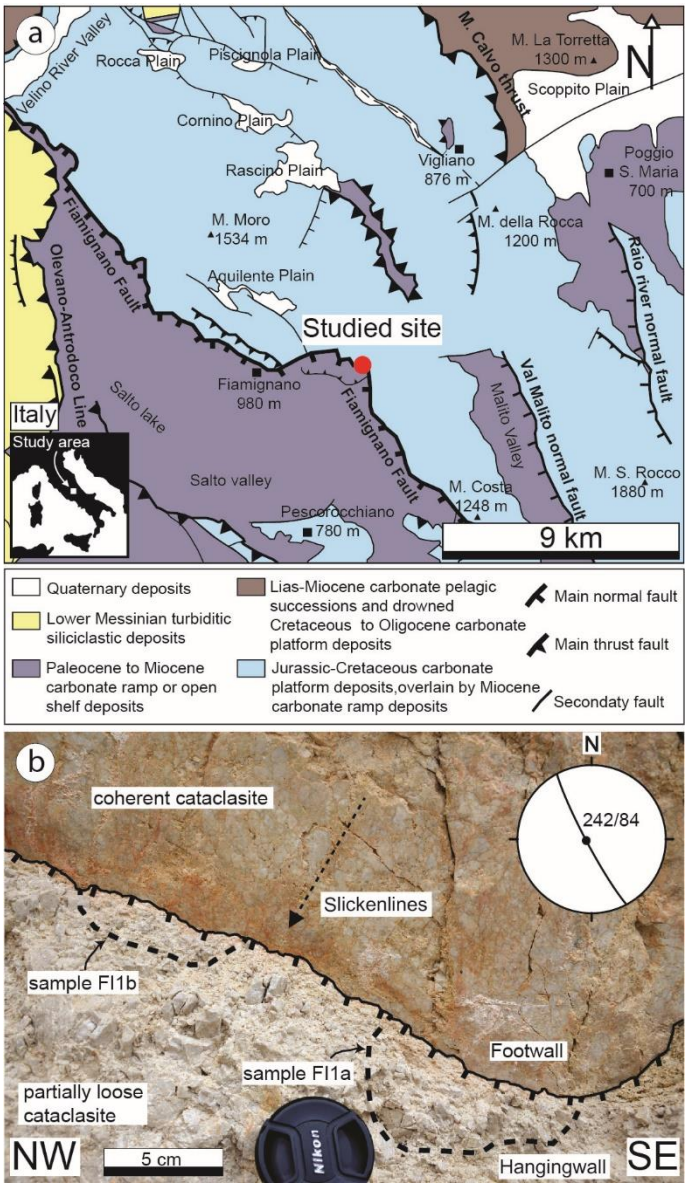

Figure 3: Structural map of the Fiamignano area (modified after Bigi and Costa Pisani, 2005) with the location of the collected samples and the main structural lineaments. (b) Main fault with sampled cataclasite associated to the polished fault surface in the same fault block. Average fault attitude (dip direction, dip angle) is plotted in the stereonet on the right; the black point in the plot represents the average orientation of the slickenlines measured on the main slip surface.

2.4 Methods

2.4.1 Sample preparation

Sample FI1a consists of ~500 g of loose cataclastic material with mm-size clasts. It was dried at 40°C for 24 hours, sieved at 2 mm, and then divided in small portions, using first a Quantachrome sieving riffler and then a Quantachrome rotary micro-riffler, thus obtaining representative sub-samples suitable for analyses with laser and optical granulometry. We prepared several aliquots from the same starting material because samples can not be recovered after the analyses. For our

purpose, we used (1) a laser diffraction particle size analyser (Malvern Mastersizer 3000) and associated dry and wet dispersion units (Aero S and Hydro EV, respectively), and (2) an optical particle size analyser (Malvern Morphologi 4-ID).

Sample FI1b consists of a poorly cohesive cataclasite that was carefully impregnated with epoxy resin and sectioned perpendicular to the fault plane and parallel to slickenlines to obtain a 40 μm thick petrographic thin section suitable for optical and scanning electron microscopy. The thin section was coated with carbon before SEM analysis.

2.4.2 Instruments and analytical procedures

2.4.2.1 Laser granulometry

The Malvern Mastersizer 3000 works on suspensions, emulsions and dry powders on the size range between ~0.01 and ~3500 μm. In our case, light scattering data collected by the instrument using a blue and red light dual-wavelength, single-lens detection system, were automatically inverted by the Mie theory (Boer et al., 1987), which is suitable for non-spherical particles, and grouped in 100 size classes automatically generated by the instrument. The refractive index was set at 1.572, which corresponds to the value of calcite, while the other parameters were chosen separately first for dry analyses and then for wet analyses.

Before starting with the dry analyses, we performed preliminary tests with different settings of measurement time (Fig. S1 in the Supplementary material) air pressure and feed rate in the dispersion unit (Fig. S2 in the Supplementary material), to define the most appropriate (i.e. less invasive) Standard Operative Procedure (SOP) for the analysis of our sample. Each test was performed on an identical sub-aliquot (~3.5 g) of the original sample FI1a, previously obtained by splitting. Once having defined the proper SOP, we performed the analysis fixing air pressure at 1 bar and feed rate at 60%. This analysis was performed on another sub-aliquot (~3.5 g) obtained from the same sample FI1a. To add the right amount of sample in the dispersant and control the quantity of material recirculating into the system during the analysis, we monitored the obscuration value, which is a parameter that measures the amount of laser light lost due to the introduction of the sample into the analyser beam.

For wet analyses we followed a similar procedure and performed some preliminary tests to verify the influence of pump speed velocity, measurement time, and ultrasonication intensity (Figs. S3-S7 in the Supplementary material) on the sample during analysis. Even in this case, each analysis was performed on identical sub-aliquots (1-2 g) obtained from splitting the sample FI1a with macro and micro rotary riffler. Each test consisted of 25 runs performed under fixed conditions for two

variables and systematically varying the third one (Storti and Balsamo, 2010b) (Figs S3-S7 in the Supplementary material). After having defined the best SOP, we analysed another sub-aliquot of the same material setting pump speed at 1700 rpm, measurement time at 20 s and no ultrasonication energy. Even in this case, we monitored the obscuration value.

With both dry and wet laser granulometry, we acquired a value of equivalent diameter for each particle, which corresponds to the diameter of a particle assumed to be perfectly spherical, and the value of volume % (V%) for each size class (100 classes in total) created automatically by the instrument. The values of equivalent diameter were converted first in the correspondent volume of each particle (Vp) using the Eq. (3)

$$Vp = \frac{4*\pi*req^3}{3}. \quad (3)$$

and then in cumulative number of particles for each class (Np) using the Eq. (4).

$$Np = \frac{V\%}{Vp*100}. \quad (4)$$

The calculated number of particles for each class (Np) was plotted versus size classes in a log-log diagram to obtain a curve with a slope corresponding to the value of fractal dimension (D3). Following the procedure described by Keulen et al. (2007), not perfectly linear data distributions were also best fitted by two power laws.

2.4.2.2 Optical granulometry

The Morphologi 4-ID is an optical microscope connected with a dispersion unit and a camera that acquires grey-scale pictures that are automatically processed to obtain particles size and shape data in the 0.5-1300 µm size range (the range can be extended for some applications). Unfortunately, the automatic dispersion unit works with a very small volume of sample to avoid the formation of particles aggregates. The Morphologi 4-ID can illuminate sample, with a white light LED, from below or above, controlling light levels. The optical system (Nikon CFI 60 bright-field/ dark-field system) allows to choose the more appropriate magnification (from 2.5x to 50x) to capture clear images and merge them together to create a representative 3D grain size distribution of the sample analysed. The instrument also allows to capture images of the same sample dispersion with more than one magnification (e.g. 2.5x and 10x). Data extrapolated from such images are automatically merged together by the instrument in a single output file. The Morphologi 4_ID works with both: 1) the automated 'Sharp Edge' segmentation or 2) the manually-controlled thresholding.

Before the analysis, we performed a calibration test (Fig. S9 in the Supplementary material) to choose the most appropriate magnifications. Then, we tested the measurement reproducibility (Fig. S10 in the Supplementary material) by repeating the same analysis for three times on identical size areas of the same sample dispersion. We used 15 mm^3 of the starting loose sample FI1a that were dispersed automatically over the sample lid using the automatic dispersion chamber (Fig. S8 in the Supplementary material). During the analyses, we adoperated two different magnifications (2.5x and 10x) to guarantee particle detection over a wide size range (~0.675 µm – ~666 µm). The instrument automatically provides the CE diameter of particles (i.e. the diameter of a circular particle with the same area of the particle analysed). Data of CE diameters were used to build the frequency distribution by dividing the acquired data in the same 100 size classes previously adopted for laser granulometry. This allowed us to make a direct comparison between results from the different techniques. For the calculation of fractal dimension, we plotted in a log-log diagram the cumulative number of particles obtained from the frequency distribution versus grain size. Following this procedure, we obtained a distribution fitted by a power law in a linear fractal range, and then the corresponding value of fractal dimension. Even in this case, not perfectly linear data distributions were also best fitted by two power laws.

2.4.2.3 Multiscale Image analysis

Image analysis on sample FI1b was performed using images acquired at different magnifications. We started with optical scanning of the whole thin section by a Nikon Super Coolscan 5000, and then moved to the Zeiss Axioplan 2 optical microscope. We finally adoperated the JEOL JSM 6400 scanning electron microscope (operating settings 240µA and 20kV) to acquire micrographs at higher magnification of representative sub-areas. In particular, we processed a scan image with area of 460 mm^2, two images from the optical microscope of respectively 4.15 mm^2 acquired at magnification 25x (2.5x plus the ocular magnification 10x) and 1.15 mm^2 acquired at 50x (5x plus the ocular magnification 10x), and one image from the SEM with area of 0.069 mm^2 acquired at 1050x (Fig. 7). We manually traced grains boundaries (we classify a micro-fractured particle formed by a number of sub-grains still preserving their cohesion as one single particle) and automatically converted the original photographs in black and white bitmap images using the software ImageJ (Fig. 7) (using the option “exclude on edges” to delete clasts truncated at the edges of the images). From the software, we obtained the areal values of particles that we converted in equivalent diameters using the equation (1). We analysed 983 particles on the thin section, 286 particles at 25x, 212 particles at 50x and 902 particles at 1050x. Then, basing on the 100 size classes used also in the other techniques,

we calculated the number of particles for each size class (frequency distribution). This allowed us to plot in a log-log diagram, the equivalent number of particles versus size classes and thus extrapolating the value of fractal dimension (D2) which represents, in this case, a 2D grain size distribution. The curves obtained for each magnification were multiplied for their corresponding scale factors (see Figure S10 in the Supplementary material). This operation allowed us to make data acquired at different magnifications comparable, and thus create a complete grain size distribution over three orders of magnitude in the 2.13–2390 µm size range. Linear data distributions were best fitted by one power law, while non perfectly linear data distributions were best fitted by two power laws.

2.5 Results

2.5.1 Laser granulometry with dry module

Reproducibility test in dry laser granulometry, consisting of comparing the results of five different analyses with the same parameters, shows very similar values of fractal dimension ranging from 2.27 to 2.35, that proved the effectiveness of the selected operating procedure (Figure S2c in the Supplementary material). We chose one of these tests (i.e. the reproducibility test 4 which has the lowest number of fractal dimension) to present and discuss the results obtained with this methodology (Fig. 4). The frequency distribution obtained by plotting volume percentage versus log. particle size (Fig. 4a) shows a unimodal and asymmetric grain size distribution with modal peak at ~1630 µm. The corresponding cumulative number of equivalent spherical particles plotted versus the corresponding grain size classes, in the log-log diagram (Fig. 4b), has a roughly linear distribution within the 1.45 - 2100 µm size range. The resulting fractal dimension calculated over this size range is D3 = 2.27, with a correlation coefficient of R2=0.99 (Fig. 4b). Since the data distribution in Figure 2b displays a light curved trend, we tried to fit the data with different power laws, thus obtaining two corresponding values of fractal dimension in two quasi-rectilinear segments of the cumulative distribution. We calculated a value of D3 = 2.93 (R2=0.99) in the lower size range (1.45-14.5 µm), corresponding to a curve segment with a high slope, and a lower value of D3 = 2.02 (R2=0.99) in the upper size range (14.5-2100 µm), corresponding to a curve segment with a lower slope. Overall, the value of fractal dimension obtained by averaging the entire curve is lower than the value obtained for the lower size classes and higher than that obtained for the higher size classes (Fig. 4b).

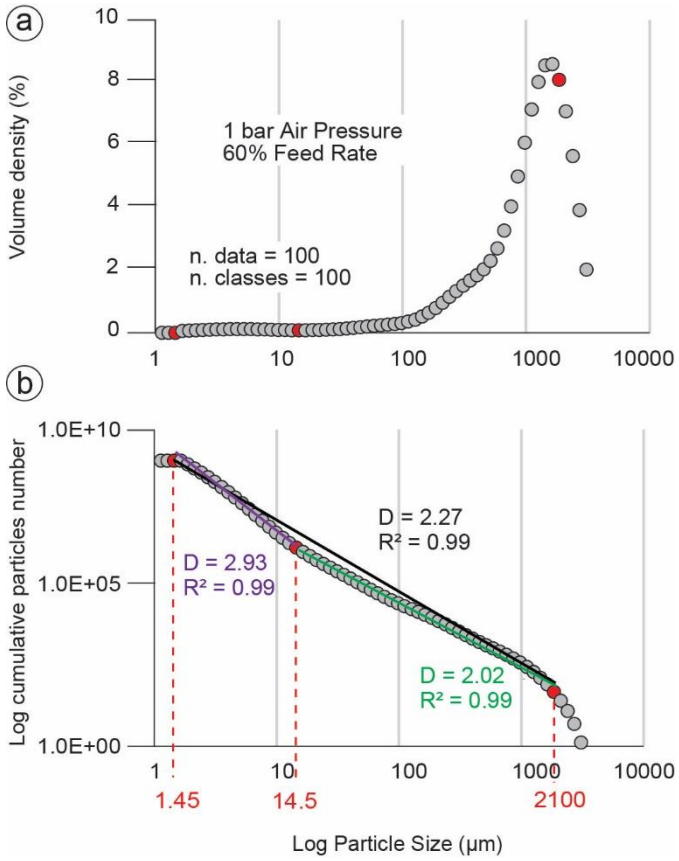

Figure 4: (a) Granulometric distribution of data obtained with dry laser granulometry at 1 bar of Air Pressure and 60% of Feed Rate. (b) Cumulative of equivalent particle number plotted versus particle size in a bi-logarithmic graph with related fractal dimension calculated over the 1.45-2100 µm size range. The values of fractal dimension, and related correlation coefficients, calculated over the 1.45-14.5 µm size range and the 14.5-2100 µm size range are also provided.

2.5.2 Laser granulometry with wet module

For wet laser granulometry, after having proved the measurement reproducibility (Fig. S6 of the Supplementary material), we could select, from one of the five tests, the first run with 0% ultrasonication energy because it is the less biased analysis that preserved coarsest particles and thus the best natural conditions (Fig. S7b in the Supplementary material). The frequency distribution obtained with this analysis, consisting of plotting volume percentage versus log. particle size is represented by a slightly polymodal distribution over the 0,46-1430 µm size range. Despite the irregularity of the curve, it is possible to recognize a predominant peak at ~200 µm and a lower peak at ~25 µm (Fig. 5a). In the log-log diagram obtained by plotting the cumulative number of particles versus particle size (Fig. 5b), the value of fractal dimension calculated over the 0.46-1430 µm size range is D3=2.76 (R2=0.99). Even in this case, due to the variable trend of the cumulative distribution, we tried to fit the curve by using two different power laws over the 0.46-21.2 µm and

the 21.2-1430 µm size ranges respectively. The value of fractal dimension obtained for the fine classes (D3=2.7 with R2=0.99) is slightly lower than that obtained for the coarse ones (D3=3.0 with R2=0.99) and that averaged over the whole size range of the cumulative distribution.

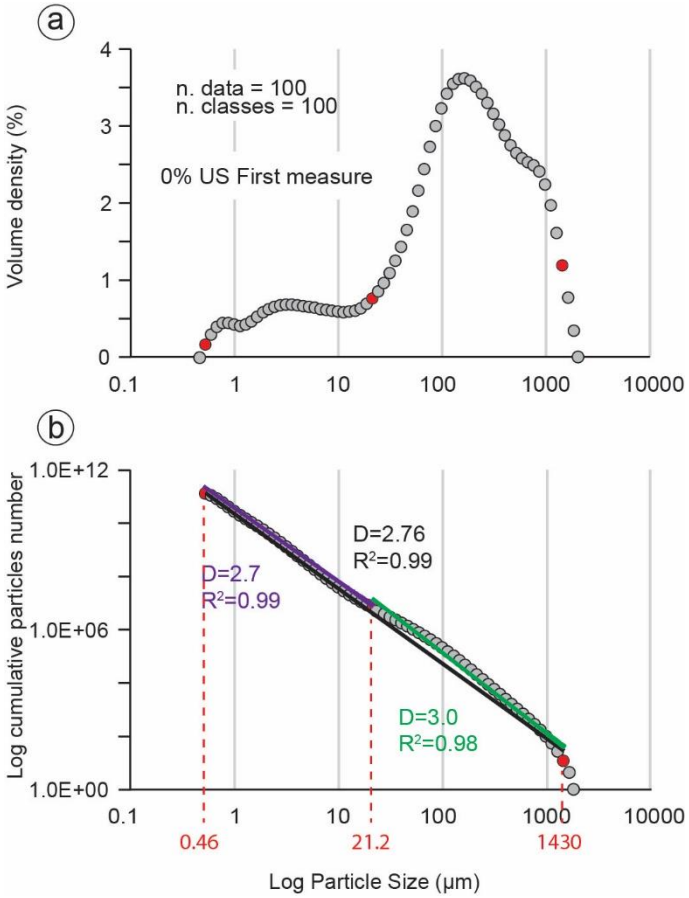

Figure 5: a) Granulometric distribution of data obtained with wet laser granulometry with 0% ultrasonication energy. (b) Cumulative of equivalent particle number plotted versus particle size in a bi-logarithmic graph with related fractal dimension calculated over the 0.46-1430 µm size range. The values of fractal dimension, and related correlation coefficients, calculated over the 0.46-21.2 µm size range and the 21.2-1430 µm size range are also provided.

2.5.3 Optical granulometry

Results from optical granulometry of sample FI1a are provided in Fig. 6, while details on reproducibility test can be found in the Supplementary material (Fig. S10). Unfortunately, data of particle with equivalent diameter ≥ 586 µm are missing because we manually removed them before entering the material into the instrument, which is not able to work with such big particles. For this reason, a comparison between this curve and the results from laser granulometry and image analysis has some limitations. The curve corresponds to a unimodal and peaked curve with modal value at about 3 µm (Fig. 6a). In Figure 4b, the cumulative number of particles plotted versus particle

size in a log-log diagram is fitted by a power law over the 3.55-586 µm size range and gives a value of fractal dimension of D3=2.28 (R2=0.99). We further tried to fit the curve with two different power laws on two rectilinear segments. The resulting fractal dimensions vary from D3=2.26 (R2=0.99) for the fine size classes (3.55-35.3 µm size range), to D3=2.63 (R2=0.98) for the coarse size classes (35.3-586 µm size range).

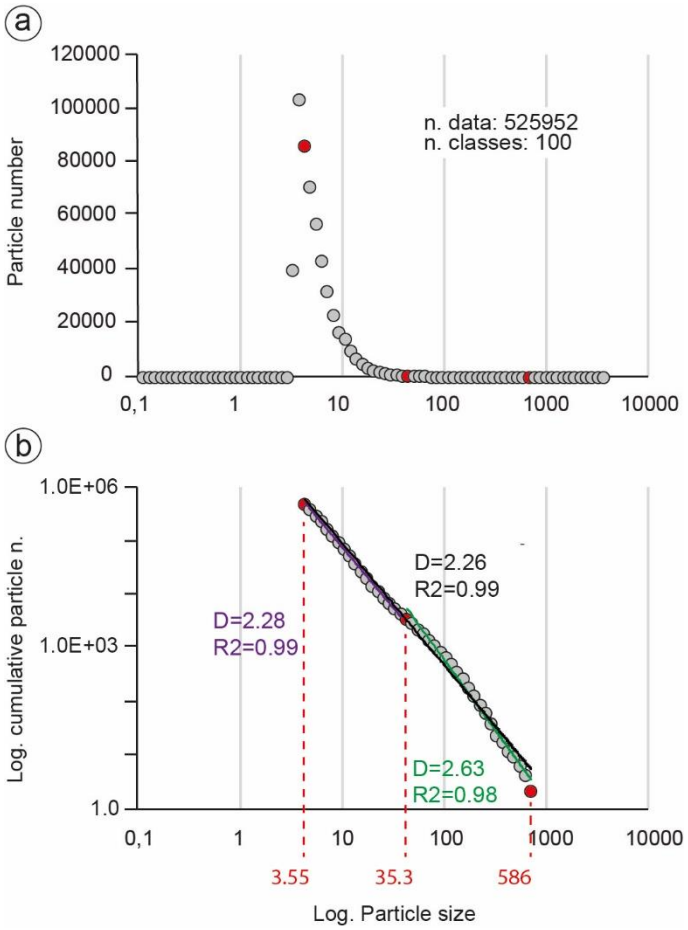

Figure 6: a) Granulometric distribution of data obtained with optical granulometry. (b) Cumulative of equivalent particle number plotted versus particle size in a bi-logarithmic graph with related fractal dimension calculated over the 3.55-586 µm size range. The values of fractal dimension, and related correlation coefficients, calculated over the 3.55-35.3 µm size range and the 35.3-586 µm size range are also provided.

2.5.4 Microstructures and multiscale image analysis

The microstructures of the sampled cataclastic material were studied on the thin section obtained from sample FI1b (Fig. 7). The fault rock appears as a non-foliated, coarse-grained cataclasite made by heterogeneous clasts, mostly dolomite in composition, characterized by different size and, on average, sub-angular shape (Fig. 7). Significant grain size reduction (from 5 mm to few µm in size) occurs from the inner part of the thin section to the proximity of the slip

surface (Fig. 7a, e). Next to the slip surface, grain size decreases down to few micrometers, except for some µm- to mm- size survivor grains localized along the master slip surface (Fig. 7e). The roundness of clasts does not seem to depend on their mineralogical composition, even because many clasts are constituted by a mosaic of small fragments of different origin and mineralogical composition. Some coarse clasts present thin calcite veins thus testifying that these clasts come from a cohesive rock affected by fluids circulation. SEM images show that a very fine-grained matrix occurs, whereas no cement was found between clasts (Fig. 7d). Matrix is partially made by comminuted clasts of dolomite and calcite with brownish colour under optical microscope. Some dolomite clasts contain microfractures that are not extended up to the clast borders and thus not affecting the integrity of clasts.

Results from multiscale image analysis are derived from four different analyses performed, on the thin section in Figure 5a, at different magnifications: scan image, 25x, 50x and 1050x. The results are presented as cumulative particle number versus particle size in log-log diagrams with different colours corresponding to results obtained at different magnifications (Fig. 8). Plotting data from different images with different colours facilitates realizing that all distributions have concave-upward shapes, characterized by inclined sectors in the coarser sizes, followed by overlapping flat-lying sectors in the remaining size classes, outside the lower fractal limits (Fig. 8a, b). Preserving only data in the intervals that provide linear best fits with $R2 \geq 0.9$, i.e. within fractal range limits, provide an overall curve with well-aligned data points (Fig. 8b). We obtained four different values of fractal dimension acquired with the four different magnifications: D2=1.87 at 1050x with the SEM, D2=1.75 at 50x with the optical microscope, D2=2.30 at 25x with the optical microscope and D2=2.66 with the scan image. By merging the results from the different magnifications, we obtained a cumulative fractal distribution over three orders of magnitudes in the 2.13-2390 µm size range (Fig. 8c). The fractal dimension obtained on this wider interval is D2=1.98 (R2=0.99). Since the curve displays a slightly curved trend, we also tried to fit data with two power laws. This results in two different values of fractal dimensions calculated respectively in the 2.13-98.1 µm (small particles) size range and 98.1-2390 µm size range (coarse particles) (Fig. 8c). The value referred to the first interval is D2=1.76 (R2=0.99), whereas the value referred to the second interval is D2=2.46 (R2=0.98). In this case, the fractal dimension calculated for the small size classes is lower than that calculated for coarse size classes. The fractal dimension averaged on the whole size range analysed is intermediate with respect to the other two values. Moreover, the Sammis' correction to pass from 2D to 3D fractal values provided fractal dimension calculated in the coarse classes D3=3.46.

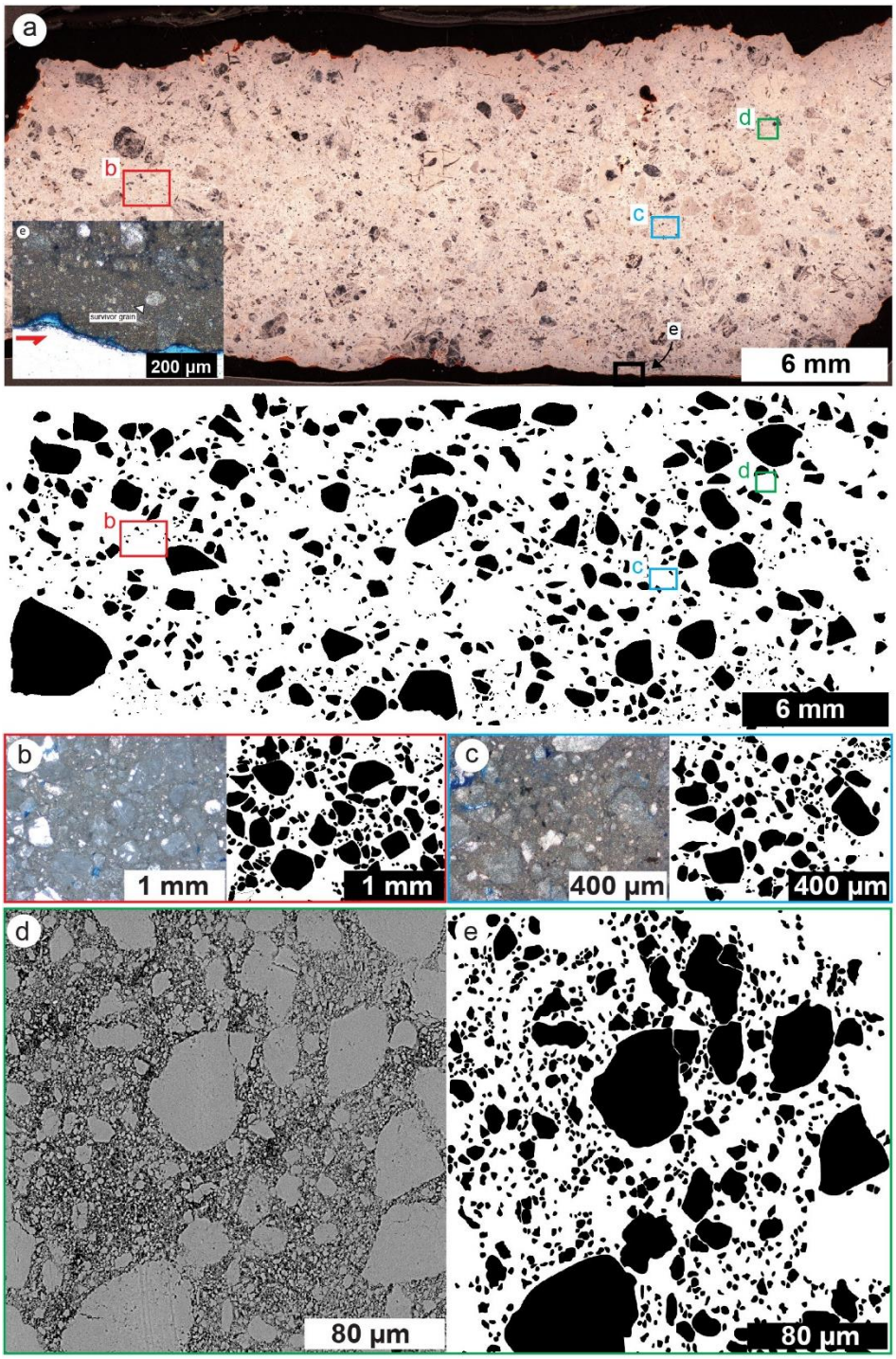

Figure 7: Multiscale image analysis at the optical microscope and scanning electron microscope. (a) Scanned thin section of 3282 x 1311 px – 0.089 px/µm with inverted colours and corresponding segmented image. The images contain the indication of the sub-areas analysed at higher magnifications (b, c, d). (b) Image of 2592 x 1944 px – 1.1 px/µm acquired with optical microscope at 2.5x with the corresponding segmented image (on the right), (c) image of 2592 x 1944 px – 2.09 px/µm acquired with optical microscope at 5x with the corresponding segmented image (on the right), (d) image of 1024 x 1025 px – 41 px/µm acquired with scanning electron microscope at 1050x with the corresponding segmented image (on the right), (e) grain size reduction toward the master slip surface at the optical microscope. The slip surface is indicated with the red arrow while big survivor clasts embedded into the brown matrix are indicated with the white arrow.

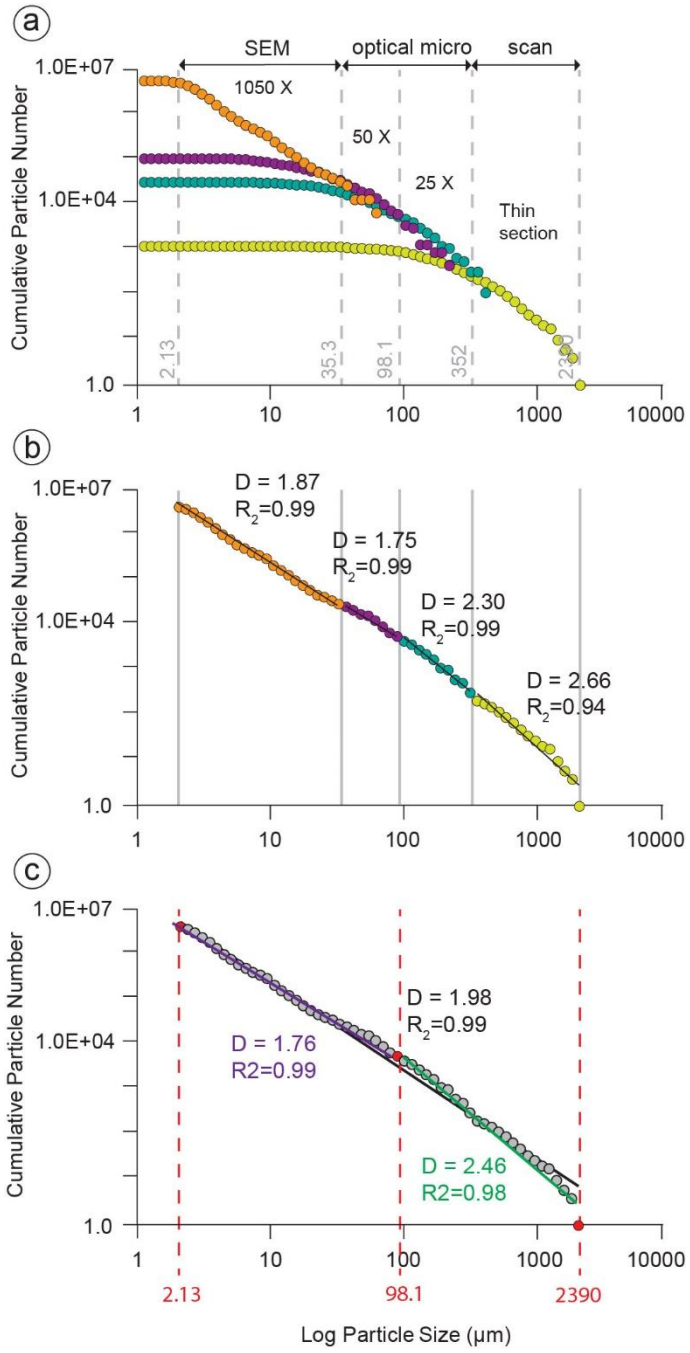

Figure 8: Results of multiscale image analysis on thin sections at magnifications of 25x, 50x (values obtained multiplying the magnification of the objective – 2.5x and 5x- and the magnification of the ocular – 10x) at the optical microscope and 1050x at the scanning electron microscope. Values are represented as cumulative equivalent particle number plotted versus size in bi-logarithmic graphs. (a) Total data acquired at different magnifications plotted separately for different granulometric curves. (b) Data acquired at each magnification truncated to create a single granulometric distribution within the 2-976 µm size range. (c) Resulting granulometric distribution with the calculated fractal dimension of 1.97, and related correlation coefficient, over the 2.13-2390 µm size range and fractal dimensions calculated over the 2.13-98.1 µm and 98.1-2390 µm size ranges, and related correlation coefficients.

2.6 Discussion

2.6.1 Comparison of fractal dimensions obtained with different methods

With wet and dry laser granulometry, we analysed two aliquots of the same loose material (sample FI1a) that show significant differences in terms of fractal dimension (Fig. 9a). We obtained an average value of D3=2.27 with the dry procedure and a value of D3=2.76 with the wet procedure after the first run of the 0% ultrasonication test. The increase in fractal dimension from the first to the last run (D3=2.87) in wet laser granulometry, which is indicated in Fig. 9a with a vertical arrow, is due to the disaggregation process occurring during wet laser granulometry, that was already addressed by Storti and Balsamo (2010a, b). For both wet and dry procedures, we performed five identical analyses to verify measurement reproducibility (Figs. S2 and S6 in the Supplementary material). The mean fractal values obtained for both dry and wet reproducibility analyses are plotted and compared with literature data in Fig. 9b, where the calculated standard deviations show much more variability in wet tests than in dry tests. This variability in wet tests is caused by the heterogeneous disaggregation during sample analyses in water. In 0% ultrasonication tests (Fig. S7 in the Supplementary material), the initial disaggregation of particles is also followed by particle fragmentation thus resulting in higher values of fractal dimension due to the increase of fine particles with respect to the original sample. The value of fractal dimension changes from D=2.76 to D=3.04 from the first to the last run (Fig.S7 in the Supplementary material). This is even more evident in 10% ultrasonication test, in which the value of fractal dimension, averaged on all the runs, is D=3.54 (Figure S7 in the Supplementary material), likely due to the reopening of intraclast microfractures; for this reason, the results obtained from the 10% ultrasonication tests are considered strongly biased and not further discussed and displayed in Fig. 9b (cf. Storti and Balsamo, 2010a and references therein).

On the contrary, the constant D values obtained from the five dry analyses (D3 between 2.27 and 2.35, Fig. 9b) suggest that dry procedure is perfectly stable and reproducible. Despite this, we noticed that that the curve of dry laser granulometry has an anomalous shape for particles size > 10 µm. This is likely due to a limit of the dry procedure in disaggregating very coarse particle aggregates (>100 µm), resulting in an increase of particles coarser than 100 µm and consequent lack of smaller particles in the 10-100 µm size range (Figs. 2 and 8). This is evident in Fig. 10, where we compare, among the others, the curve of dry laser granulometry with that from wet laser granulometry. Despite this limit in dry laser granulometry, laser granulometry in general allows to analyse a very high number of particles with respect to the other techniques (i.e. optical granulometry and image

analysis). For this reason, in Fig. 10, the curves obtained from laser granulometry contain larger number of particles than that from optical granulometry and image analysis. Moreover, in Fig. 10 the distribution built for image analysis has a lower slope with respect to the others because it represents 2D values of particle diameters instead of 3D distribution as the others (Fig. 10).

Remarkably, the value of fractal dimension from dry laser granulometry almost coincides with that from optical granulometry: D3=2.27 versus D3=2.28, respectively (Fig. 9a). This similarity is quite surprising since the two curves were calculated over different fractal ranges: 1.45-2100 μm in dry laser granulometry and 3.55-586 μm in optical granulometry. Therefore, these two procedures are the less invasive for fractal dimension determination. The narrowness of the fractal range investigated with the optical granulometry varies among the different areas of the same sample dispersion (Figure S10 in the Supplementary material) and reflects the small volume of sample introduced in the dispersion chamber. In fact, the automatic dispersion unit works with a very small volume of sample to avoid the formation, on the sample holder, of particles aggregates made by single small particles difficult to recognize.

With the multiscale image analysis, we calculated an average 3D value of D3=2.98 (Fig. 9a), obtained by converting D2= 1.98 with the Sammis' convention (Sammis et al., 1987). Multiscale image analysis is a valuable method to calculate GSD in cohesive sample and offers a strong control on the material analysed. In particular, it gives the possibility to classify a micro-fractured particle formed by a number of sub-grains still preserving their cohesion as one single particle (which is the method that we adopted in our analyses) thus helping to overcome the problem of the ephemeral cataclastic fabric of carbonate fault core rocks (cf. Storti and Balsamo, 2010b.) On the other hand, image analysis, especially when the digitalization of the clasts is made manually, can analyse a limited number of particles due to time-consuming procedure. The real number of particles analysed is in fact smaller than laser and optical granulometry, and final number of particles obtained by multiscale image analysis are affected by the multiplication, in each sub-image, for the areal scale factors (Fig. S11 in the Supplementary material). Moreover, results from image analysis may be approximated due to the truncation of the clasts during the preparation of the thin section. The 2D images acquired with the scan, the optical and the scanning electron microscopes represent 2D images of truncated particles with diameters different from the effective ones. The use of the Sammis' law reduces this bias by assuming a uniform mixing of particles on the plane and helps to obtain a 3D value of fractal dimension from 2D images of particles (Sammis et al., 1987). Therefore, we believe that the comparison between 3D fractal values calculated from the volume of an

equivalent spherical particle (i.e. wet and dry laser granulometry) with 3D fractal values obtained from the area of an equivalent circular particle, (i.e. multiscale image analysis), corrected by the Sammis' law, is not always straightforward. This is demonstrated by the high D values obtained from image analysis in this study, which probably is biased by the lack of truncated coarser clasts that could have reduced the slope of the best fit line. For this reason, we suggest caution in comparing results from 3D and 2D analytical techniques.

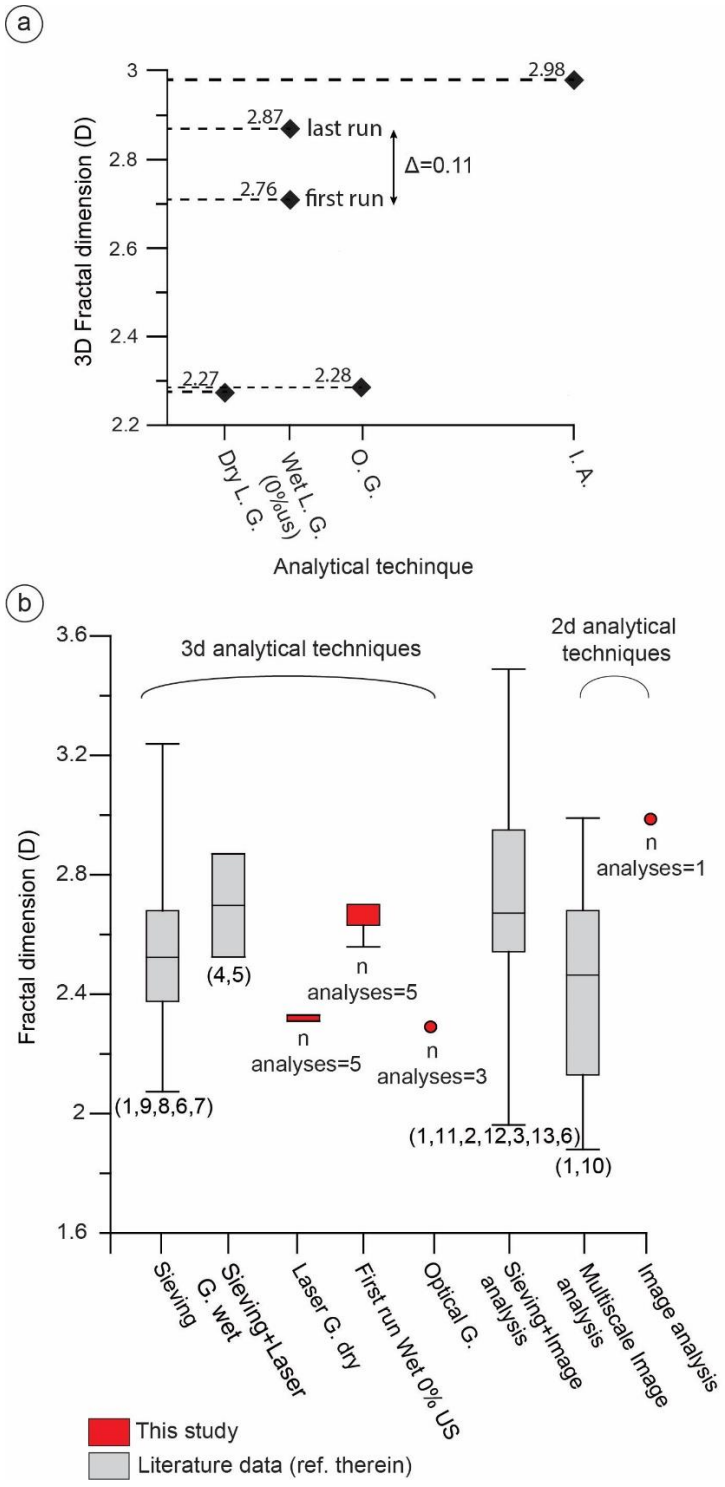

Figure 9: (a) Comparison among the values of fractal dimension calculated during this study (b) comparison between our data and data from the literature for carbonate fault core rocks. In (a): Dry Laser Granulometry (Dry L.G.), Wet Laser Granulometry with 0% ultrasounds (Wet L.G. 0%us), Image analysis (I.A.) and Optical Granulometry (O.G.). (b) Box-plot representative of data from this study (red boxes and points) and from the literature (grey boxes). The numbers indicated below the box-plots refer to the following case studies from the literature: (1) Mattinata (Italy), (2) Vigliano (Italy), (3) Mt. Serrone (Italy), (4) Assergi (Italy), (5) Venere (Italy), (6) Sagittario (Italy), (7) Presenzano (Italy), (8) Gran Sasso (Italy), (9) Monti Alburni (Italy), (10) Dent Fault (UK), (11) Gargano (Italy), (12) Salzach–Ennstal–Mariazell–Puchberg [SEMP] (Austria), (13) Borcola Pass (Italy).

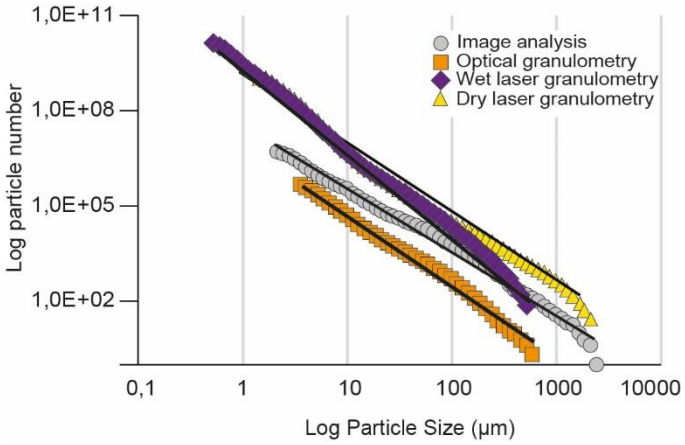

Figure 10: Cumulative frequency distribution obtained from the four different analytical techniques. Curves from laser granulometry are higher with respect to the others due to the more elevate number of particles analysed with this technique. The curve of image analysis represents 2d values of particles diameters and thus has a minor slope with respect to that of laser and optical granulometry.

2.6.2 Significance of double slope in GSD cumulative diagrams among different methodologies

By the observations of the granulometric distributions obtained with the different techniques, we found that more than one value of fractal dimension can be extrapolated from the same curve. In particular, we tried to calculate two D-values for each analytical technique by considering different slopes on the same cumulative distribution: a D-value (D<) for small grain sizes and a D-value (D>) for large grain sizes. In fact, in the curves analyzed we could recognize a break that separates segments of variable slope that can be fitted by two different power laws. We called "d" (in agreement with Fondriest et al., 2012) the value of grain size corresponding to this break. We found that d varies in an interval ranging from 11.20 µm to 35.3 µm among the data obtained with the four analytical techniques. In our case, d cannot be considered the grinding limit, defined as the threshold grain size value below which clasts or particles cease to develop fractures and deform by abrasion during rolling (Keulen et al., 2007), because it usually corresponds, in calcite, at values of particle diameters ~4 µm (An and Sammis, 1994). The lower limits of our fractal distributions do not allow to identify and discuss the grinding limit, since not all the curves extend below this threshold value (i.e. distributions from optical granulometry and image analysis). However, in agreement with Keulen et al., 2007, we found that D< is smaller than D> in three of the four adoperated techniques. In image analysis, this is also in agreement with the values of fractal dimension calculated for grain sizes < 100 µm (50x and 1050x), which are significantly lower than that obtained for grain sizes > 100 µm (25x and scan image). In particular, in image analysis we found that D< corresponds to 1.76

while D> corresponds to 2.48 (Fig. 8c). The corresponding 3D values are very high, especially that of D>, which is considered supra-fractal since it exceeds the value of 3. Results from the dry laser granulometry indicate an opposite situation, where the value of D> is smaller than that of D< (Fig. 4b). This opposite trend is explainable by the underestimation of particles in the interval 10-100 µm that significantly changes the normal slope of the curve (Figs. 2, 8). If analytical procedure would not have strongly affected the measured particles, the obtained value of d would have been the same among all the four analyses. Thus, we conclude that the value of "d", in our case, further indicates the mechanical influence of the analytical technique on the sample analyzed.

2.6.3 Role of sample cohesion

The variability in fractal dimension obtained in this study is firstly explained by the adoperated analytical procedure. Nevertheless, since we analysed three poorly coherent samples and one cohesive cataclasite, we must also discuss the possible influence of sample cohesion on the obtained results. In nature, when cohesion is not produced by post-kinematic cement, it can be produced by abundant fine particles (silt- and clay-size components). Such potential different grain size distribution can provide an additional source of uncertainty in the interpretation and comparison of fractal dimensions obtained from loose and coherent samples. In our case, cement is lacking within the cataclasite (Fig. 7) thus we investigated the present of fine particles in sample FI1.b to give a possible explanation to the different rock cohesion between FI1a and FI1b. The high value of fractal dimension obtained from image analysis demonstrates that the sample has, on average, more small particles than coarse particles. However, with image analysis we analysed particles coarser than 2.13 µm (Fig. 8). On the contrary, volumetric analyses performed on the loose samples detected particles < 2 µm, thus indicating that the poorly cohesive material contains particles smaller than the cohesive sample or, at least, as small as that of the cohesive sample. Unfortunately, the lower resolution limit of image analysis (about 2 µm) depends on the resolution of the image acquired with the SEM and does not allow to verify the presence of very small particles comparable with that observed with optical and laser granulometry. For now, we use our data that support the evidence that the poorly cohesive samples and the loose sample are exactly the same material because they experienced the same deformation in the same place at the same time. Consequently, we suggest that the bias induced by different cohesion, if present in our analyses, is negligible and we attribute the high value of fractal dimension obtained for the cohesive sample with image analysis to the methodology and not to real differences in GSD between the samples FI1a and FI1b.

2.7 Conclusions

In this work, we analysed the influence of different analytical techniques on the calculation of fractal dimension. The different analytical procedures have advantages and disadvantages depending on method of data acquisition and sample type. Results can be summarized as follow:

(1) in agreement with previous works (Storti and Balsamo, 2010a, b) wet granulometric analyses on loose cataclastic samples, even at low ultrasound energy, can cause the partial fragmentation of particles with consequent overestimation of fractal dimension. This happens when a precise standard operative procedure is not scrupulously defined and adopted. During wet analyses, disaggregation of coarse particles can also occur when weak carbonate fault core rocks are analysed. With this procedure, particles aggregates or particles constituted by n sub-grains can be destroyed.

(2) Dry analyses with the new standard operative procedure developed for the Mastersizer 3000 granulometer avoid particles fragmentation in the sample but presents some limitations in breaking particles aggregates and recognizing sub-grains in micro-fractured particles. In our samples, the system had some problems to count particles over the 10-100 μm size range. Meanwhile, it over-estimated particles (or aggregates of particles) coarser than 100 μm in diameter.

(3) The optical granulometry Morphologi 4-ID is a good innovative methodology that works with a very small amount of loose material, thus operating a selection in the original sample. It also presents some important limitations dealing with the sample dispersion system and the analysis of coarse particles. It is not always able to detect the existence of particles aggregates characterizing the samples of weak carbonate fault core rocks. Moreover, the automatic sample dispersion unit sometimes creates new aggregates during the dispersion of the fine particles over the sample lid, especially when too much material is introduced all together in the dispersion unit. Overall, the Morphologi 4-ID works well on very homogeneous loose materials but has significant limitations to analyse heterogeneous samples, even with multiple magnifications.

(4) Multiscale image analysis is time consuming but allows to analyse poorly cohesive materials in thin section, and to distinguish single particles from aggregates of particles (e.g. when a single particle is micro-fractured and constituted by several sub-clasts, it allows to distinguish the n constituents of the particle). It suffers from a systematic bias, introduced by the truncation of coarser particles during thin section preparation, that may significantly change the real diameter of the particles analysed when heterogeneous materials are analysed. Furthermore, the number of particles analysed is limited compared with the other methods used for loose cataclastic materials.

5) The comparison between 2D and 3D values obtained by different methods is not always straightforward, even when 2D values are converted by the Sammis' law. A careful work is needed to minimize the bias introduced by the truncation of particles in 2D analyses and allow an effective comparison between 2D and 3D techniques.

6) Geological factors such as fault displacement and strain localization in shear bands certainly play an important role in determining the fractal dimension of carbonate fault core rocks. Nevertheless, the lack of clear scaling relationships indicate that analytical technique constitutes the major control on the variability of fractal dimension.

Therefore, we suggest the following guidelines for carbonate fault rock analysis (and other similar materials) depending on rock's cohesion, grain size distribution and available equipment:

For coherent materials, both homogeneous and heterogeneous, the use of 2D multiscale image analysis is strongly recommended. The possibility to have a strong microtextural control on the fabric of the sample is fundamental in the study of fault core rocks, especially in carbonates, where aggregates of particles are frequent. In addition, the samples' fabric in fault core rocks gives important information on the amount of comminution and the processes involved in fault deformation.

For loose material, the use of 3D optical granulometer, which gives a very precise grain size distribution within a narrower size range, is recommended for homogeneous samples but may provide bias in strongly heterogeneous cataclastic samples. The use of laser granulometer is suggested when a fast calculation of grain size distribution over a wide range of grain size is needed, particularly, for more resistance quartz-dominated fault core rocks. For carbonate fault core rocks and other weak samples, we recommend the use of wet laser granulometry at 0% ultrasound energy. This simultaneously helps to minimize particles fragmentation.

2.8 Acknowledgments

We are grateful to Renée Heilbronner and another anonymous reviewer for their valuable and constructive revisions. They significantly helped to improve the early version of the manuscript. Alfatest Srl is acknowledged for kindly making available to us the Malvern Morphologi 4-ID optical granulometer. A. Papa (Alfatest Srl) is particularly thanked for the valuable support during laboratory analyses. We are grateful to A. Comelli (University of Parma) for the accurate preparation of thin sections. Author's contribution: S. Cortinovis participated to fieldwork, acquired and interpreted data, and wrote the manuscript; F. Balsamo participated to fieldwork, collaborated in

data interpretation, and critically reviewed the manuscript; F. Storti collaborated in data interpretation and critically reviewed the manuscript.

3 Structural architecture and in-situ shattering along the active Monte Marine Fault, Central Apennines (Italy)

S. Cortinovis, F. Balsamo, M. Fondriest, F. La Valle, G. Di Toro

3.1 Abstract

The NW-SE-trending seismogenic Monte Marine Fault (MMF) consists of two major hard-linked segments and is characterized by a master fault surface with normal kinematics and minor subsidiary faults in the exposed footwall within Mesozoic carbonates. The structural architecture of the fault varies significantly along strike. The linkage between the northwestern and the southeastern fault strands occurs in correspondence of a step-over zone characterized by E-W trending faults with oblique slip, where anomalous amounts of loose materials resembling in-situ shattered rocks originate characteristic bad-land morphologies. To the Northwest, where the structural architecture of the fault is simpler and characterized by pure extension, most of the fault-related deformation is localized along the major slip surface. Comprehensively, the off-fault damage is about 40-50 m thick in the Barete area. Conversely, the thickness of the loose material increases significantly, up to 500 m, in the step-over zone, and particularly at the intersection between inherited thrust faults and Quaternary normal faults near the village of Pizzoli. In this study, we present a multi-disciplinary dataset that includes field mapping and laboratory data to study the role of the structural architecture and inherited structures on the origin and spatial distribution of fault rocks (ultra-cataclasites, cataclasites, proto-cataclasites, breccias and shattered rocks). We also discuss the possible mechanisms of deformation responsible for the actual configuration of the MMF, where we hypothesize mechanisms varying from in the situ-shattering to the strain localization.

3.2 Introduction

Fault zones are commonly defined as heterogeneous and structurally anisotropic discontinuities in the upper crust that control sub-seismic fluid flow and seismicity (e.g. Caine et al., 1996). Earthquake faulting in seismogenic fault zones occurs with the instantaneous release of elastic energy stored during the interseismic periods (Kanamori, 1994). In natural fault zones, master faults are generally decorated with cataclastic fault core rocks of variable thickness, extending for few tens of meters (Micarelli et al., 2006; Solum and Huisman, 2016). Fault core rocks in carbonates result

from a set of mechanisms (Billi and Storti, 2004; Storti et al., 2007) that contributes to enhance particles comminution and reduce rock porosity and permeability. Fault-related deformation produces cataclasites and ultra-cataclasites by "*grinding*", which consists of breaking particles in smaller pieces, "*abrasion*" that is the process of scraping or wearing particles away, and "*sliding*" and "*rolling*" that consist of combined rotation and translation of particles. These mechanisms were recognized at the micro-scale not only in carbonate fault rocks but also in gouges of different composition (Billi and Storti, 2004; Balsamo and Storti, 2010, 2011; Billi, 2010) and partly reproduced in the laboratory (Anthony and Marone, 2005). On the contrary breccias, another type of fault core rock, are produced by rock fracturing without sliding and rolling of particles. In contrast with fault core rocks, most of carbonate fault damage zones, which are usually much wider than fault cores, are composed of well-organized fracture systems that may enhance fluid circulation (Micarelli et al., 2003; Kostakioti et al., 2004; Agosta and Aydin, 2006; Frost et al., 2009; Hausegger et al., 2010; Savage and Brodsky, 2011; Choi et al., 2016) Original bedding is usually preserved in the rocks of the damage zone.

Next to the classical definition of fault rocks, in the last decades several authors described anomalous thickness of deformed rocks occurring along seismogenic faults in carbonate rocks (e.g., Fondriest et al., 2015). They called "in-situ shattering" the mechanism responsible for these volumes of fragmented rocks (Fondriest et al., 2015; Schröckenfuchs et al., 2015) resembling the pulverized rocks originated by the earthquake rupture in the basement (Mitchell et al., 2011; Rempe et al., 2013). Shattered rocks usually result in badlands morphologies made of incohesive, in situ fragmented materials extending for several meters to hundreds of meters from the master fault (Fondriest et al., 2015; Schröckenfuchs et al., 2015). Despite in-situ shattered rocks were described in active tectonic settings, still the mechanisms of their formation and the factors controlling their distribution along active faults in carbonate rocks are poorly investigated. Recent studies suggest that the formation of shattered rocks is associated to complex array of faults that overall contribute to enhance rock fracturing in seismogenic and active faults. This is particularly evident in the central Apennines that present various examples of thrust faults inherited from the Apennine compression associated to hundreds of meter wide loose carbonates (La Valle, 2019, master thesis).

In this study, we describe different types of fault rocks and document their thickness variations along the seismically active Monte Marine Fault (MMF) in the central Apennines (Italy) by combining detailed field mapping with structural and microstructural analyses on hand samples and thin sections. The MMF is a seismogenetic NW-SE trending extensional fault bordering the Eastern flank

of the Upper Aterno Valley, NW of the L'Aquila town. The MMF was partially reactivated during the 1703 earthquake (Moro et al., 2002, 2016; Galli et al., 2011; Falcucci et al., 2015) and is characterized by the occurrence of cataclasites, breccias and shattered rocks developed in Mesozoic carbonates exposed in the footwall block. The latter are hardly distinguishable from breccias in the field, but it seems that they extend for several kilometers along the fault, from NW to SE, and increase in thickness to the central and southern part of the fault zone, where several bad-lands shape the appearance of the fault near the villages of Pizzoli and Arischia.

The aims of this work are (1) to qualitatively reconstruct the structural architecture of the MMF, (2) to quantitatively describe fault core rocks (ultra-cataclasites, cataclasites, proto-cataclasites, breccias and shattered rocks) exposed in the footwall block and describe their thickness variations along the fault strike, and (3) to investigate the role of inherited structures in the development of the fault zone and in the formation of high deformed rocks along the fault. The multi-disciplinary and multi-scale approach used in this study allowed us to propose a hypothesized evolutionary model to describe the formation and evolution of the MMF rocks during the seismic cycle.

3.3 Geological setting

3.3.1 The Upper Aterno Valley

The Central Apennines of Italy belong to the Late Oligocene to Present fold-and-thrust belt related to the W-subduction of the Adria plate under the European plate (Doglioni, 1991; Carminati et al., 2004, 2012). The Central Apennines display a set of NE verging thrusts, inherited from the compressional tectonics, and superimposed by NW-SE oriented active normal faults. This complex seismotectonic structure was responsible for the recent destructive seismic sequences (e.g., L'Aquila Mw 6.1, 2009; Amatrice Mw 6.0, 2016) developed from the Sibillini mountains (to the North) to the Avezzano basin (to the South). In this context, a curious seismic gap area is represented by the Middle Aterno valley (Fig. 11), which is a part of the Central Apennines Fault System (CAFS) (Tondi and Cello, 2003), also known as Central Apennines Downfaulted Area (CADA) (Ghisetti and Vezzani, 1999; Agosta and Aydin, 2006). This region was affected by the continuous deepening of the hydrographic network (Galli et al., 2011), accounted for the first basin excavation, and was later dissected by several seismogenic, extensional faults during Quaternary times (Ghisetti and Vezzani, 1999; Agosta and Aydin, 2006). The seismotectonic history significantly contributed to form the actual configuration of the Upper Aterno Valley, that presents attributes resembling other Quaternary basins of the Central Apennines (e.g. the Colfiorito Basin, the Fucino Basin, the L'Aquila Basin) (Cello et al., 1997). The Aterno valley consists of a NW-SE trending quaternary basin bordered

with seismogenic extensional faults. These faults, aligned and characterized by en-echelon geometries, correspond, from the South to the North, to the Monte Pettino Fault, the Mt. Marine Fault, the San Giovanni Fault and the Capitignano Fault. These seismogenic fault segments shaped the Eastern flank of the Aterno valley (Galadini and Messina, 2004), and are still potentially dangerous for the development of new seismic episodes in the Central Apennines.

3.3.2 The Monte Marine Fault

The seismogenetic MMF (Fig. 11) is located in the Central Apennines (Italy) and develop in partially dolomitized carbonate rocks of the Lazio-Abruzzi platform. In particular, the fault cuts through the Calcare Massiccio Formation (Early Jurassic) to the South and the Corniola Formation (Early Jurassic) to the North (Fig. 11). The MMF belongs to the NW-SE Monte Pettino - Monte Marine Fault system, which was originated started from the Late Miocene, when contractional deformation in the Apennine fold-and-thrust belt was overprinted by extensional tectonics in its axial portion (Ghisetti and Vezzani, 1999). The fault zone overall consists of a ~14 km long seismogenic fault (Galli et al., 2011) and was partially reactivated during the February, 2 1703 (Mw=6.7) seismic sequence that caused hundreds of fatalities along the Aterno Valley and in the near town of L'Aquila. The seismically active segment of the fault is 8 km long and extends from the Barete village to the Arischia village (Blumetti, 1995; Moro et al., 2002; Galli et al., 2011). Near Arischia, huge amounts (100-300 m thick) of loose material significantly shaped the footwall of the MMF creating bad-land morphologies easily recognizable at several km of distance from the master fault (Fig. 12a, b). The old and complex seismotectonic history of this fault zone is well documented (Moro et al., 2002, 2016; Galli et al., 2011; Falcucci et al., 2015). At least five events of surface rupture after the 6th-5th millennium B.C. (maximum recurrent interval of 7000 years) were registered along the active fault segment (Calamita and Pizzi, 1992; Cello et al., 1997; Galadini and Galli, 2000; Galli et al., 2011; Falcucci et al., 2015; Moro et al., 2016).

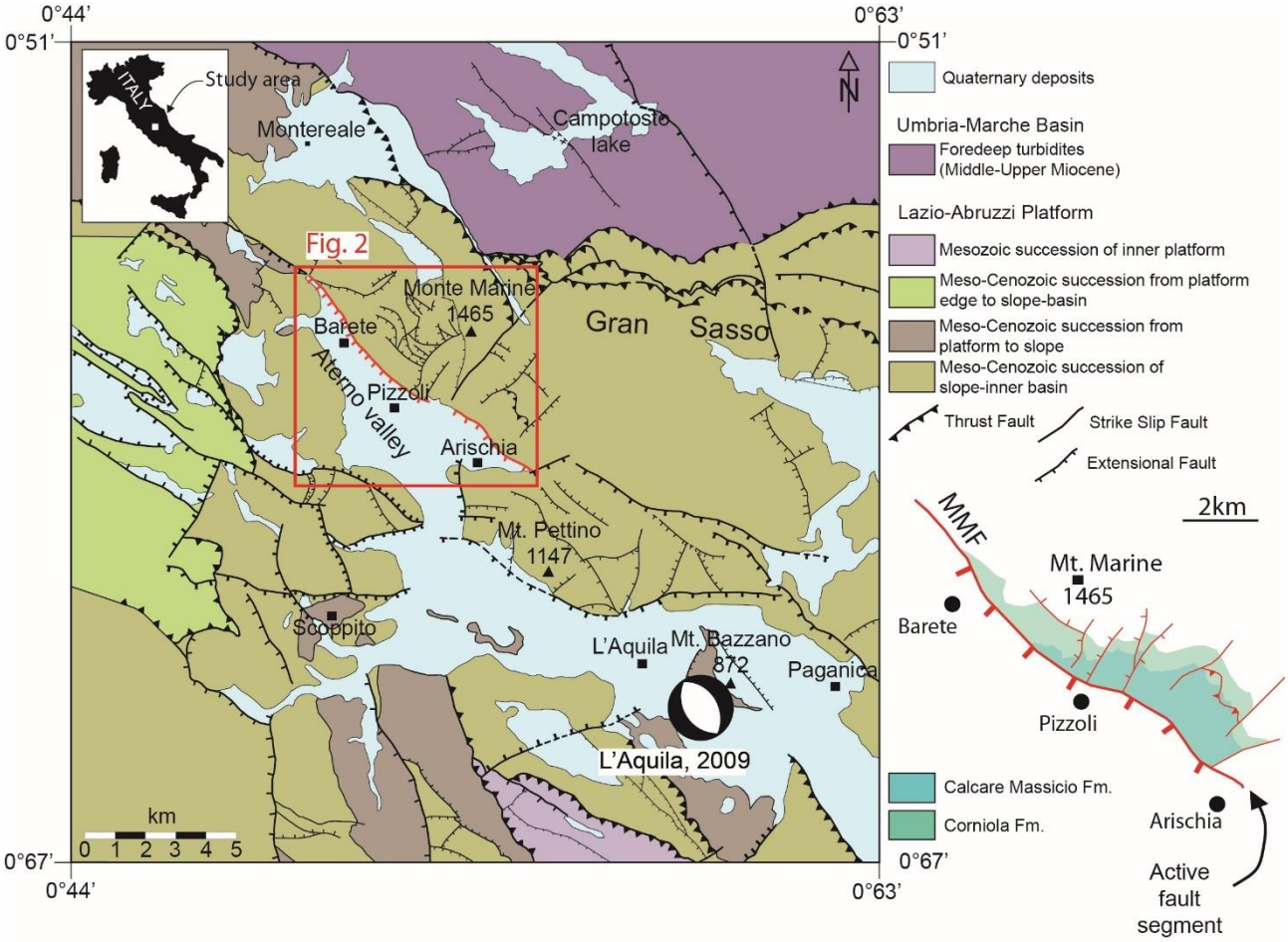

Figure 11: Simplified geological map of the Aterno valley with the location of the study area Northwest of the L'Aquila town. The fault zone is localized on Meso-Cenozoic succession of slope inner basin of the Lazio-Abruzzi carbonate platform and cut through the Calcare Massiccio Fm. to SE and the Corniola Fm. to NW.

3.4 Methods

3.4.1 Field mapping and structural analysis

We mapped two areas of interest (Barete and Pizzoli sites) located in the footwall of the main fault (Fig. 12a) at the 1:500 scale. Field mapping, based on orthorectified aerial photographs available on the website of the Regione Abruzzo (http://geoportale.regione.abruzzo.it/Cartanet), was aimed to map the main structural elements (i.e. the main fault and the subsidiary faults strands). We also constructed two geological cross-sections based on 1:500 and 1:5000 mapping. The first cross section, ~80 m long, was traced near the Barete village, while the second cross section, ~3 km long, was traced near the Pizzoli village (Fig. 12a). A total of 62 loose and coherent representative samples of cataclasites and fractured rocks, together with 862 structural data, were collected. Fault kinematics analysis was based on slickenlines preserved on principal and secondary slip surfaces. Fault pitch on striated surfaces was measured moving clockwise, and ranges from 0°

to 180°. Meso-scale field observations, combined with microstructural analysis, provide the basis for the classification of outcropping fault-related rocks in the different structural domains.

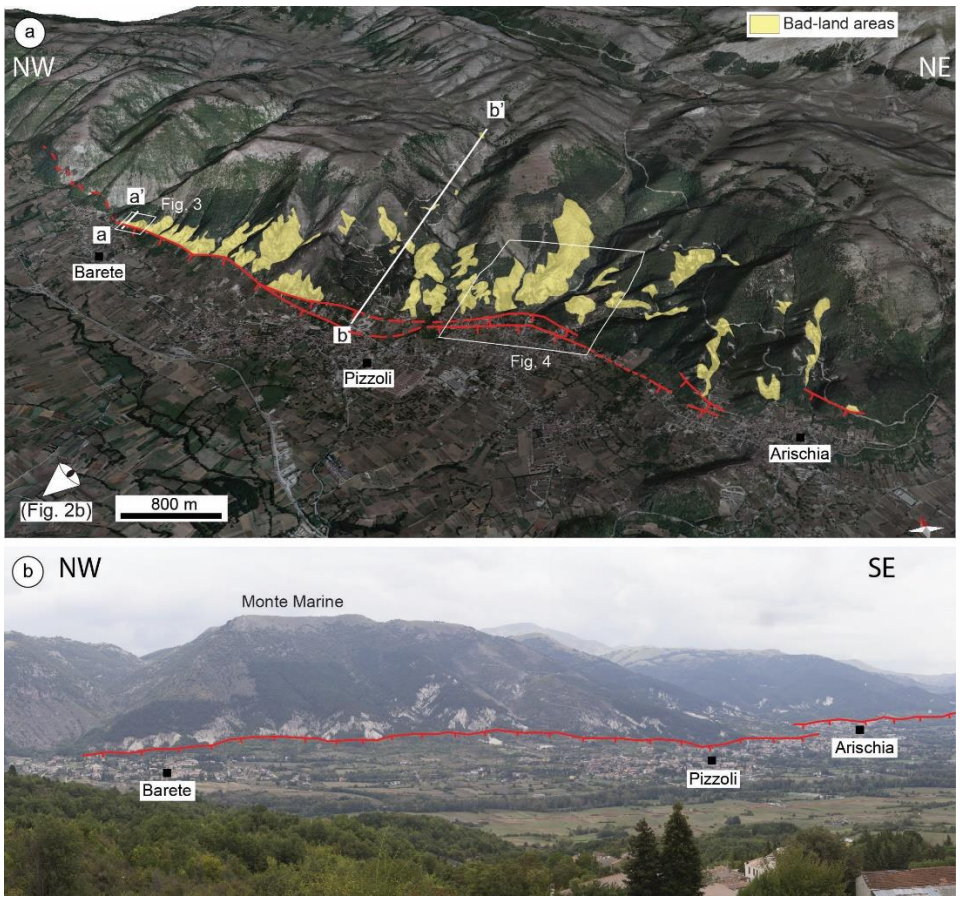

Figure 12: a) 3D view of the Monte Marine Fault (MMF) with indication of the main fault surface (red line in Fig. 2a), bad-land areas (yellow areas in Fig. 2a), cross sections (aa' and bb') and mapped areas (Fig. 2a). b) Panoramic view of the MMF.

3.4.2 Microstructural analysis

A total of 58 thin sections were analyzed under a petrographic microscope. Samples were impregnated with epoxy resin and sectioned perpendicular to the fault plane and parallel to slickenlines to obtain standard petrographic polished thin sections. They were analysed with the Zeiss Axioplan 2 Optical Microscope. Moreover, the most interesting samples were observed at the JEOL JSM 6400 Scanning Electron Microscope, at different magnifications, to examine microstructures in mm-thick slip zones. The EDS probe was adoperated to identify minor elements and distinguish dolomite crystals from calcite crystals.

3.4.3 Grain size and shape analysis

Four representative samples were analyzed using multiscale image analysis to calculate grain size and shape distribution in carbonate fault rocks, following the procedure described by Cortinovis

et al., 2019. Three samples are representative of the ultra-cataclasite, cataclasite and proto-cataclasite domains. We acquired a total of 53 images with the Zeiss Axioplan 2 optical microscope using different magnifications (1.25X, 2.5X, 5X, and 10X). We analysed more than one area for each sample at the same magnification to get a consistent number of particles for each sample. This operation was particularly useful in the coarse sample (i.e. proto-cataclasite and breccia), where images may contain a minor number of particles. We used the magnification 10x to analyse particles with diameter smaller than 25 µm, 5x for particles with diameter between 25 µm and 36 µm, 2.5x for particles with diameter between 36 µm and 94 µm and 1.25x for particles with diameter bigger than 94 µm. Before using these values, we made several tests to choose thresholds that allow acquiring precise values of aspect ratio and circularity (Pizzati et al., submitted). For each particle, we acquired the value of the equivalent diameter Deq, that corresponds to the diameter of a circular particle with the same area of the particle analysed. The fourth sample analysed corresponds to breccia (30x20x15 cm). Because of sample dimensions, this rock was cut with a diamond wire to obtain a fresh surface available for image analysis. In this case, we manually traced all the recognizable clasts on the fresh cut (each clast is delimited by opening-mode fractures) on a transparent paper that was scanned to obtain a digitalized image of the breccia texture. All grain size and shape data from the studied samples were obtained with the ImageJ software (Heilbronner and Keulen, 2006).

For grain size analysis, we manually traced the boundaries of particles to get their areal values. After that, we converted the obtained areas in values of equivalent diameter using the Eq. (1):

$$Deq = 2 * \sqrt{\frac{A}{\pi}} \quad (1)$$

For each sample, we sorted particles in a different number of size classes (classes thresholds were fixed to maximize the number of particles in each class) to build a diagram where the number of particles is plotted versus log. particle size. We also plotted, in a log-log. diagram, the cumulative number of particles versus log. particle size, thus obtaining the fractal dimension which corresponds to the slope of the power law best-fit line of the curve in the log-log distribution (Turcotte, 1986).

For grain shape analysis, we used the values of Aspect Ratio (AR) and Circularity (C). Aspect Ratio describes the elongation of particles and is obtained with the Eq. 2:

$$AR = \frac{Max\ axis}{Min\ axis}. \quad (2)$$

Circularity indicates the roughness of the perimeter of particles and is described by the Eq. 3:

$$C = \frac{4\pi Areal}{Preal^2}. \quad (3)$$

Both values of Aspect Ratio and Circularity were automatically calculated with the software ImageJ. These values are plotted in diagrams where the average values of AR and C for each size class is plotted in the 30 - 11500 μm size range. Data from ultra-cataclasites, cataclasites and proto-cataclasites were grouped in 12 size classes, while data from breccia were grouped in 6 classes.

3.5 Field data

In map view, the structural architecture of the MMF significantly varies along the fault strike (Fig. 12a). Overall, the fault zone is NW-SE oriented, similarly to the other active extensional faults in the Central Apennines and consists of two hard-linked NW-SE-trending segments. The off-fault damage, testified by the presence of the bad-land morphologies, increases from the Northwest to the Southeast, and extends in the footwall up to ~500 m (Fig. 12a, b). In the northern sector, near the Barete village, the fault segment is planar, whereas between the Pizzoli and the Arischia village the two fault segments are hard-linked by E-W faults (Fig. 12b). In cross section, the MMF structure consists of a well-developed cataclastic fault core of variable volume surrounded by a classical damage zone. The volume of the deformed material varies significantly along the fault and locally includes high amount of loose materials characterized by high fracture density and resembling the shattered rocks found along other faults of the central Appenines (e.g. Vado di Corno fault). At the outcrop scale, shattered rocks are hardly distinguishable from breccias.

3.5.1 The Barete site

In the Barete site, the main fault cuts through the Corniola Fm. (as described in the geological map of Vezzani and Ghisetti, 1998, inset in Fig.11) and measures 204/65 (dip dir./dip convention) (Figs. 13a and 15a), with slickenlines indicating dip-slip extensional kinematics (stereographic projection in Fig. 13a).

In the footwall block, the master fault surface is bordered with ~1-2 m thick layer of ultra-cataclastic, whitish and cohesive material (UC) (Figs. 13b, 15b). Next to ultracataclasites in the footwall, whitish and poorly cohesive cataclasites (C) outcrop in a 2-3 up to 8-10 m wide corridor (Figs. 13b, 15b). The thickness measured for these fault rocks suggest a cumulative km-throw extensional fault zone in accordance with the displacements estimated for other fault zones of the central Apennines that present a similar seismotectonic evolution starting from Triassic/Jurassic times (Tondi and Cello, 2003; Bigi and Pisani, 2005). Breccias (B) and proto-cataclasites (collectively in brown colour in Fig. 13a, b; Fig. 15c) are organized in ~20 m wide corridors parallel to the main fault. The transition from the fault core to the damage zone is marked by secondary synthetic and antithetic extensional faults

(Fig. 15b) while damage zone consists of fractured beds of dolomitized Corniola Formation. In this area we did not recognized evidences of shattered rocks (e.g. bad-lands morphologies).

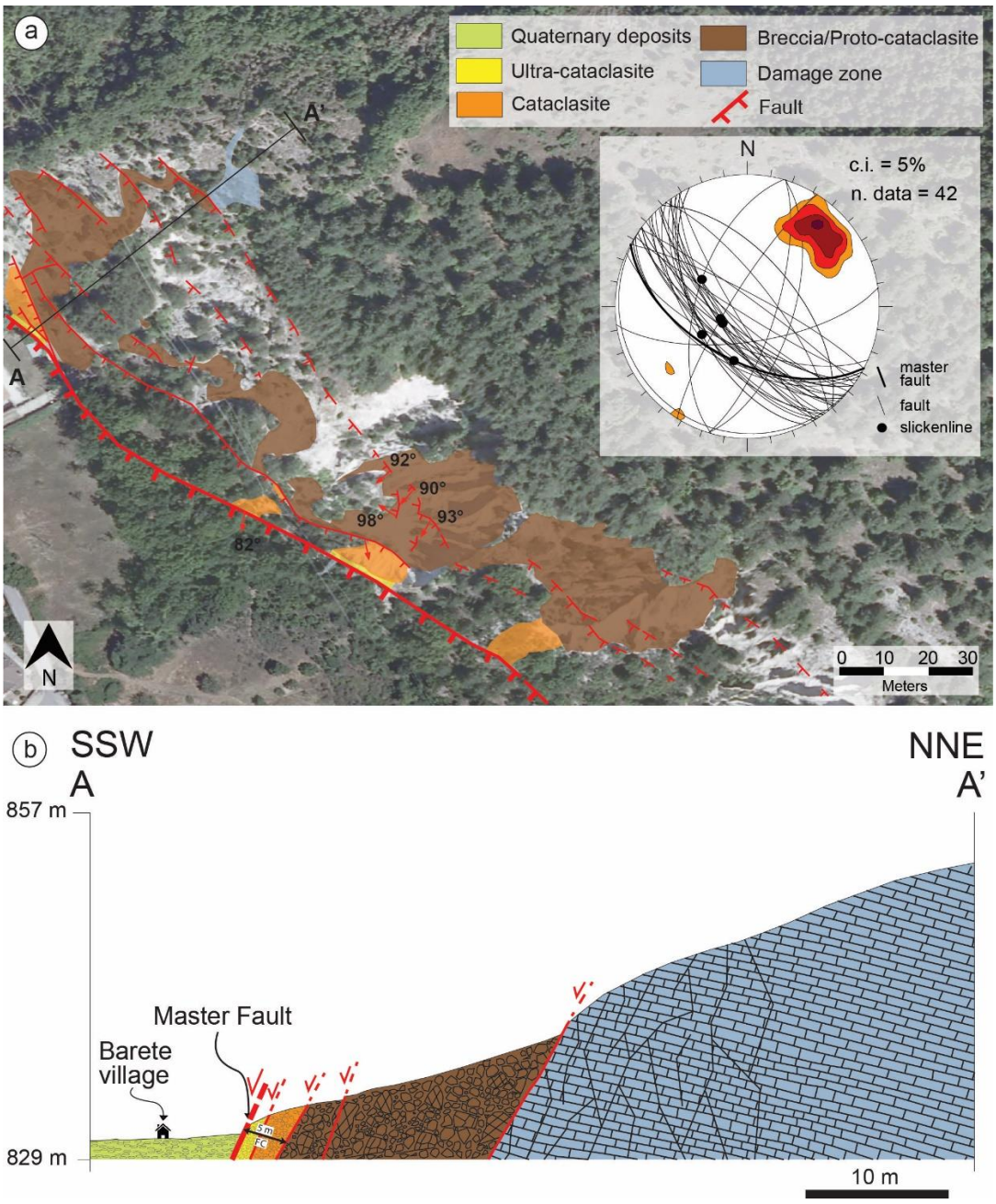

Figure 13: a) Geological map with stereographic projection of main faults and secondary faults and b) geological cross section of the Barete area with indication of different structural domains and major structural lineaments.

3.5.2 The Pizzoli site

In the Pizzoli site, the fault zone is structurally more complex than in the Barete site. Northeast of the Pizzoli village, the main fault surface strikes E-W and cuts through the dolomitized Calcare Massiccio Formation. Here, and particularly along the Sant'Antonio canyon, we documented a

significant increase in fault zone thickness and the presence of bad-land morphologies up to 600-700 m wide (Fig. 14a) filled of breccias mixed with shattered rocks. In this area, we recognized the same fault rock types of the Barete site (i.e. ultracataclasite, cataclasites, proto-cataclasites and breccias) (Fig. 14a), and also a Pleistocene slope breccia locally displaced by secondary faults (cf., Galadini et al., 2000; Moro et al., 2016). Extensional faults in this sector are scattered and mostly organized in NW-SE to E-W sets (Fig.14b). Fault slickenlines indicate oblique transtensional kinematics with pitch values between 50° and 130° (Fig. 14a, c). Low-angle thrust faults were also measured in this sector and are organized in conjugate systems with mean attitude of 206/26 and 042/24, respectively (Fig. 14a, d). Fault slickenlines on thrust faults indicate both NNE-SSW transport direction and oblique slip on lateral ramp (Fig. 14e). In this sector, cross cutting relationships indicate that thrust faults are overprinted by the extensional faults (Fig. 15d). Locally, NW-SE extensional faults sole out in the low-angle thrust faults (Fig. 15e). Finally, minor right-lateral strike slip faults, NNE-SSW oriented, were mapped (Fig. 14a).

A longer cross-section near the Pizzoli village allowed us to document the overall structure of the MMF in the over-step sector, and measure the thickness of the fault rock domains (ultra-cataclasites, cataclasites, proto-cataclasites and breccias) (section B-B' in Fig. 12). Based on cross section in Figure 6a, the ultra-cataclasites and cataclasites in the fault core are 2-3 m thick, while real thickness of proto-cataclasites and breccias is up to ~500 m (Fig. 16a). The loose breccias locally host 2-3 m-wide coherent, brecciated lithons with positive relief (Fig. 16c, d). Lithons generally preserve the original bedding (Fig. 16d) and are locally delimited by secondary faults with associated thin layers of cataclasites (Fig. 16b). In other cases, the boundary between loose breccias and the lithons consists of proto-catacalasites. The damage zone consists of fractured rocks and several minor synthetic and antithetic, NW-SE to E-W extensional faults (Fig. 16a, e). Further, a set of NE-SW extensional faults was measured. Overall, the kinematics of extensional faults ranges from pure to oblique transtension (Fig. 16e). Finally, we have also measured low-angle thrust faults with NW-SE orientation, and NW-SE and NE-SW strike slip faults. Thrust faults are cross-cut by extensional faults.

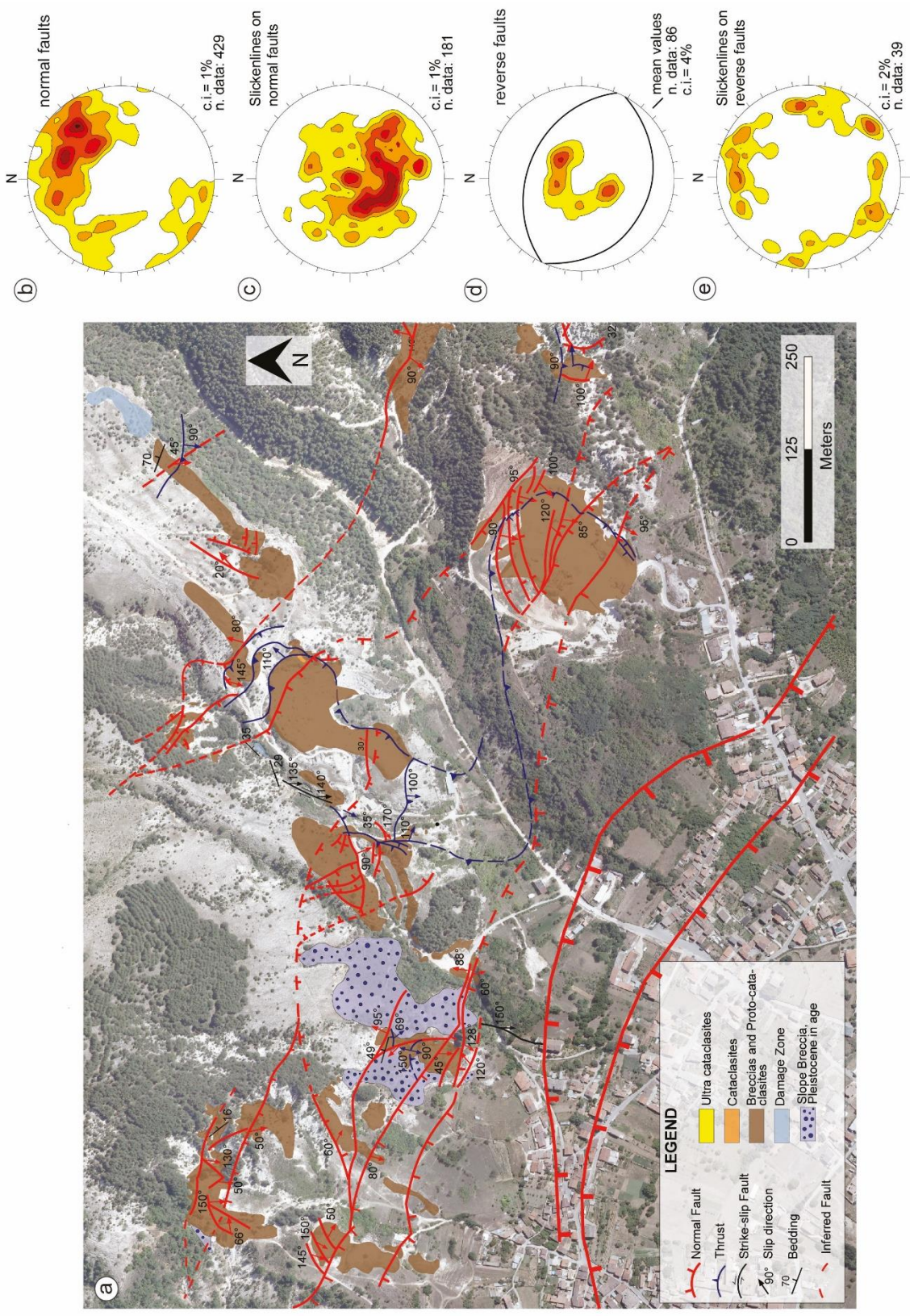

Figure 14: a) Geological map of the S. Antonio area with mapped structural lineament and fault rocks. The main fault surface was partially inferred by Moro et al., 2016; b) lower hemisphere, equal area projections of the measured normal faults, plotted as poles; c) slickenlines related to normal faults; d) reverse faults with mean attitudes (black lines in Fig. 4d) and slickenlines related to reverse faults.

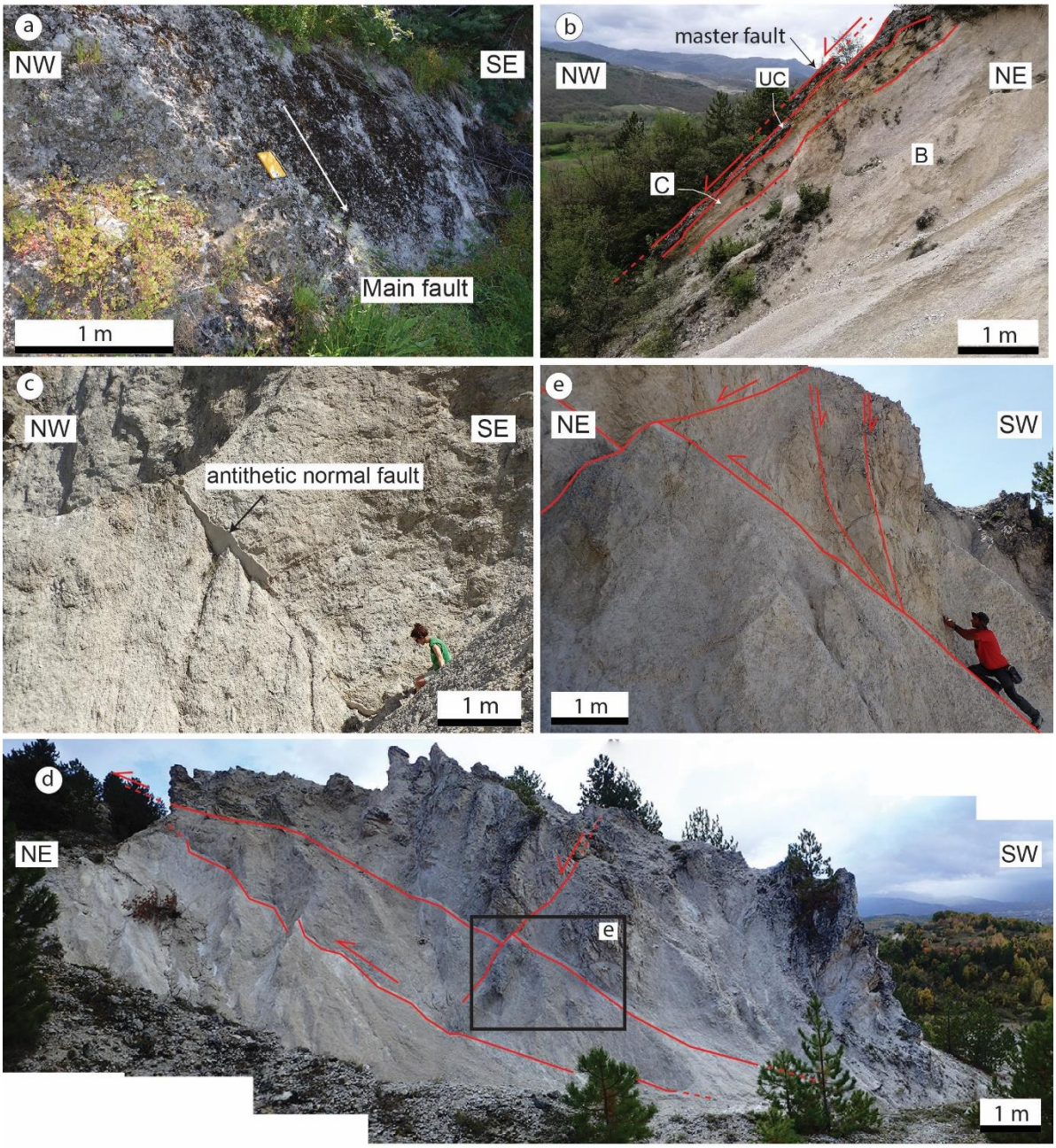

Figure 15: (a) Outcrop images showing the main fault surface in the Barete area; (b) a cross-section of the main fault and fault core; (c) an antithetic fault developed inside breccia near Barete; (d, e) reverse faults crosscut by extensional high angle faults near Pizzoli inside a bad-land areas.

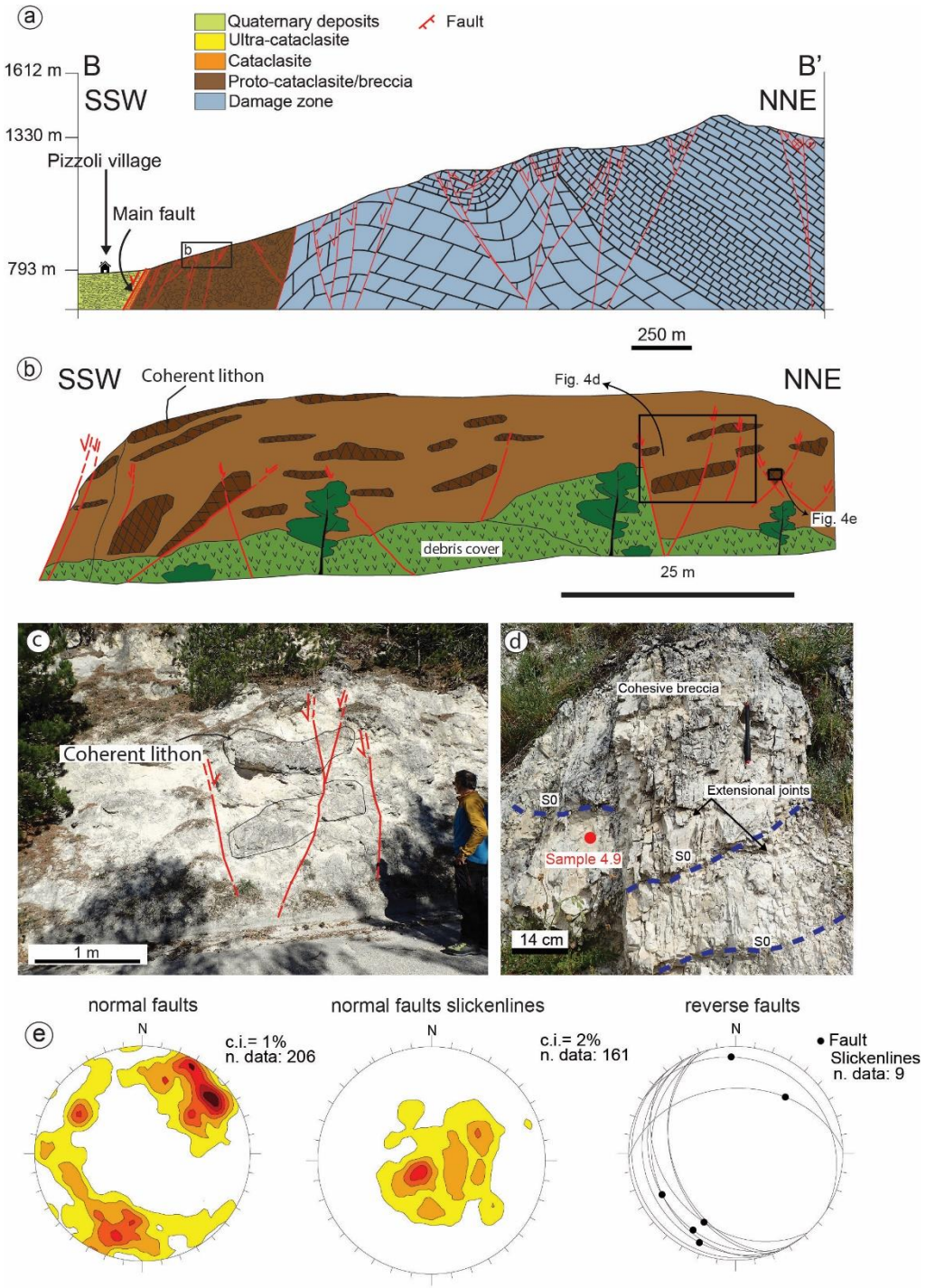

Figure 16: (a) Geological cross section of the Pizzoli area with indication of the different fault rocks, major structural lineaments, and bedding; (b) schematic diagram of the brecciated domain observed along the Pizzoli cross section; (c) image from the field showing lithons bordered and dissected by normal faults and (d) lithons affected by different sets of joints (e) lower hemisphere, equal area projections of the measured extensional faults with related slickenlines and reverse faults (black dots indicate slickenlines).

3.6 Fault rocks characterization

According to field observations, we found and studied several types of fault rocks developed in the fault core and in the damage zone, which include ultra-cataclasites, cataclasites, proto-

cataclasites, and breccias. Further, we have characterized the well-polished mirror-like slip surfaces developed along extensional faults.

3.6.1 Ultra-cataclasites

Ultra-cataclasites (UC) consist of white colour, fine-grained partially loose and stiff fault rocks composed of mm- to µm- size dolomite grains (Fig. 17a). At the microscale, UC is characterised by few sub-rounded big survivor grains (up to 4-5 mm in diameter) made of dolomite and minor calcite, bioclasts and chert (Fig. 18a, b, e), and a brownish matrix. The matrix is constituted by very comminute calcite and partially dolomite fragments that are not discernible at the optical microscope. Near Barete, the content of bioclasts and chert grains with respect to dolomite and calcite grains in the UC increases significantly. Near Pizzoli, ultra-cataclasites have a very different appearance made by prevalent dolomite clasts. This difference can be explained by lithological variations recognizable between the area of Pizzoli, where the master fault cuts through the Calcare Massiccio Formation, and the area of Barete, where the fault develops inside the Corniola Formation (Vezzani and Ghisetti 1998).

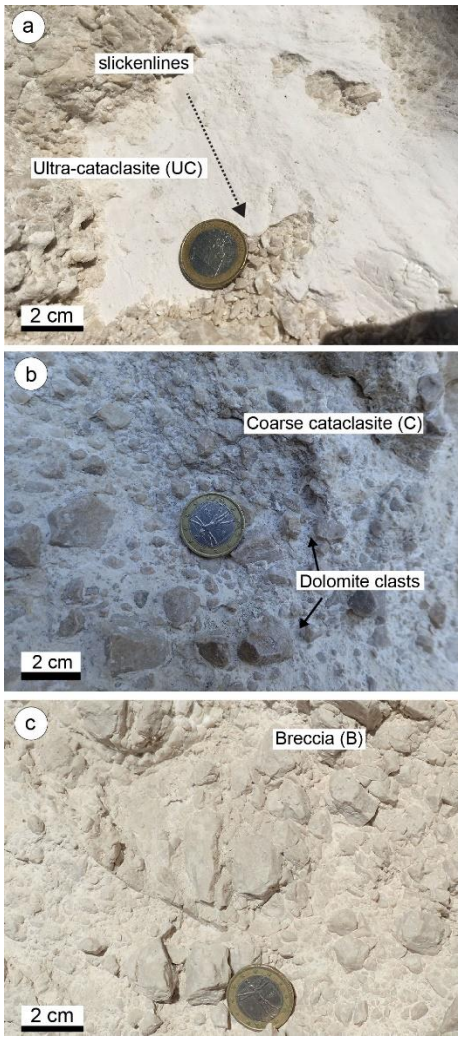

Figure 17: Images of different fault rocks recognized in the field: (a) ultracataclasites with slickenlines near Arischia; (b) coarse cataclasites formed by big dolomite clasts embedded by a white matrix of calcite near Barete (c), and breccias with coarser clasts of dolomite near Pizzoli.

3.6.2 Cataclasites

Cataclasites (C) consist of light grey, fine-grained, partially loose or cohesive fault rocks composed of µm- to mm- size sub-rounded dolomite grains (Fig. 17b). At the microscale, dolomite grains are embedded in a brown fine matrix made of more comminuted dolomite and calcite grains visible with difficulties at the optical microscope (Fig. 18c, d, f). Locally, cataclasites are affected by stylolites with accumulation of insoluble dark material (Fig. 18c), probably derived from calcite dissolution. Even some Fe-oxides are scattered over the thin section analyzed (Fig. 18c). Overall, cataclasites form up to ~2 m thick bands along the master fault and thinner layers along secondary slip surfaces in the fault damage zone.

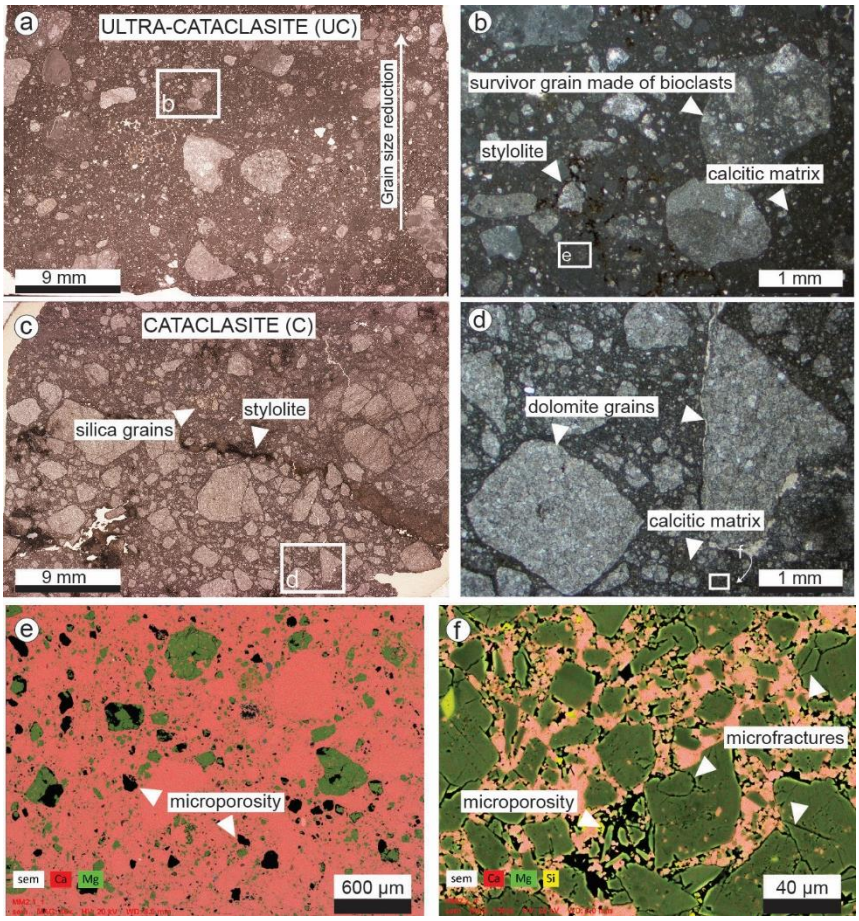

Figure 18: (a) Image of ultracataclasite and (b) detail from the same image at the optical microscope. (c) Image of cataclasites and (d) detail from the same image at the optical microscope. (e, f) Images from scanning electron microscope showing a detail on the matrix composition in the two samples analyzed.

3.6.3 Breccia and proto-cataclasites

Breccias (B) are formed by angular, cm-size dolomite grains characterized by high degrees of cohesion with respect to proto-cataclasites, cataclasites and ultra-cataclasites (Figs. 16d, 17c). Cohesion is locally given by rock cementation with microveins (from 1 to several mm thick) localized within the fracture array and filled by calcite and dolomite (Fig.19a). The rock slab in Fig. 19a shows a cemented fragmented carbonate (dolostone) where the individual fragments are neither rotated nor translated (Fig. 19a, b, c). The sample presents small pockets of proto-fault breccia in the upper left portion.

Proto-cataclasites (PC) are composed of mm- to cm-size sub-angular to angular grains of prevalent dolomite and minor calcite and chert.

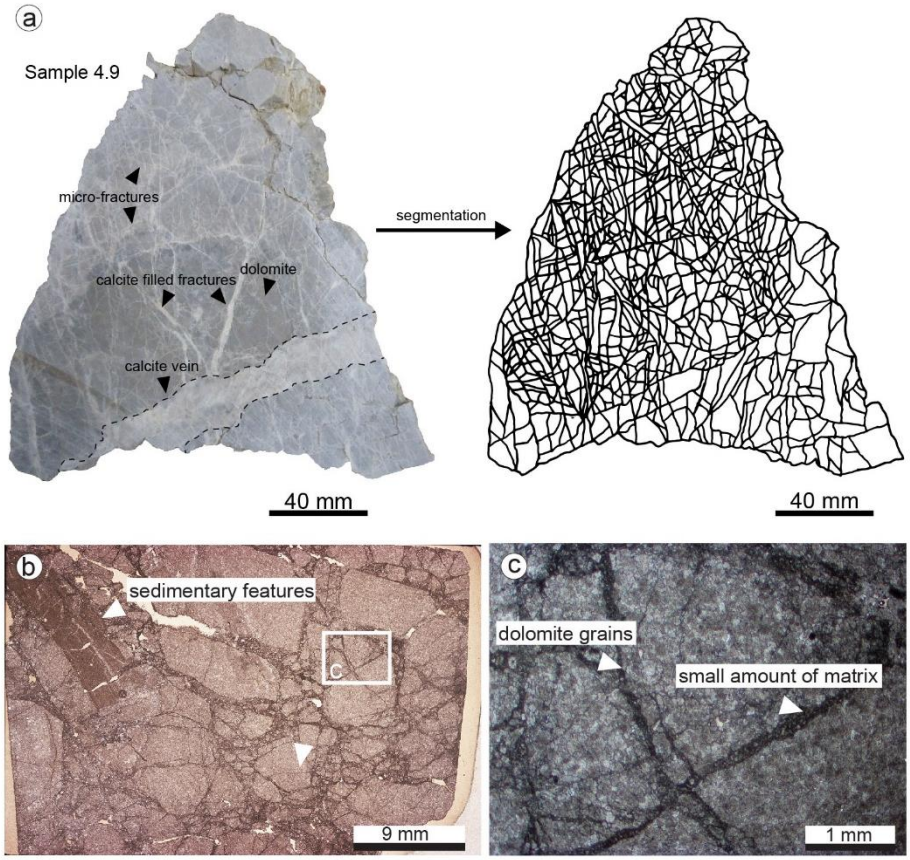

Figure 19: (a) Hand sample image showing micro-fractures and veins filled by calcite with related segmented image; (b) standard petrographic thin section representing breccia and (c) detail of dolomite clasts in breccia sample.

3.6.4 Slip surfaces

Samples collected in the field show evidences of extreme comminution, strain localization and, locally, co-seismic deformation. In very comminuted cataclasites, we recognized a significant grain size reduction toward the slip surface and locally in proximity of big clasts of dolomite that are partly fragmented and reduced to sub-angular and angular small fragments of the same composition (Figs. 20a, b, c, g and Figs. 21b, f). We also observed very angular clasts of dolomite produced by rock fracturing at the incipit of cataclasis in samples with more angular grains like proto-cataclasites (Fig. 21a). On very localized slip surfaces, we found a brownish, amorphous material at the optical microscope (Figs. 20a, b, c) and scanning electron microscope (Figs 21b, d, e). SEM-BSD analyses (Fig. 21e) proved that this amorphous material is prevalently composed of fragmented calcite. Calcite and dolomite crystals locally growth with very elongated shapes along sharp and rectilinear slip surfaces (Fig. 20d) with the major axis perpendicular to the slip plane. We observed that slip surfaces locally cut µm- to mm-size survivor grains of dolomite creating the so called “truncated clasts”, classified as evidences of co-seismic deformation at seismic slip velocity (Fondriest et al.,

2013) (Figs. 20c, d and Fig. 21d, g). At the optical microscope, we recognized flame-like structures, (Figs. 20e, f) consisting of dark and very comminuted material forming convolute-shape structures that resemble fluids. The composition of this material, obtained with the EDS point analysis, is partly dolomitic and partly calcitic. We documented the presence of calcite cement sealing porosity and micro-porosity developed among the big clasts of dolomite. (Fig. 20g and Figs. 21a, c, h).

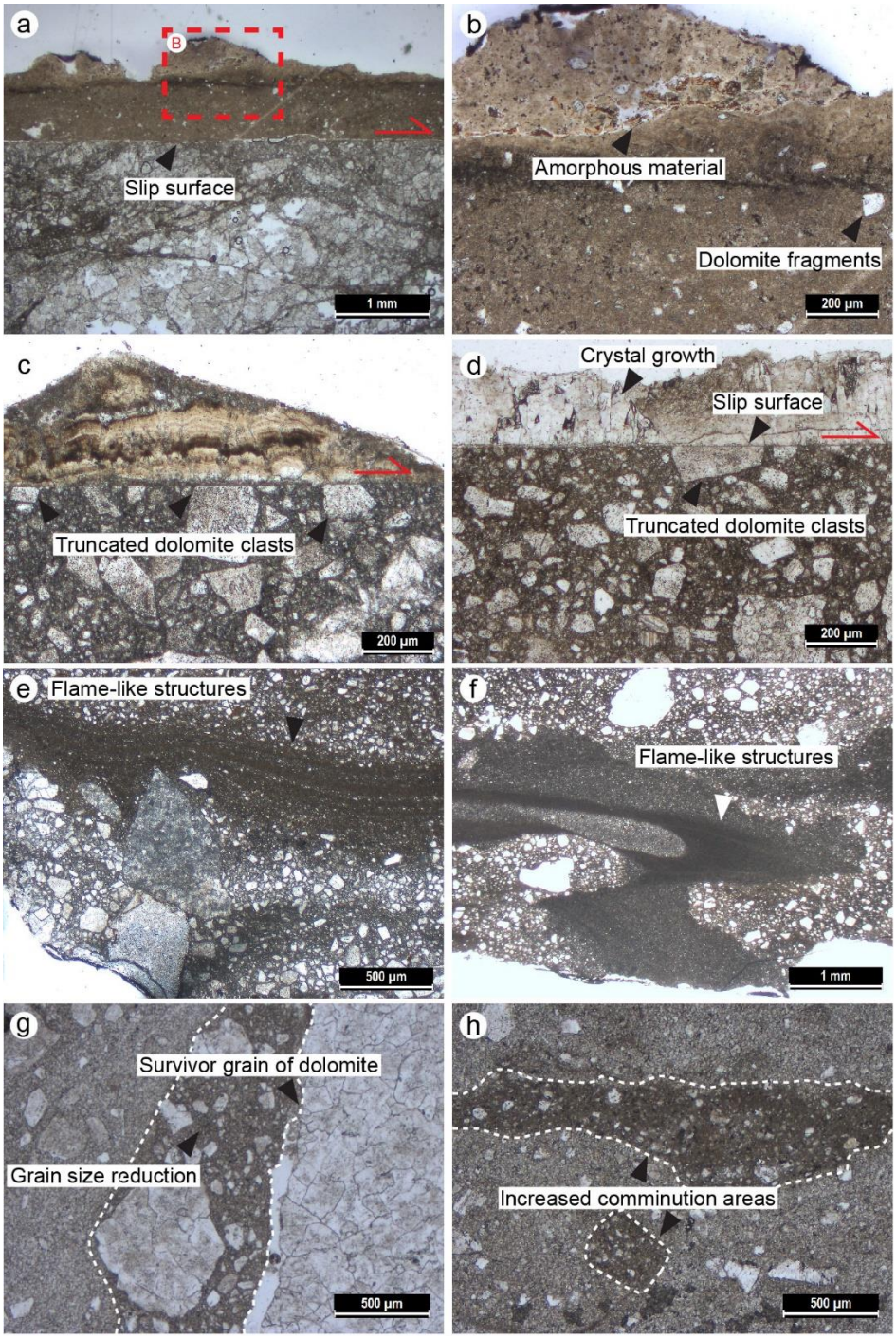

Figure 10: (a,b) Images from optical microscope representing slip surfaces with amorphous material, crystal growth and (c,d) truncated clasts of dolomite. (e,f) flame like structures formed by very comminuted material are represented by dark convolute shapes; (g,h) grain size reduction is visible along the main slip surfaces and near major dolomite clasts that experienced fracturing.

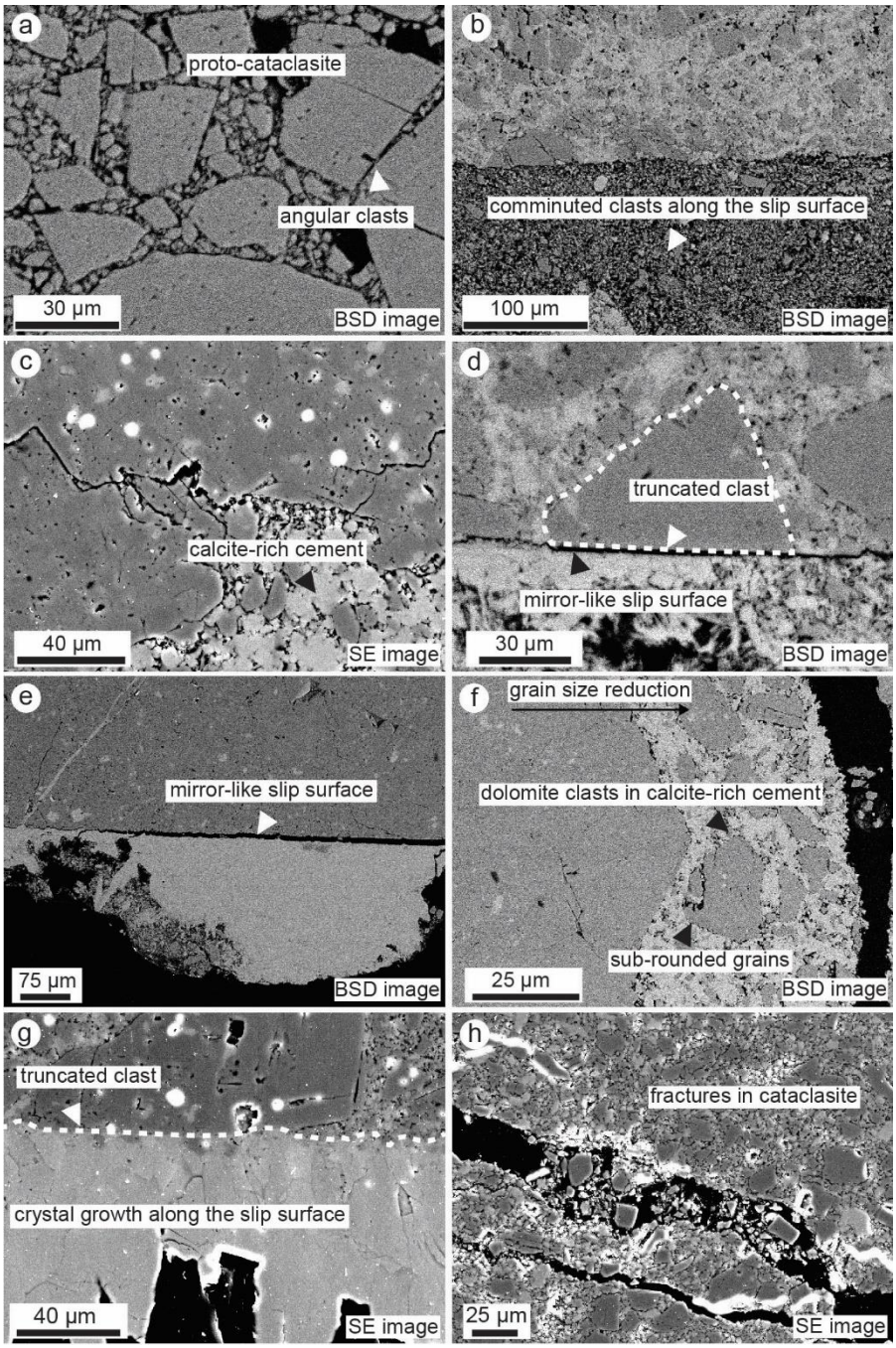

Figure 11: (a) Image from scanning electron microscope representing cataclasite and breccia samples and related microstructures: angular clasts broken by principal fracturing; (b) comminution along the slip surface; (c,f) calcite-rich cement crystallized inside pores and fractures; (d,e) truncated clasts of dolomite along mirror like slip surfaces; (g) crystal growth along the slip surface and (h) general framework produced by fracturing and cataclasis.

3.7 Grain size and shape data

3.7.1 Grain size distributions

Grain size distributions were calculated for all the four different domains described above, to compare the different rock samples from a petrophysical point of view. Results acquired with image analysis are shown in the two columns of Fig. 22 as frequency distribution, on the left side (Figs. 22a, b, c, d), and cumulative number of particles plotted versus size classes in a bi-logarithmic graph, on the right side (Figs. 22e, f, g, h). Frequency distributions overall show unimodal bell-shaped distributions with different peak values. Ultra-cataclasites have a mean value of 257.16, a mode of 186 and a median of 104.73 (Fig. 22a). Cataclasites have a very similar trend with respect to ultra-cataclasites, with a mean value of 322.57, a mode of 240 and a median of 225.26 (Fig. 22b). Proto-cataclasites have a grain size distribution that partly differ from that of ultra-cataclasites and cataclasites with a mean value of 539.46, a mode of 400 and a median of 451.37 (Fig. 22c). Lastly, breccias have a completely different curve shape with respect to the other domain. For breccias, we calculated a mean value of 3035.62, a mode of 4000 and a median of 2713.49 (Fig. 22d). Even in the shape of the bi-logarithmic graphs on the right of the figure we recognized some differences. The curves of ultracataclasite and cataclasite are well fitted by the power law linear best-fit over 1.5 orders of magnitudes (Figs. 22e, f), while data of proto-cataclasites show very irregular tendencies interpolated with difficulties by the straight line (Fig. 22g). Because of the minor number of clasts in the coarse samples, the granulometric curve obtained from data of breccia present less classes than the other domains and cannot be well interpolated (Fig. 22h). These differences in grain size distributions result in a diversity of 2D fractal dimensions that vary from D=0.98 in proto-cataclasites and breccias, to D=1.61 s and D=1.81 in cataclasites and ultra-cataclasites respectively. In the case of ultra-cataclasites, cataclasites and breccias, we got a very good correlation coefficient (R2=0.99). On the contrary, from breccias we got a lower value of correlation coefficient (R2=0.7). The amplitude of the size interval considered in the calculation of fractal dimension is indicated by the black lines sketched on the cumulative distributions.

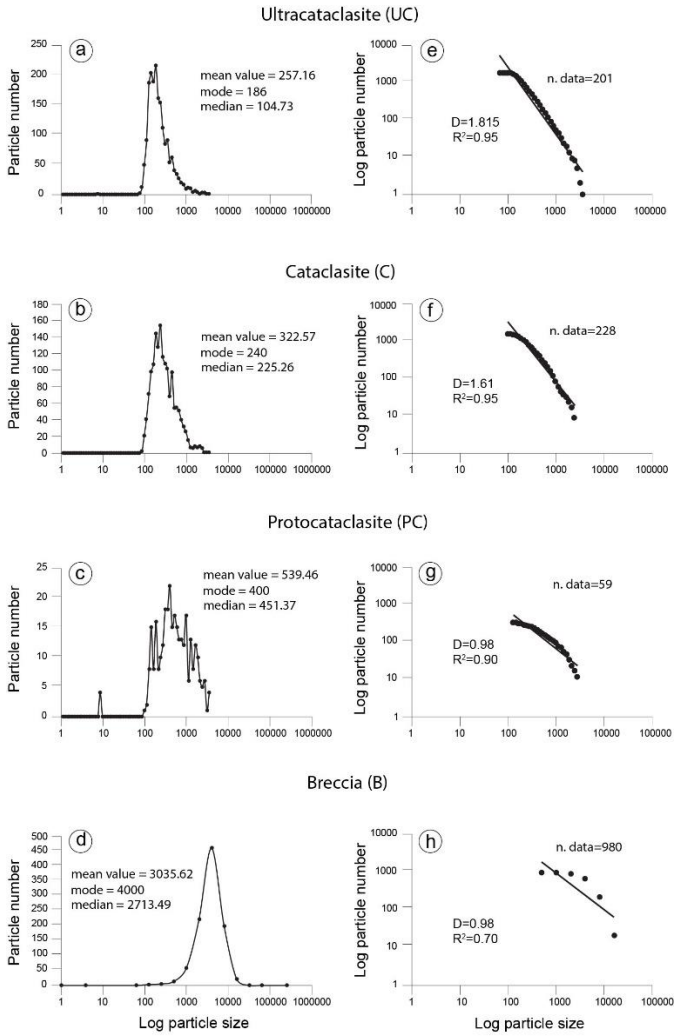

Figure 12: Frequency and log. cumulative distribution of particles plotted versus log. particle size for the four different samples analyzed with image analysis: (a,e) ultra-cataclasite, (b,f) cataclasites, (c,g) proto-cataclasite and (d,h) breccia. Values of fractal dimension obtained by fitting, with power low distribution, the cumulative distribution of particles are given for each domain and reported next to the curves.

3.7.2 Grain shape distributions

Grain shape distributions for all the samples analyzed are reported in Fig. 23, where we plot the values of circularity (Fig. 23a) and aspect ratio (Fig. 23b) versus log. grain size, with different colors representing different fault rocks (ultra-cataclasites, cataclasites, proto-cataclasites and breccias). Values from ultra-cataclasites, cataclasites and proto-cataclasites were calculated on images from thin sections and plot in the same size range (32 - 3000 µm); values of breccias were acquired from a hand sample and plot in another size range (855 - 11500 µm). These different procedures were dictated by the nature of the sample and their average grain size distributions. The standard deviations calculated for the values of each class are reported on the curves with black vertical lines (Figs. 23a, b). Value of Circularity (Fig. 23a) and Aspect Ratio (Fig. 23b) are plotted versus size classes.

In general, values of Circularity vary significantly for all the four samples analyzed and describe decreasing shape trends. The shape of the curve of proto-cataclasites is very irregular and probably influenced by the low number of data available for this domain. Ultra-cataclasites vary from 0.769 at 32 µm to 0.633 at 3000 µm, cataclasites initially increases from 0.6 at 32 µm to 0.8 at 75 µm and then decreases regularly down to 0.68 at 3000 µm. Breccias also vary slightly from 0.64 at 855 µm to 0.56 at 11500 while proto-cataclasites have a very different trend, with an oscillatory curve that reflects the heterogeneity of the sample but also the lack of data in the size classes analyzed (Fig. 23). Overall, ultra-cataclasites and cataclasites have higher circularity with respect to proto-cataclasites and breccias over the entire size interval analyzed. Similarly, for values of grain size higher than 855 µm, breccias have lower values of circularity with respect to all the other samples analyzed.

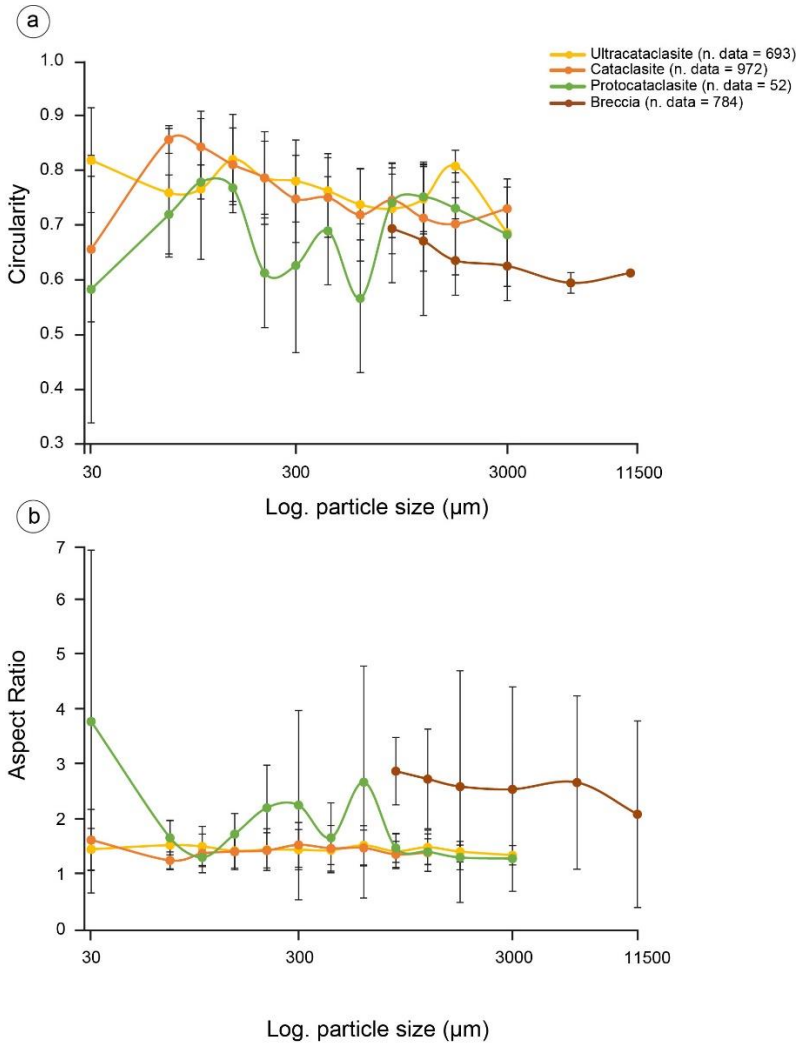

Figure 13: Grain shape distributions obtained for the four samples analyzed with image analysis. (a) Values of circularity and (b) values of aspect ratio. Both these values are plotted versus log. particle size. Results from the different samples are represented with different colors; standard deviations are reported for each size class and the number of data analyzed is indicated for each domain.

The values of Aspect Ratio, on average, vary less than that of circularity (Fig. 23b). In particular, proto-cataclasites and cataclasites have very similar flat trends of Aspect Ratio, with values varying from 1.65 to 1.31. On the contrary, proto-cataclasites confirm their complex trend that decrease, with significant oscillations, from the value of 3.8 at 32 µm to the value of 1.31 at 3000 µm. Finally, values obtained from Breccia form a curve that decreases from 2.9 at 855 µm to 2.1 at 11500 µm. Overall, Breccias and proto-cataclasites have values of Aspect Ratio much higher than that of ultra-cataclasites and cataclasites, which vary in the same range of values.

3.8 Discussion

3.8.1 Structural architecture along the MMF

As described in the previous chapters, the MMF has a very complex structural architecture that varies from NW to SE following the main fault plane. The Barete area is characterized by a very easy and linear configuration ascribable to pure extension (there are no evidences of strike slip and reverse kinematics in this fault sector) and extensional faults lie parallel to each other following the same direction. On the contrary, the Pizzoli-Arischia area presents crosscutting relationships among fault strands of different kinematics and age (e.g. extensional faults exploiting inherited low angle faults formed during the Apenninic compression, extensional faults cutting low angle thrusts, strike slip faults cutting extensional faults and strike slip faults cut by extensional faults). Near Pizzoli, the presence of EW and NW-SE right lateral and left lateral strike slip faults and transtensional faults can be interpreted in two different ways. 1) Strike slip faults developed during the quaternary extension constitute high-angle tear faults and worked to accommodate lateral variations in displacement between the Northern and the Southern sector of the MMF. 2) Strike slip faults correspond to inherited structures related to the formation of low angle faults in the Apennine compression and were partially reactivated during the quaternary extension as tear faults. Unfortunately, the presence of high amounts of loose rocks in the Pizzoli area often hides the original structures and does not allow to interpret unequivocally the crosscutting relationships between extensional faults and strike slip faults and, consequently, to explain the formation of strike slip faults and give them a relative chronology. In any case, the presence of several subsidiary synthetic faults in the fault core of the main fault together with the presence of huge amounts of shattered rocks between Pizzoli and Arischia, testify that off-fault damage is distributed over a wide area.

3.8.2 Distribution and origin of fault rocks

The amount of deformed rocks varies along the MMF. It overall increases from the North to the South, where huge amounts of loose fault rocks form characteristic bad-land morphologies along the fault strike. The classical definition of fault core includes both cataclasites and breccias and the normal thickness of fault core rocks varies from few cm to 1-2 m (e.g. the Venere Fault, the Pirgaki and the Helike Faults in the Gulf of Corinth) (Micarelli et al., 2003; Agosta and Aydin, 2006). In accordance with this definition, the fault core of the MMF, hundreds of m wide, is out of range with respect to that of other faults developed in carbonate rocks. This partly derives by the difficulties to place the boundary between breccias and shattered rocks, which are hardly distinguishable from breccias. We recognize as shattered rocks the amounts of loose materials produced by fracturing and characterized by a very high fracture density. The presence of high volumes of loose material suggest a different mechanisms of deformation with respect to brecciation.

In the central part of the fault zone, NE of the Pizzoli village, the thickness of fault rocks is maximum and we documented up to 50 cm thick ultra-cataclasites on low angle faults surrounded by m-thick proto-cataclasites and breccias, and high amounts of shattered rocks. In this area, the amount of loose material is associable to the presence of three important stacked thrusts with NNE-SSW orientation. The fault slickenlines measured on these faults indicate both NNE-SSW transport direction and oblique slip on lateral ramps that mean stress field variations during time, including reactivation of thrust faults during extension. This is also testified by the crosscutting relationship between compressional structures (e.g. SC-planes) measured near thrust faults and extensional shear planes and joints (Riedel fractures associated to normal and strike slip faults).

To the North of the fault zone, where the mean attitude of the main fault is 204/65 (dip dir/dip) and the secondary normal faults follow almost the same orientation, deformation is less intense and confined to the master slip surface. Overall, the distribution of fault rocks suggests a direct correlation between the structural complexity of the fault and the amount of damage changing along the fault zone. This observation was already presented by Demurtas et al., 2016 and Fondriest et al., 2015, that described the occurrence of shattered rocks in carbonate fault rocks affected by a complex and multi-stage evolution. Moreover, field evidences and data from the literature suggests that the formation of shattered rocks is common in dolomitic rocks, where the development of new fractures is facilitated by the rock's stiffness (the Young's Modulus of dolomite, ~ 116 GPa, is higher than that of calcite, ~ 84 MPa) (Mavko et al., 2009). High values of both shear and bulk moduli also affect the brittle behaviour of carbonate rocks at shallow crustal levels. The presence of such

volumes of shattered rocks and their distribution along the fault is particularly interesting since they could play an important role to adsorb part of the elastic energy released during the earthquake rupture. Ma and Andrews (2010) and Okubo et al. (2019) proved that off-fault damage adsorbs part of the energy available during earthquakes, thus causing the reduction of radiation and kinetic energy available for seismic waves propagation. Okubo et al., 2019 also found that off-fault damage can delay the transition from sub-Rayleigh to supershear speeds at a fixed depth and modeled the evolution of fracture network proving that, in case of strike slip faults, the complexity of the fracture density increases with depth even though damage zone width decreases. In our case, it would be interesting to investigate the presence of shattered rocks at depth by using geophysical tolls (e.g. seismic and geoelectric investigations) to validate the model even on extensional and complex faults, which are more difficult to reproduce with numerical models.

3.8.3 Aseismic and coseismic fault rocks

The rock types mapped along the MMF are classified on the base of grain size and shape distributions and different deformation mechanisms. Fault core is formed by cataclasites, proto-cataclasites and partially breccias, which also highlight the transition from the fault core to the damage zone. Ultra-cataclasites are localized along major slip surfaces and experience a major grain size reduction (2D=1.815), while cataclasites form thicker layers along fault planes and undergoes a less intense deformation (2D=1.61). We think that even proto-cataclasites (2D=0.98), which separate cataclasites from breccias, partially experience cataclasis, even if at a less extent with respect to ultra-cataclasites and cataclasites. Breccias are characterized by a value of fractal dimension equal to that of proto-cataclasites (2D=0.98) even though they are originated by pure fracturing (i.e. without grains rolling and sliding). As proved by results from image analysis (Fig. 23), ultra-cataclasites and cataclasites have more rounded grains than proto-cataclasites and breccias in the entire range of size classes analysed. In fact, these rocks are progressively smoothed by cataclasis that operates to form more equidimensional grains than that of proto-cataclasites and breccias, characterized by elongate clasts. The presence of shattered rocks is attributed to the mechanism of in situ fracturing with a very high frequency of micro-fractures that overall contribute to create high volumes of loose material resulting in bad-land morphologies (Mitchell et al., 2011; Fondriest et al., 2015). Breccias and shattered rocks are hardly distinguishable in the field. Nevertheless, we did not perform microstructural investigation on shattered rocks then we can not compare the two domains from the petrophysical point of view. Anyway, as sketched before, the

presence of shattered rocks generates some problems in the classical definition of fault core thickness along the MMF.

3.8.4 From rock shattering to strain localization

The coexistence of shattered rocks and ultra-comminuted cataclasites along the MMF indicates the heterogeneity of deformation mechanisms operating during the seismic cycle (Fig. 24). In the case of the Monte Marine Fault, rock shattering is prevalent at the scale of the fault (the off-fault damage width is up to 3 km) while progressive strain localization causes rock comminution along the major slip surfaces (Fig. 24b). When faults move for creeping, progressive strain localization forms breccias that evolve into grain-supported proto-cataclasites made of angular to sub-angular survivor grains with quite elongated shapes formed by *bulk crushing* and *intragranular Extensional Fracturing*. Proto-cataclasites further evolve into cataclasites and ultra-cataclasites through the processes of *chipping*, *grinding*, *abrasion*, *sliding* and *rolling* that produce matrix-supported faults rocks made of sub-rounded to rounded survivor grains (Billi and Storti, 2004; Anthony and Marone, 2005; Balsamo and Storti, 2010, 2011; Billi, 2010) (Fig. 24b). The mechanisms of progressive grinding, abrasion, sliding and rolling explain the values of circularity and aspect ratio measured in the different rock domains. At the same time, the reactivation of reverse faults with normal or oblique kinematics can also occur if favored by the orientation of the preexisting faults with respect to the new stress field (Fig. 24b). This is proved by the kinematic indicators measured on low-angle faults along the MMF testifying the reactivation of 20°N oriented thrusts under extension. In the case of earthquake rupture, faults reactivation and strain localization occur contemporaneously to in-situ shattering, responsible for developing the high amounts of deformed rocks with high fracture density. We hypothesize that the formation of shattered rocks could be related to the passage of seismic waves in the fractured damage zone and fault core. Contemporaneously, at seismic slip velocities, mirror-like slip surfaces develop along fault planes produced by extreme abrasion between the fault blocks (Fig. 24c). The complexity and variability of the resulting fault rocks along the MMF seems to be caused by the contribution of several seismic and aseismic fault reactivations in a cyclic evolution (Fig. 24).

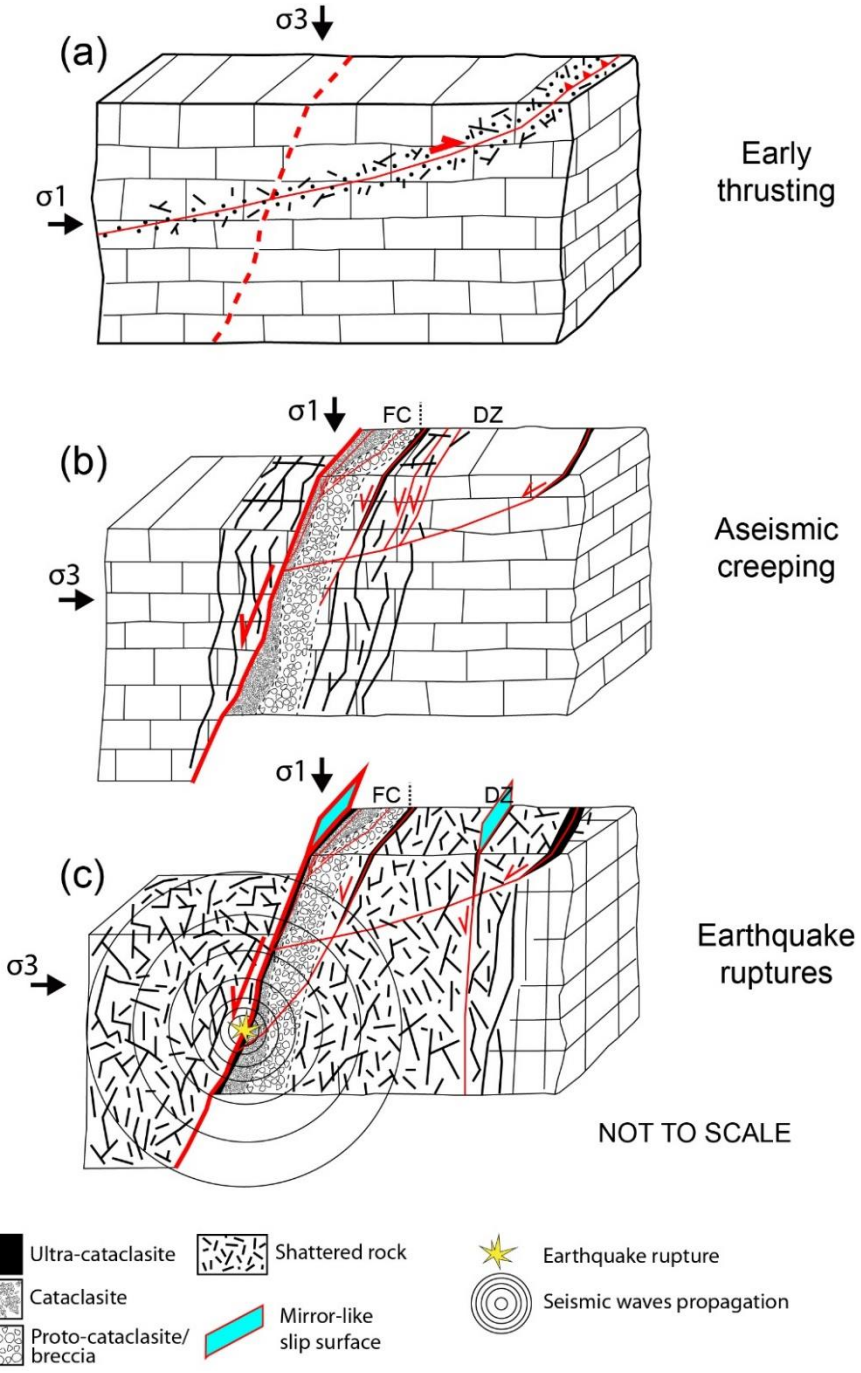

Figure 14: Not to scale cartoon showing the evolution of fault rocks in the studied area due to the progressive re-activation of extensional faults through time during the seismic cycle. (a) Early thrusting produces thrust faults during the Apennine compression; (b) progressive strain localization occurs along the main slip surface and subsidiary faults during aseismic fault creeping; (c) in situ shattering is likely activated during the earthquake rupture and favored by seismic waves propagation. The effect of seismic waves propagation is major where extensional faults cut through inherited thrust faults. During earthquake, mirror-like slip surfaces develop along the fault planes. By definition, the fault core here includes ultra-cataclasites, cataclasites and breccias.

3.9 Conclusions

To conclude, we summarize the previous discussion with few points that include the most important results from our study:

- The Monte Marine Fault is a complex fault zone that presents significant structural heterogeneities along the fault strike and huge off-fault damage. The major complexity is recognizable in the central and southern part of the fault, where structures of different kinematics intersect producing an increased amount of loose fragmented material and cataclastic rocks.
- The fault core thickness varies along the fault strike and is maximum between the area of Pizzoli and Barete. In this fault sector, the fault core is out of scale with respect to its classical definition due to the presence of shattered rocks that are hardly distinguishable from breccias.
- The type of fault rocks developed along the fault reflects different mechanisms of deformation, which vary from pervasive in-situ shattering at high slip rates during earthquake rupture to progressive strain localization along faults during fault creeping. This results in a cyclic evolution with alternated phases of aseismic creep and seismic rupture.
- The presence of in-situ shattered rocks and microstructural evidences of coseismic slip testify that the fault zone was seismically active and likely experienced several events of surface rupture at high slip rates.

3.10 Acknowledgments

We thank A. Comelli (University of Parma) for the accurate preparation of thin sections. We thank L. Barchi (University of Parma) for the support during SEM analyses. Author's contribution: S. Cortinovis participated to fieldwork, acquired and interpreted data, and wrote the manuscript; F. Balsamo and M. Fondriest participated to fieldwork, collaborated in data interpretation, and critically reviewed the manuscript; F. La Valle participated to fieldwork and elaborated field observations and structural data, and G. Di Toro participated to fieldwork and critically reviewed the manuscript.

4 Dry vs wet deformation processes during seismic slip under fluid pressurized conditions in natural carbonate fault gouge

S. Cortinovis, S. Aretusini, M. Nazzari, G. Di Toro, F. Balsamo

4.1 Abstract

Seismic rupture propagation is influenced by the presence of fluids within faults. This is especially valid in carbonate rocks, where the occurrence of water in proximity of the slip surface favours the failure of asperities and consequently fault weakening. Experimental evidences showed that, at slip initiation, water-dampened gouges weaken faster than in room-dry conditions.

Here we present a series of friction experiments preformed with the Slow to HIgh Velocity Apparatus - SHIVA (HPHT lab, INGV, Roma) on a natural fault gouge of mixed dolomite (80%) and calcite (20%) collected in the damage zone of the Monte Marine Fault (Central Apennines, Italy). We perform experiments at effective normal stresses of 1 and 5 MPa, slip velocities of 0.001 m/s and 1 m/s, and a total displacement of 0.5 m in both dry and wet drained conditions (pore fluid pressure was 0.2 or 1.0 MPa). We examine the influence of pore fluid pressure using first water as pore fluid, to simulate wet conditions, and then Argon as pore fluid, to simulate dry conditions. For the first time, we measured pore fluid pressure during seismic slip thanks to a pressure transducer located on the downstream of the pore fluid pressure circuit. We also compare experimentally produced microstructures with natural samples. This comparison allows us to constrain the conditions at which fault slip occurred along the MMF. Mechanical data show that carbonate gouges pressurize, and samples undergo to significant shortening during experiments with water. Moreover, microstructural analyses suggest that fault slip along the MMF probably occurred in dry conditions during cyclic fault reactivations.

4.2 Introduction

The presence of fluids along active and seismogenic faults plays an important role in the nucleation and propagation of seismic ruptures (Rempe et al., 2014, 2017; Violay et al., 2014). The role of fluids in the seismic cycle has been investigated in many studies focused on the Umbria-Marche and L'Aquila seismic sequences, where earthquakes developed in carbonate platform rocks characterized by over-pressured fluids at depth (Chiodini and Cioni, 1989; Collettini and Barchi,

2002). Fluids influence earthquakes propagation; pore pressure changes during the seismic cycle due to the development of new pores and fractures suitable by fluids to flow. At the same time, the variation of pore pressure in space and time affects the effective stress distribution after the mainshock thus controlling the evolution of aftershocks sequences along the same and nearby fault zones. During seismic rupture propagation, at the micro-scale, it has been proposed that frictional heating should favour the reduction of the effective stress by enhancing pore fluid pressure (thermal pressurization, Rice, 2006).

The ingression of pressurized fluids in faults seems to play a pivotal role in the evolution of seismic sequences in the Central and Northern Apennines (e.g., Miller et al., Nature, 2003). Among these faults, the Monte Marine Fault (MMF), a NW-SE oriented Quaternary extensional fault located c. 20 km NW of the L'Aquila town, represents an area where the possible presence and influence of fluids during the seismic rupture (the fault was lastly reactivated during the 1703 earthquake) is still unclear. It is certain that the fault was shaped by a complex seismotectonic history resulting in the formation of large volumes of loose fault material formed by "shattering" cut by extremely localized cataclasites and ultra-cataclasites along major and subsidiary faults (Cortinovis et al., 2018). Nevertheless, the variety of the deformation processes and the conditions of fault rupture (i.e. pressure, temperature, depth of deformation, slip velocity and pore fluid pressure) need to be further investigated.

In the specific case of seismic slip propagation in carbonate rocks, the presence of water promotes the brittle failure of asperities thus enhancing fault weakening behaviour (Violay et al., 2014),which is at the base of rock failure and consists of a drop of rock friction coefficient. In case of calcite-rich fault gouges, Rempe et al. (2017) demonstrated that the mechanism of "dynamic weakening" with failure of asperities occurs faster in wet conditions than in dry conditions. However, existing technical limitations impeded to study water pressurized conditions at large seismic slip (i.e., > 0.1 m, 1 m/s). On the contrary, in dry conditions, dynamic weakening is slower and the formation of high-strain shear bands predates dynamic weakening (Fondriest et al., 2012; Rempe et al., 2017). Under dry conditions in calcite or dolomite gouges, there are also other mechanisms that induce faults' weakening: Han et al. (2010) proposed that the formation of nanograins can lubricate faults via powder lubrication. A general consensus developed around the importance of crystal plasticity in calcite or dolomite nanoparticles controlling dynamic weakening. Crystal plasticity involves the deformation of the material at the nanoscale due to strain variations able to induce modifications in the original crystallographic structure of a mineral. For example, De Paola et al., 2015 proposed

that nanograins could deform by grain size dependent diffusion creep (grain boundary sliding), and recently, Passelègue et al., 2018 confirmed that crystal plasticity is the main mechanism during earthquakes slip in carbonate rocks. Very recent experimental and microanalytical studies (Demurtas et al., 2019a; Pozzi et al., 2019) focused on the study of nanoparticles formation in mixtures of 50% calcite and 50% dolomite or pure calcite gouges and their deformation by combined dislocation creep, which consists of movements of dislocations through the crystal lattice of a mineral, and grain-size dependent diffusion creep, based on the diffusion of vacancies through the crystal lattice of a mineral.

Here we present a series of high velocity friction experiments performed with Slow to HIgh Velocity Apparatus SHIVA (HPHT lab, INGV, Roma) (Di Toro et al., 2010) on a natural fault gouge of mixed dolomite (80%) and calcite (20%) collected along a subsidiary fault in the damage zone of the MMF. We also compare naturally-produced microstructures from poorly cohesive fault samples collected from the MMF with experimentally-produced microstructures obtained by shearing loose fault gouge. This comparison allowed us to define the more probable conditions at which microstructures developed along the MMF during rupture at seismic and sub-seismic slip (depth of failure, pore fluid pressure and slip rate). In particular, we examined the influence of fluid using first water as pore fluid, to simulate wet conditions, and then Argon as pore fluid, to simulate dry conditions during slip. We performed experiments at effective normal stresses of 1 and 5 MPa (drained condition with pore fluid pressure of 0.2 and 1 MPa), at slip velocities of 0.001 m/s and 1 m/s, and a total displacement of 0.5 m.

We show that slip rate influences the mechanical behaviour of the natural fault gouge during experiments. In particular, at high slip rates and wet conditions, we observed fluid pressurization and evidences of dolomite/calcite decomposition with associated formation of nanoparticles and sintering of clasts. Our experimental findings allowed us to discuss the possible deformation mechanisms active along the Monte Marine Fault.

4.3 Methods

4.3.1 Geological setting and starting material

We manually sieved, with a 250 µm mesh, about 670 g of natural carbonate fault gouge from four different samples, of mixed dolomite and calcite, collected from the same fault plane along the seismogenic Monte Marine Fault (Central Apennines, Italy) and dried in oven at 40° C for 24 h to remove humidity. The material was collected along an extensional fault in the damage zone of the MMF, near the village of Pizzoli (Fig. 25). Along this fault, we could collect both cohesive and loose

material representative of an immature mosaic breccia. The heterogeneity of the material was useful to compare the natural microstructures with that obtained during friction experiments. We compared naturally produced microstructures on the cohesive sample with microstructures formed by friction experiments on the loose sample (Fig. 25). The four samples were analysed via X-ray powder diffraction, that revealed identical composition among the samples. Since samples were similar, we could mix them to obtain a homogeneous material (about 240 g) that was dried, sieved and then divided in identical sub-aliquots (10 g) using first a Quantachrome sieving riffler and then a Quantachrome sieving micro-riffler (University of Parma). After this operation, we obtained 24 comparable sub-samples. One of these sub-samples was further subdivided in smaller aliquots (each of about 1 g) suitable for laser granulometry analyses.

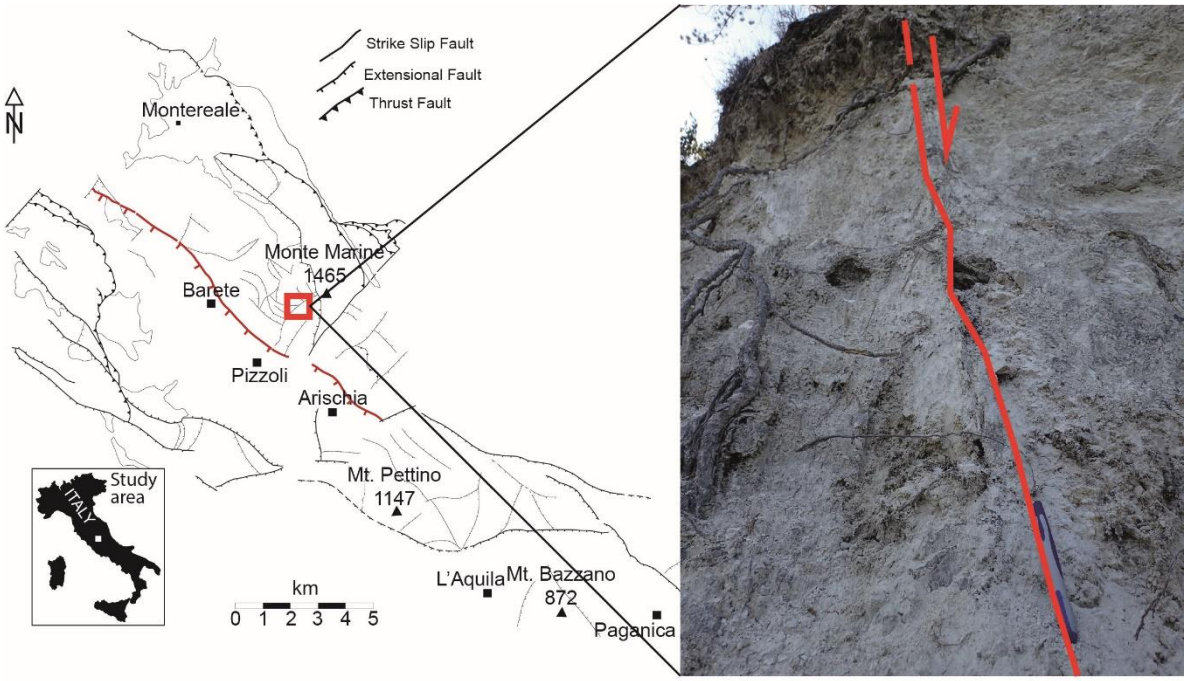

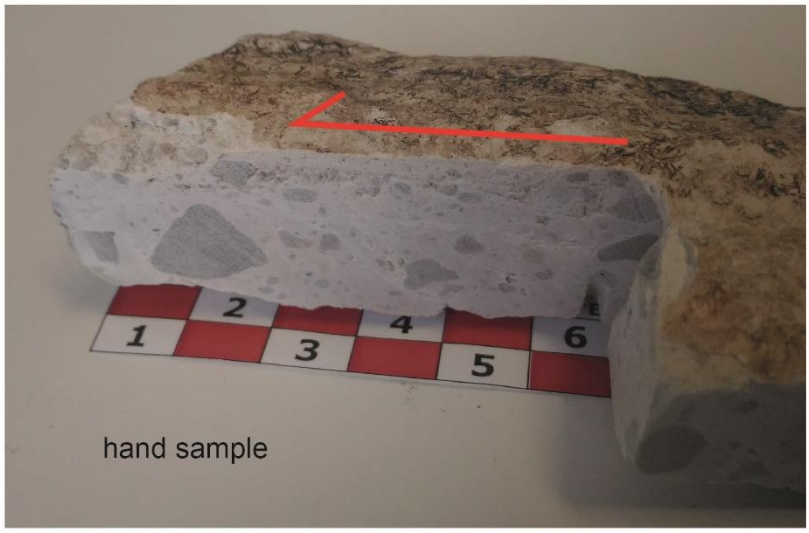

Figure 25: Structural map of the Monte Marine Fault with location of the study area. Loose and coherent samples collected from an extensional fault in the damage zone of the Pizzoli area. The coherent sample was analysed with image analyses while the loose sample was used in friction experiments.

4.3.2 Laser granulometry

Measurement of grain size distribution was performed via laser granulometry on the natural fault gouge with a laser diffraction particle size analyser (Malvern Mastersizer 3000) and associated dry dispersion unit (dry Aero S). Two samples respectively of 1.19 g and 1.21 g were investigated, the second sample to verify the reproducibility of our measurement. During the analyses, we set the air pressure (operative range: 0 - 4 bar) which determines the velocity at which the granular matter is lead into the system, at 1 bar, feed rate (operative range: 0% - 100%), which determines the time required for the material to pass through the analyser, at 20%, and measurement time at 60 s.

4.3.3 X-ray powder diffraction analyses

X-ray powder diffraction analyses were performed on the natural fault gouge using the Bruker D2 Phaser powder diffractometer (University of Parma). Measurements were performed using: Cu Kα radiation (30 kV excitation voltage and 10 mA current), a Ni filter, scanning angles 2θ between 4° and 70° (with incremental steps of 0.018°) and a sampling time of 1 s. The diffractometer acts with a θ-θ focalizing geometry and takes advantage of a solid-state detector (LYNXEYE XE-T). The diffraction patterns were identified using the Bruker software EVA and the Crystallography Open Database. The software performs a semi-quantitative analysis of the main mineralogical phases using the $I=I_{cor}$ ratio method. A sample rotation of 30 rpm was applied to minimize crystal preferential orientation effects on the powder scattered over the sample lid. During the analyses, we firstly set time at 0.5 s, 2θ between 4° and 10°, and PSD (Positive Sensitive Detector) opening at 2.5 s, to identify the presence of clay minerals. Then, we set time at 0.3 s, 2θ between 10° and 70°, and PSD opening at 5.8 s, to identify other mineralogical phases (i.e. Calcite and Dolomite).

4.3.4 High velocity friction experiments

4.3.4.1 The SHIVA Apparatus

SHIVA (Slow to High Velocity Apparatus, Di Toro et al., 2010; Niemeijer et al., 2012) is a high velocity friction experimental machine composed of a rotary column, a stationary loading system and a sample chamber in between. The apparatus is fixed to the ground to reduce vibrations during data acquisition. On the rotary side, the machine is equipped with two electric motors that impose the rotational motion to the sample. The small engine (Ultract III-U31320C.30.3MYZ000, “se” in Fig. 26a) works with velocities from 1 rpm to 4,000 rpm, has a nominal power output of 5.15 kW, and a

maximum torque of 20 N m. This can be increased up to 4,500 N m thanks to the presence of a gearbox (1:225) ("gb" in Fig. 26a) connecting the small engine to the shaft of the main rotary shaft. The large engine (Ultract III-U720.30.3M00000, "le". in Fig. 26a) works with velocities from 1 rpm to 3,000 rpm, has a nominal power output of 280 kW, and a maximum torque of 932 N m with kt = 1.65 and I = 565 A (at 1,800 RPM; 437 N m at 3,000 RPM). A sprag clutch ("sc" in Fig. 26a) connects the large engine to the rotary shaft without losses of motion and torque during the rotary transition from one engine to the other. The presence of two 1,500 N m BC3 Bellow couplings and ball-bearing housings ("bc" in Fig. 26a) between the sprag clutch and the small engine column helps to dampen the vibrations and the movements of the rotary column.

On the stationary side, the apparatus is equipped with an electromechanical cylinder (EMC-105-HD produced by Bosch-Rexroth, Fig. 26a) to apply the normal load. The electromechanical cylinder is composed of an electric servo motor ("sm" in Fig. 26a) connected to a screw drive ("d" in Fig. 26a) via a timing belt. The electric motor has a maximum rotation speed of 3850 rpm and a peak torque of 85.86 N m (with kt = 2.12 and I = 40.5 A). This results in a maximum possible normal load of 76 kN. During ordinary operation conditions the maximum normal load applicable is 17.5 kN.

The normal load is measured via a loadpin (Batarow) placed in series between the end of the screw drive and the stationary transmission shaft of SHIVA ("lp" in Fig. 26a). The maximum measurable force of the loadpin is 80 kN and the resolution is ± 0.4 kN. The normal load is controlled in a PID closed loop. The combination of the maximum axial velocity (0.64 m/s) and acceleration (30 m/s^2) of the load system and the controller velocity loop time (500 µs) results in a time resolution of 10 ms for the normal load control.

In the stationary side, torque is measured via a S-shaped load cell which connects a horizontal arm to a vertical bar fixed to SHIVA concrete base ("tlc" in Fig 26a). The number of rotations is measured in the rotary side using two optical encoders. The axial displacement of the stationary column is measured with linear variable displacement transducers (LVDTs). In the sample chamber, we installed a LVDT ("l" in Fig. 26a) to measure axial shortening on the sample during the experiments. A DC-LVDT ("dcl" in Fig. 26a) is placed between the sample chamber and the piston assemblage on the stationary side.

During the experiments we used a cylindrical sample holder with a radius of 25.5 mm (see next section for a comprehensive description). The encoders measurements are converted into tangential slip according to the following equation:

$$D[m] = D[revs] \cdot \frac{4\pi r}{3}$$

The slip D[m] is calculated from the cumulative number of revolutions D[revs] and the sample radius r. The velocity is calculated by filtering the slip data and calculating its time derivative using the time step of the data acquisition. Both slip and velocity are referred to an "equivalent radius" (i.e. 2/3 of the external radius of the sample) and are therefore defined as equivalent velocity and displacement. Normal stress σ_n and shear stress τ are calculated according to Mizoguchi et al., 2007:

$$\tau[MPa] = M[V]\, C_M\, \frac{3}{2\pi r^3}$$

$$\sigma_n[MPa] = F[V]\, C_F\, \frac{1}{\pi r^2}$$

With M[V] the measured torque with the S-shaped loadcell, F[V] the measured force with the loadpin, r the sample radius, and C_M and C_F the corresponding calibration constants.

The LVDT and DC-LVDT measurements are converted into displacement multiplicating them with the corresponding calibration constants.

4.3.4.2 Description of the pressurized gouge sample assemblage and pore fluid circuits

The sample holder is composed of two cylinders ("ssh" and "rsh" in Fig. 26b) specifically designed for pore fluid to flow through and saturate the gouge layer, which is sandwiched in between. The base of the cylinders adjacent to the gouge layer has three porous plates (sintered stainless steel) each one inserted in a socket. Below the plates, at the base of each socket there are channels which distribute the fluid coming from the holes in the cylinders, therefore communicating with the pore fluid circuit (see Fig. 26b). Porous plates and socket channels help to distribute uniformly the pore fluid on the gouge surface thanks to the presence on the porous plates of radial rugosity driving fluids to move into the material. The cylinders are fixed at the two sides of the SHIVA sample holder via radial springs. The stationary cylinder has three additional holes with direct access to the gouge layer (independent of the previously described holes): one is used to insert a miniaturized pressure transducer (placed under one of the three porous plates, ca. 1.7 mm distance from the base of the cylinder), and another one is used to insert a K-type thermocouple, which hot junction tip is placed at the base of the cylinder, used for measuring pressure and temperature, respectively (Fig. 26c).

The sample assemblage is composed by two independent circuits: a confining pressure circuit and a pore pressure circuit (Fig. 26b). The confining pressure circuit is composed of a Teledyne Isco Pump 500D syringe pump ("Pump A" in Fig. 26b), a water reservoir and a circuit connecting the pump to the pressure vessel ("pv" in Fig. 26b). The pore fluid circuit is composed of a second identical syringe pump ("Pump B" in Fig. 26b) connected to a water reservoir (in experiments with water as pore fluid) or a gas canister (in experiments with Argon as pore fluid), and to a circuit connecting the

pump to the sample holder (i.e., to the back of “shs” in Fig. 26b). Both syringe pumps have a capacity of 507 mL, a flow range from 0.001 to 204 mL/min (accuracy 50% of the setpoint), a displacement resolution of 31.2 nL, and a pressure range from 0.07 to 25.86 MPa (accuracy 0.5% full scale).

During the experiments, we measured the confinement pressure with a pressure transducer on the pressure vessel (“Pc” in Fig. 26b) and the downstream pore pressure with a pressure transducer on the downstream pore fluid pressure circuit (“Pf,d” in Fig. 26b).

All pressure measurements are converted into pressure via the respective calibration factors. Temperature measurement is converted into temperature using the 9^{th} order inverse polynomial function (https://srdata.nist.gov/its90/download/type_k.tab).

4.3.4.3 Preparation of the experiment

The gouge layer was prepared by pouring ca. 10 gr of starting material on the porous plates over the stationary cylinder, which was previously jacketed with a heat shrink tube. This assemblage was then inserted in the pressure vessel past the O-rings so that the gouge layer stayed between the stationary and rotary O-rings (Fig. 26b). The interface between the rotary cylinder and the heat shrink tube (fixed to the stationary cylinder) was lubrified applying a coating of molybdenite solid lubricant. The rotary sample holder was then inserted into the heat shrink tube. The full assemblage was finally loaded in the sample chamber of SHIVA.

4.3.4.4 Description of the experiment

Once the sample was positioned in the sample chamber, we loaded it up to the set-point normal stress (1.2 or 6 MPa) and confinement pressure (0.4 or 2 MPa).

In case de-ionized water was pore fluid, upstream pore pressure was set at 0.1 MPa (“Pf,u” in Fig. 26b), waiting until pore pressure downstream (“Pf,d” in Fig. 26b) equals the upstream. We used a small electric pump connected to the downstream pipe for several minutes to remove air bubbles from the pore fluid circuit.

In case Argon was the pore fluid, gas was flowed across the gouge layer for several minutes at a constant pressure of 0.1 MPa to ensure saturation.

After this, while keeping the upstream pressure constant (0.1 MPa), the end cap of the downstream pore fluid circuit was kept closed for several minutes and then opened to further remove air bubbles. After this operation was repeated several times, we applied the set point upstream pore fluid pressure (0.2 or 1 MPa) and waited until downstream pressure transducer read an identical pressure value.

The experiments were performed under drained conditions. An initial slip pulse named “preshear” was applied to the gouge layer to warrant a standard initial microstructure and gouge layer thickness. Equivalent velocity was set to 7 µm/s for a total displacement of 0.007 m. A second slip pulse named “main pulse” was applied to the gouge layer: equivalent velocity was set to 0.001 or 1 m/s for a total displacement of 0.5 m in both cases.

The main pulse was repeated (i.e., “second pulse”) for the experiments s1773, s1774 (V=1 m/s and water as pore fluid) and s1775 (V= 1 m/s and Argon as pore fluid). We applied the “second pulse” by repeating the same procedure of the “main pulse” on the deformed sample and keeping the operative conditions of pore pressure, normal stress and confinement unvaried during the second pulse.

At the end of the experiment, we decreased the pore fluid pressure to 0.1 MPa, then switched off the pressure control and opened the pore fluid circuit to the atmosphere. Normal stress was decreased down to 0.5 MPa while confinement pressure was decreased to 0.1 MPa prior to switch off both control systems. In the end, the sample holder assemblage was removed from the sample chamber to retrieve the gouge layers for microstructural studies.

	Pore fluid	1 MPa	5 MPa
1 mm/s	Ar	1702 (1701, 1700)	1705
	H_2O	1696	1698
1 m/s	Ar	1703, 1775	1706, (1776)
	H_2O	1697, 1773	1699, 1774

Table 2: List of slow (v=0.001 m/s) and fast (v=1 m/s) friction experiments performed at low (σ_{neff}=1 MPa) and high (σ_{neff}=5 MPa) normal stress and different pore fluid (water vs Argon). Experiments in parentheses are failed experiments.

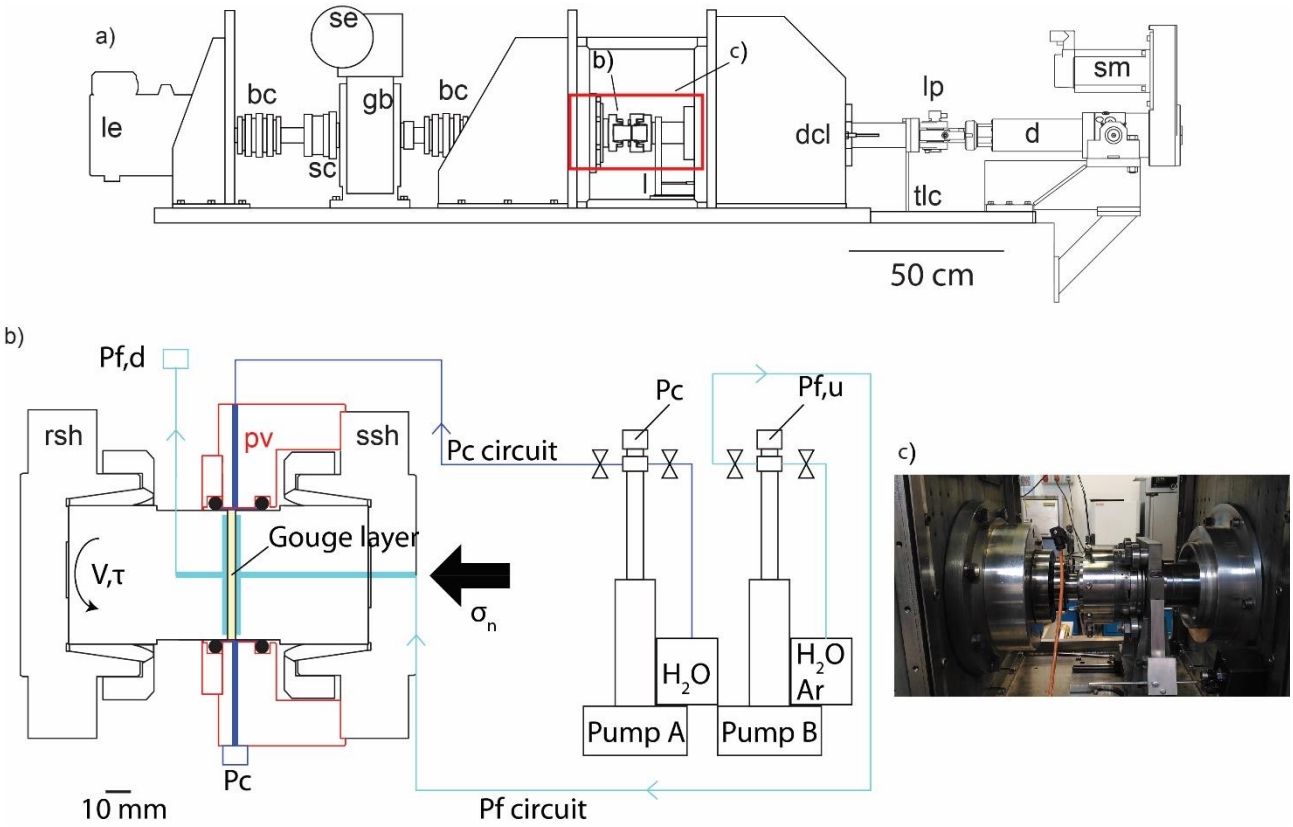

Figure 26: Schematic diagram of the slow to high velocity apparatus (SHIVA) (a), with detail of the new pressurize gouge sample assemblage and pore fluid circuits for the control of confinement pressure (Pump A) and pore fluid pressure (Pump B) (b). Detail of the pressurized gouge sample assemblage arranged into the sample chamber (c).

4.3.5 Microstructures

After the experiments, the gouge layers were recovered by opening the sample holder, by decoupling the rotary cylinder from the remaining assemblage. The gouge layers were dried under room humidity conditions for an overnight. Subsequently, they were embedded into Struers Epofix epoxy resin and cured under room humidity and temperature. The samples were cut on an orthogonal direction to the sample radius at ca. 2/3 of the radius. Standard petrographic thin sections were prepared (University of Parma), polished (~30-35 µm thick) and then carbon coated (INGV, Rome, Italy) for SEM analyses.

4.3.5.1 SEM

A JEOL JSM-6500F Field emission Gun - Scanning Electron Microscope (INGV, Rome, Italy) was used to analyse microstructures formed in the natural fault gouge during friction experiments. We acquired Back Scattered Electron (BSE) and Secondary Electron (SE) images with an accelerating voltage of 15 KV at a working distance of 10 mm.

4.3.5.2 EMPA

A JEOL JXA 8200 Electron Micro-Analyzer (EPMA) with combined EDS-WDS (five spectrometers with twelve crystals) (INGV, Rome, Italy) was used to obtained good compositional maps from the samples recovered after friction experiments (Table 3). To analyse our samples, we used the following standard: mineral1 (Ca), mineral2 (Mg), mineral3 (S), mineral4 (Fe) and mineral5 (Si). During analyses, we set the acceleration voltage at 15 kV and the beam current at 7,5 nA. The beam size was kept at 2,5 µm, with the counting time at 10 s on the beam and at 5 s on the background. During X-ray map acquisition, we used 15 kV accelerating voltage, 7,5 nA probe current, and dwell time of 60 ms per pixel.

name	x (µm)	y (µm)	pixel size (µm)
1699_1	1000	1500	2
1699_2	1000	1500	2
1699_3	200	400	0.5
1706_1	400	700	1
1706_2	200	200	0.5
1706_3	400	700	1

Table 3: List of areas analyzed with EMPA compositional maps, with areas and locations on the samples.

4.4 Results

4.4.1 Materials: XRD and laser granulometry

With XRD and laser granulometry (LG) analyses, we characterized the material before performing friction experiments. XRD analyses revealed that the sample consists of a mixture of calcite (20%) and dolomite (80%). The grain size distribution of the sample, obtained with dry laser granulometry, is represented in Fig. 27a as frequency distribution of equivalent spherical particles. The shape of the granulometric curve is concave-upward with peak value at ~200 µm and shows a

significant asymmetry that suggests a heterogeneous composition of the sample, with many clasts of diameter <200 µm. The related value of fractal dimension, inferred by plotting the cumulative number of particles versus size classes, is D=2.15, with an R2 coefficient of 0.99 (Fig. 27b). This value of the fractal dimension is typical of mature cataclasites or a comminute breccias (Billi and Storti, 2004).

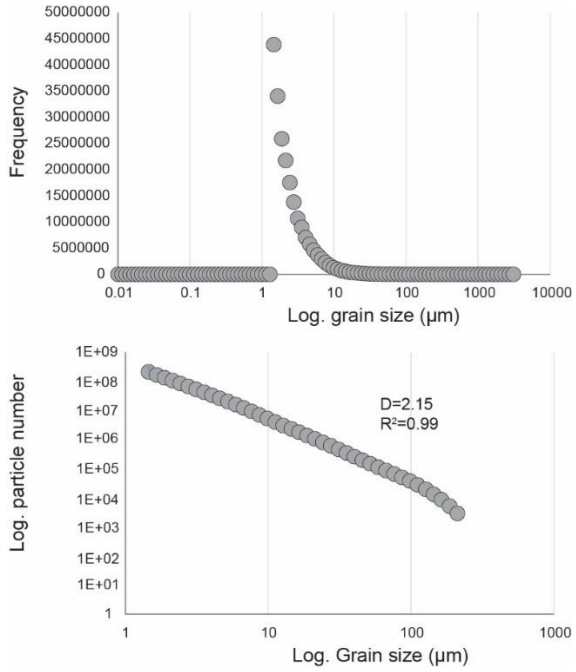

Figure 27: Characterization of the starting materials. Frequency and log. cumulative distribution of particles plotted versus log. particle size obtained with the laser granulometer Mastersizer 3000.

4.4.2 Experiments

We represent the results of our experiments as values plotted over time. The variability of the different parameters are represented as curves of different colour: the light green curve represents the shear strength, the yellow curve the normal stress, the light blue curve is the confinement pressure, while the blue curve represents the amount of slip. The green curve indicates the behaviour of the pore fluid while the red curve the sample shortening. Finally, the black curve represents the values of velocity. The rise of the red curve that occurs at increasing slip (blue curve) indicates shortening and is usually associated to a decrease in shear stress and a related increase in the pore fluid pressure. A drop of the red curve can also occur. This is indicative of sample dilation and is usually accompanied by the decrease of the pore fluid (green curve). Dilation can occur while shear stress is increasing.

4.4.2.1 Preshear

The preshear was performed at a slip rate of 7 μm/s for total 0.007 mm of slip (lasting ca. 1200 s). In most experiments, shear strength increases with time and slip ("slip-strengthening" behavior) until reaching a residual strength defined as τ0. A possible exception is the experiment at 1 MPa with Argon pore fluid (s1702), displaying a peak strength at ca. 0.85 MPa followed by a slip-weakening behavior down to a residual strength of ca. 0.8 MPa (Fig. 28c). In most experiments, the value of the pore pressure remained stable (drained conditions) at the value controlled from the upstream side and shortening (compaction of the gouge) increased (red curves in Fig. 28). During the experiment s1775, the pore pressure was not stable due to difficulties in compensating the pore pressure (Fig. 28d). Overall, total shortening for the same slip amount was systematically higher in presence of pressurized water (left column in Fig. 28) than in presence of Argon (right column in Fig. 28), increasing from a minimum of about 0.2 mm with Argon to a maximum of 0.4 mm in water. Normal stress was kept constant from the servo-controlled electromagnetic piston for the entire duration of the experiments, as well as the confinement and pore pressures which were compensated by the syringe pumps (excluding experiment s1775 in Fig. 28d).

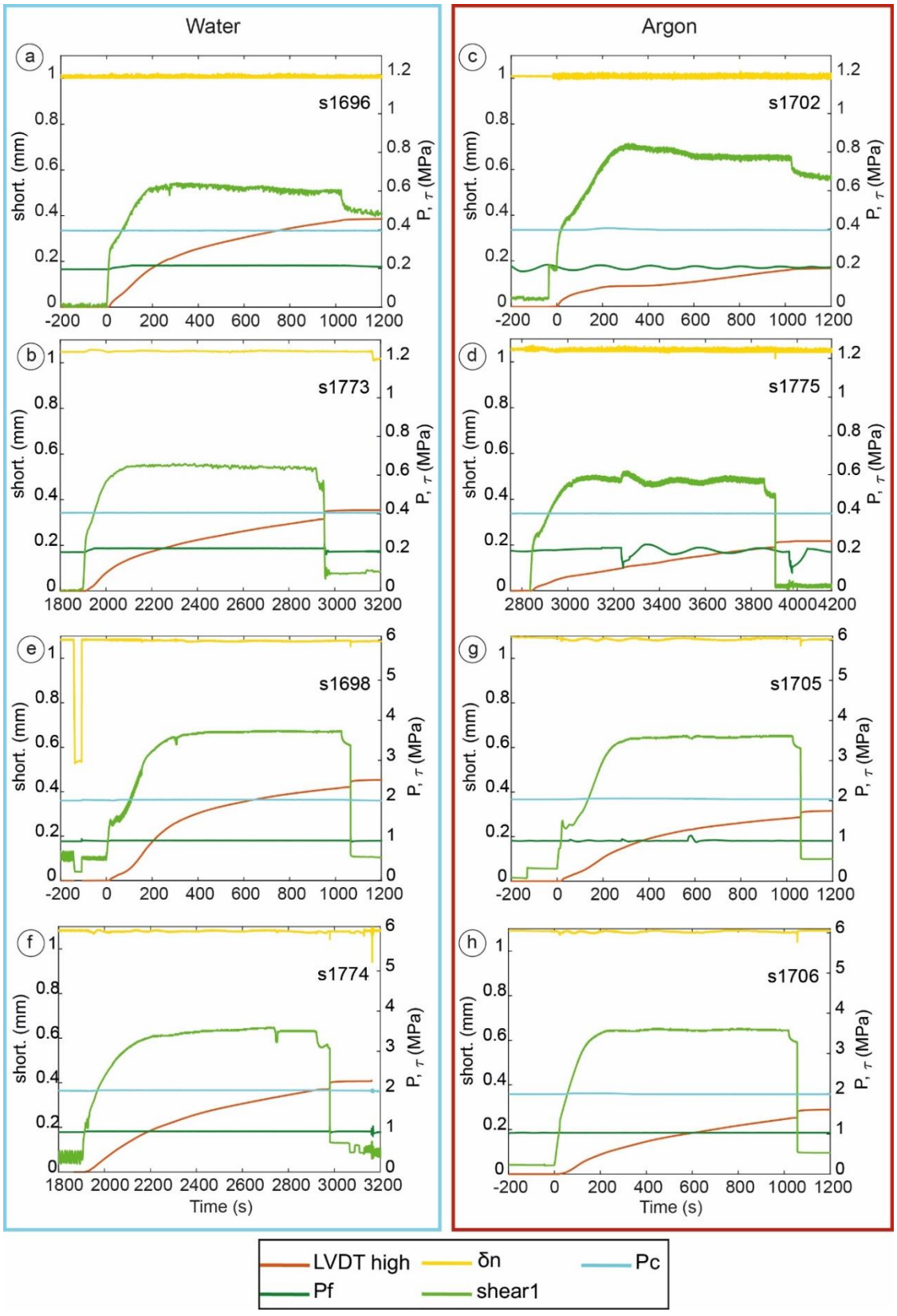

Figure 28: Mechanical data for preshear at 7 µm/s. Evolution with time of Axial displacement (LVDT high). Positive trend denotes compaction, negative trends denotes dilation. Confinement pressure (Pc), pore fluid pressure (Pf), shear strength (shear1) and normal load (σn).

4.4.2.2 Experiments at 0.001 m/s with water and Argon

Water. During the experiments s1696 and s1698 at V=0.001 m/s with water as pore fluid, shear strength generally increased with time and slip (Fig. 29a, b). In particular, at low normal stress of σ_n = 1.2 MPa (s1696), about 0.6 mm of shortening occurred in 600 s and shear strength increased continuously with time (Fig. 29a). In the case of high normal stress with σ_n = 6 MPa (s1698), shortening was lower and the sample thickness decreased of 0.35 mm in 600s and shear strength increased with time after a decreasing stage at slip initiation (Fig. 29b).

Argon. During the experiments s1702 and s1705 at v=0.001 m/s with Argon as pore fluid, shear strength was generally constant or slightly decreased with time and slip (Fig. 29c, d). At low normal stress with σ_n=1.2 MPa (s1702), the sample thickness decreases of 0.4 mm in 650s, while in the case of high normal stress with σ_n=6 MPa (s1705), shortening was lower and sample thickness decreased of 0.3 mm in 600s (Fig. 29c).

At both low and high normal stress and with both water and Ar, pore pressure and confinement remained constant suggesting absence of pressurization or the effectiveness of the pore fluid circuits (efficient drained conditions) in compensating the mechanical pressurization associated to gouge compaction. The decrease in pore pressure during experiment s1696 (Fig. 29a) at the beginning of the experiment could arise from spurious misalignment of the sample holder.

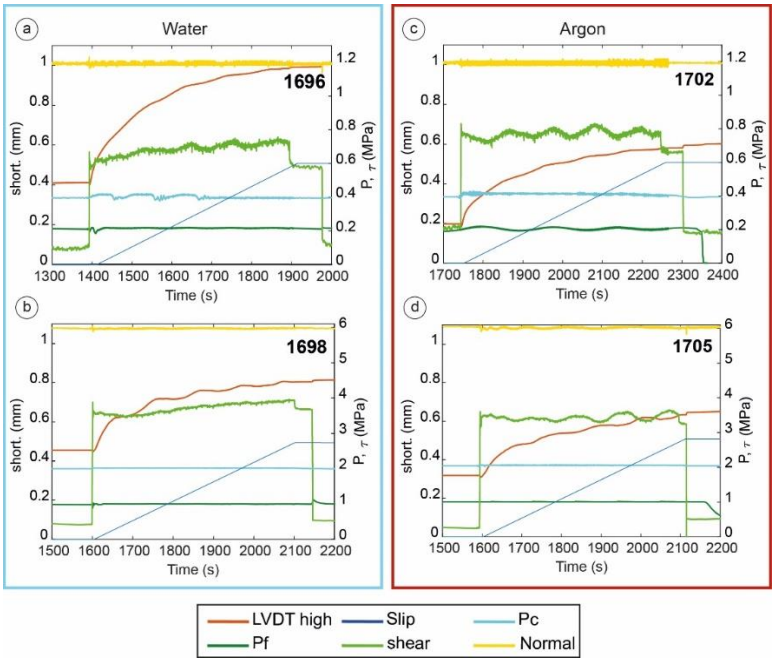

Figure 29: Mechanical data for slow experiments at 0.001 m/s, with water/Argon as pore fluid and total normal load of 1.2 MPa and 6 MPa. Evolution with time of Axial displacement (LVDT high). Positive trend denotes compaction, negative trends denotes dilation. Confinement pressure (Pc), pore fluid pressure (Pf), shear strength (shear) and normal load (σn).

4.4.2.3 Experiments at 1 m/s with water and Argon (main pulse)

Water. During these experiments, the samples achieved a peak strength at slip initiation after which the frictional strength decayed rapidly with time and slip (slip-weakening behavior) to increase again at the end of the experiment (strength recovery), independently of the imposed normal stress (Fig. 30a, b). In the experiment with σ_n=1.2 MPa (1773), significant shortening occurred, and sample thickness decreased of 0.5 mm in ca. 1 s (Fig. 30a). The confinement pressure increased rapidly from 0.35 MPa to 0.5 MPa during and slightly after the slip pulse and decreased slowly down to 0.4 MPa (after the slip pulse finished). A similar trend is that of the pore fluid pressure, which increased from 0.2 MPa to 0.4 MPa during the slip pulse and then slowly decreased to 0.3 MPa (after the slip pulse finished). A close look to the evolution of pore pressure with time allows us to recognize a pressure drop and shortening decrease (gouge dilation) during the initial acceleration stage, anticipating the pressure increase, lasting less than 100 ms (Fig. 30a). In the meantime, shear strength reaches a peak during the acceleration stage (τ_p), decreases to a constant value when V is 1 m/s (τ_{ss}) and then increases during the deceleration stage (τ_r). After the slip pulse, severe oscillations in normal force due to an instability of the control system occurred and therefore are not discussed. In the experiment with σ_n=6 MPa (1774), shortening increased from 0.4 mm to 0.85 mm during the slip pulse while pore pressure raised from 1 to 2.1 MPa (Fig. 30b). This occurred simultaneously with a change in the confinement pressure, which increased from 2 to 2.5 MPa. Shear strength evolved as in experiment 1773: peak strength at the onset of slip was followed by a decrease of the shear strength (while pore pressure increased) and then recovered at the end of slip (while pore pressure decreased). A small decrease in normal stress, pore pressure and shortening is observable during the peak strength (Fig. 30b).

Argon. During these experiments, the samples showed either an almost constant shear strength or a maximum in strength decreasing with time and then recovering at the end of the slip (Fig. 30c, d). This shear strength evolution varied depending on normal stresses. At low normal stress with σ_n=1.2 MPa (1775), the sample had a phase of strengthening that lasted for less than 1 s and coincided with a small loss of normal stress, slight increase in confinement pressure and significant shortening (Fig. 30c). In particular, the sample thickness decreased of 0.4 mm in less than 1 s, during which the confinement pressure increased (Fig. 30c). On the contrary, the constant trend of pore pressure indicates the absence of pressurization. However, this experiment could possibly have failed due to the strange behavior registered for shear strength (Fig. 30c).

At high normal stress with σ_n=6 MPa (1706), we observe weakening behaviour (Fig. 30d). Fault weakening is associated to a slight increase in confinement pressure and significant shortening that results in a total decrease of gouge thickness of 0.5 mm. Pore and confinement pressures slightly increased during the slip pulse, while normal stress decreased at slip initiation (Fig. 30d).

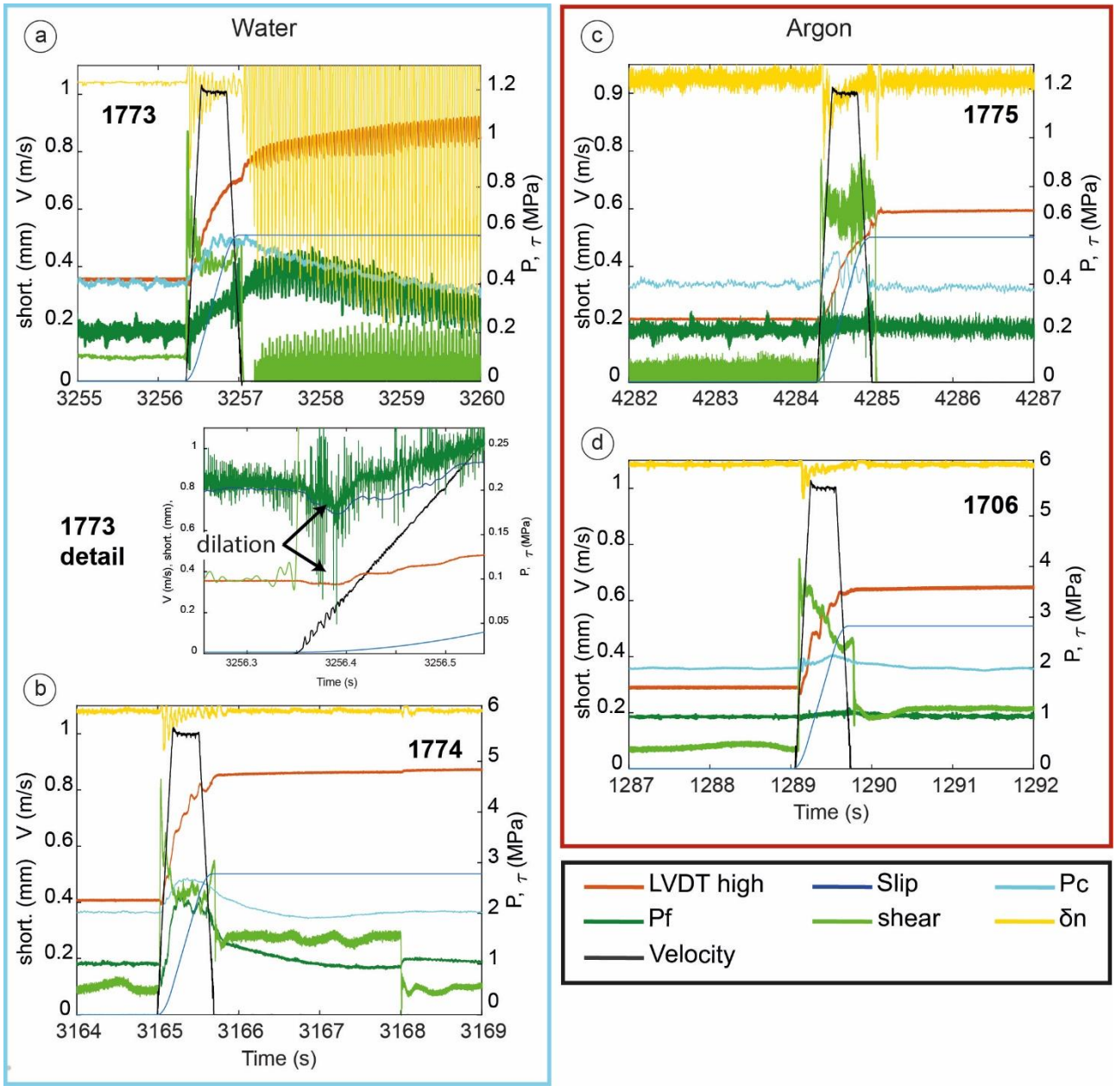

Figure 30: Mechanical data for fast experiments at 1 m/s (main pulse), with water/Argon as pore fluid and total normal load of 1.2 MPa and 6 MPa. Evolution with time of axial displacement (LVDT high). Positive trend denotes compaction, negative trends denotes dilation. Confinement pressure (Pc), pore fluid pressure (Pf), shear strength (shear) and normal load (σn).

4.4.3 Microstructures

4.4.3.1 Results from SEM and EMPA analyses

With SEM and EMPA analyses, we studied microstructures originated during friction experiments under wet and dry conditions, to understand the role of fluids during fault deformation and the possible effect of temperature increase, especially during dry experiments. SEM analyses show that microstructures produced under wet conditions (water as pore fluid) in the experiments with slow and high velocities (of 1 m/s and 0.001 m/s), normal stress of 6 MPa and displacement of 0.5 m are different with respect to that produced in dry conditions (Argon as pore fluid).

The samples recovered from the experiments s1699 (H_2O at V = 1 m/s) and s1706 (Ar at 1 m/s) have the same mineralogical composition but different features (Fig. 31, 32, 33); in both cases, dolomite and calcite crystals cover most of the volume of the sample thus testifying the absence of new phases or minerals originated during the experiments. In the thin section of the experimental fault produced under wet conditions at v=1 m/s (s1699), we qualitative estimated <10% of visible calcite crystals (Fig. 31), which is less than the value (~20%) estimated with the XRD analysis on the original fault gouge. On the contrary, the sample produced at the same velocity in Ar (s1706) has much more calcite distributed between dolomite clasts and shows peculiar microstructures (Figs. 34 and 35). In the same experiment (s1706) the slip plane consists of a mirror-like slip surface characterized by sintering and calcium accumulation that do not occur in presence of water (s1699).

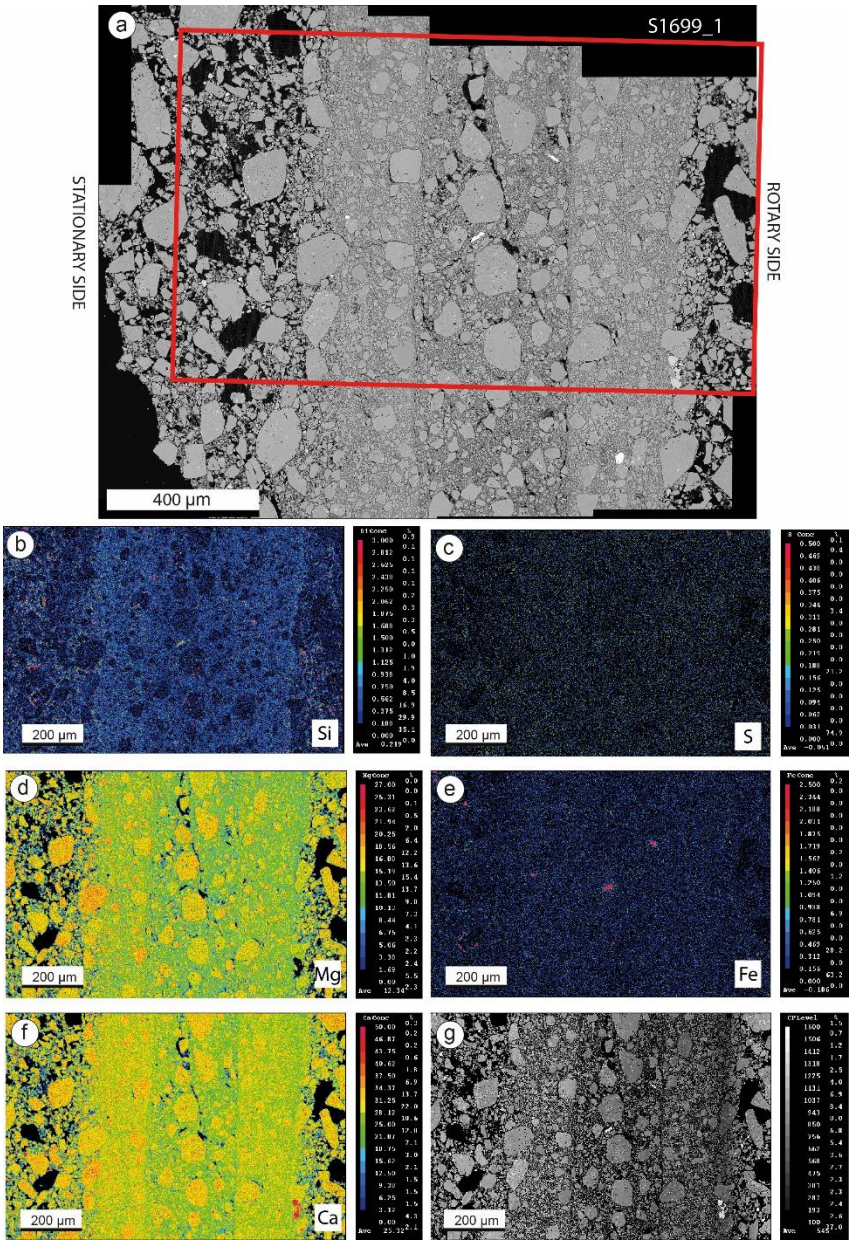

Figure 31: a) Photomosaic from scanning electron microscope (SEM) images showing sample deformed with fast experiment (v=1 m/s) with water as pore fluid (s1699, see Table 2). From b to g) Compositional maps from EMPA with abundance and distribution of major elements: Si, S, Mg, Fe, Ca.

Water, 1 m/s (s1699). In experiments with water, sample developed two symmetrical localized (~300 µm thick) shear bands with very low porosity, that embed a thicker stratum (~400 µm thick) with higher porosity (Fig. 31a). All together they show a lower porosity and lower average grain size than the surrounding volumes of gouge. These localized shear bands are characterized by the presence of very comminute material and µm- to cm- size clasts of prevalent dolomite and minor calcite (Figs. 31a, d, f). These bands change in thickness along the thin section (from a minimum of 200 µm to a maximum of 400 µm) and contain µm- to mm- size clasts. They are distinguishable on the base of their mineralogical composition (Figs. 31b-g) and present a different amount of

magnesium (Fig. 31d), which is abundant in the central band, and calcium (Fig. 31f), which is concentrated at the boundaries of the localized zone. The percentages of silicon, sulphur and iron in the thin section are negligible, even if silicon is clearly preferentially distributed in the central part of the thin section, where maximum localization occurs (Fig. 31b).

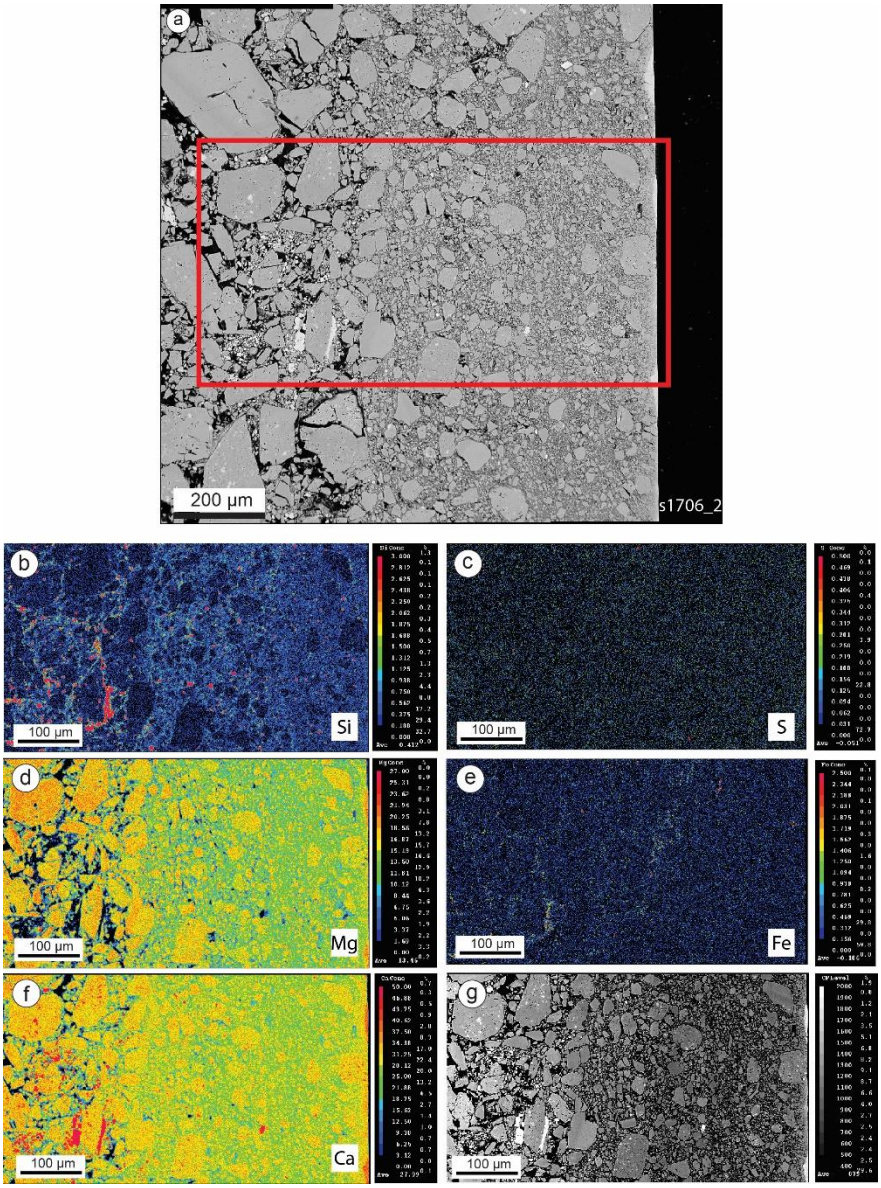

Figure32: a) Photomosaic from scanning electron microscope (SEM) images showing sample deformed with fast experiment (v=1 m/s) with Argon as pore fluid (s1706_2, see Table 2). From b to g) Compositional maps from EMPA with abundance and distribution of major elements: Si, S, Mg, Fe, Ca.

Argon, 1 m/s (s1706). In experiments with Argon, localization occurs along one single (~250 µm thick) band (Fig. 32). This band is characterized by a significant porosity reduction with respect to the boundary regions and is formed by µm- to mm- size grains of prevalent dolomite and minor calcite (Fig. 32a). Sample composition has been investigated in two different areas of the same

sample (s1706_2 in Fig. 32 and s1706_1 in Fig. 33). In these areas, the amounts of silicon, sulfur and iron are negligible (Figs. 32, 33). Silicon is concentrated in the pores of the boundary region and scattered around the localized band (Fig. 33b). Magnesium is one of the major components (Fig. 33c) together with calcium that is concentrated in the pores of the boundary region (Fig. 33d) and locally is accumulated along the slip surface (Fig. 33d and Fig. 34f, g). The slipping zone contains nanoparticles that consist of nm-size rounded clasts (Fig. 34). Nanoparticles in s1706 have rounded shapes and develop from the boundaries of the big (some µm thick) corroded clasts of dolomite (Fig. 34c) and in proximity of the slip surface (Figs. 34d, e). Decomposition and sintering occur near calcite along the slip surface (Figs. 34f, g).

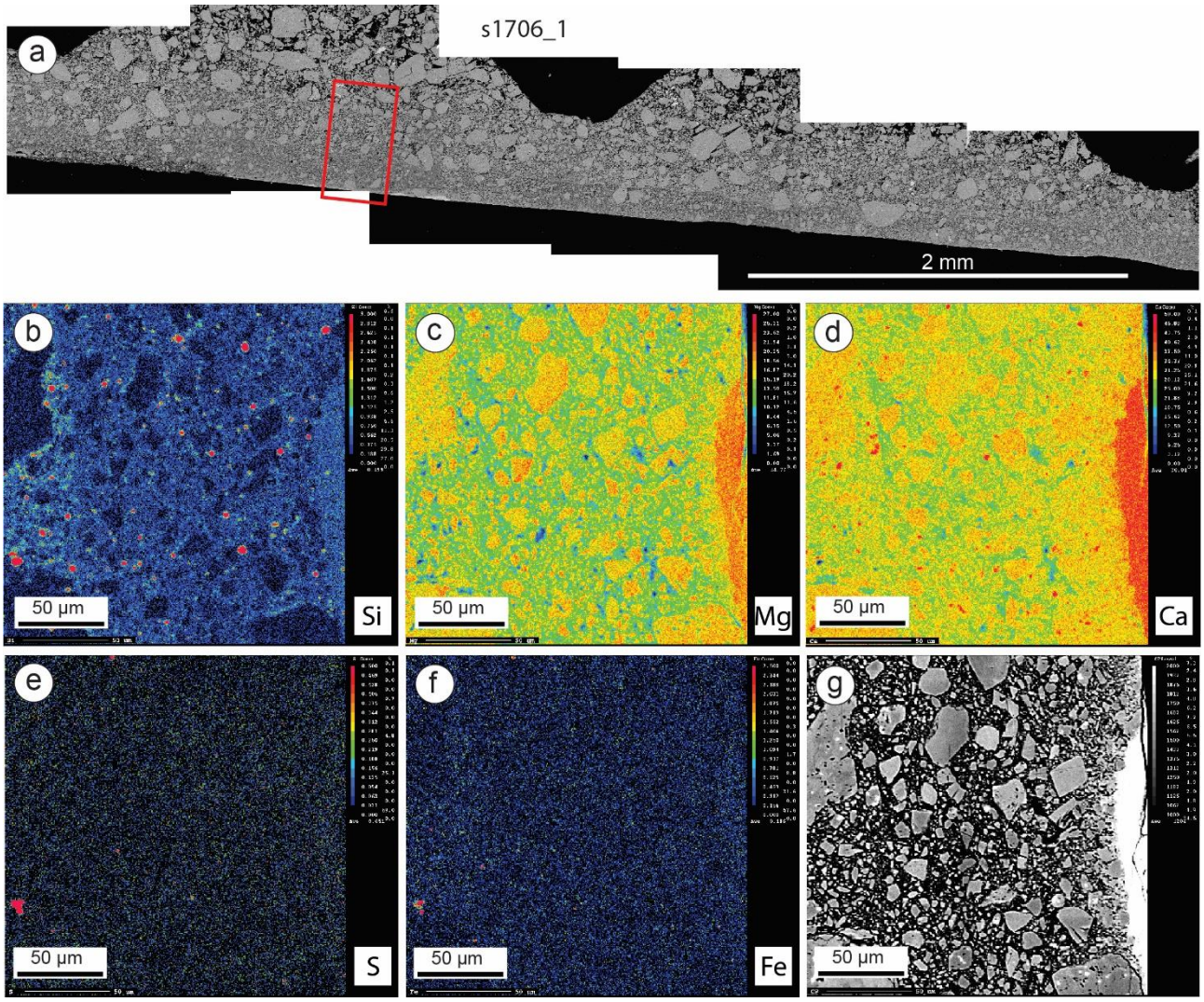

Figure 33: a) Photomosaic from scanning electron microscope (SEM) images showing sample deformed with fast experiment (v=1 m/s) with Argon as pore fluid (s1706_1, see Table 2). From b to g) Compositional maps from EMPA with abundance and distribution of major elements: Si, S, Mg, Fe, Ca.

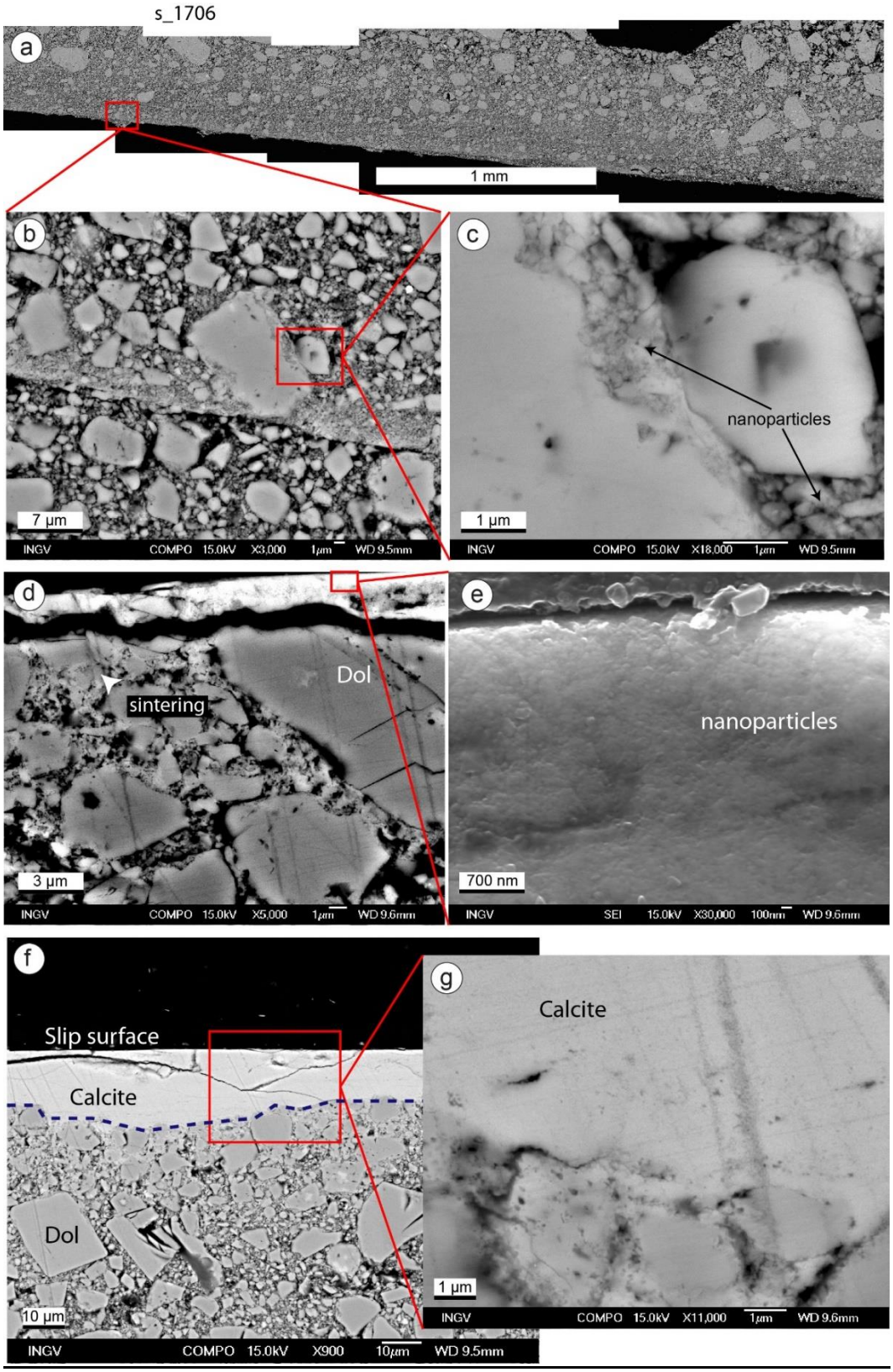

Figure 34: Scanning electron microscope (SEM) images of a) slip surface originated during fast experiment (v=1 m/s) with Argon as pore fluid (s 1706, see Table 2). b, c) Detail on corroded dolomite clasts surrounded by nanoparticles. d, e) Detail on nanoparticles near the slip surface. f, g) Detail on calcite crystals along the slip surface.

Water, 0.001 m/s (s1698). The thin section obtained at slow velocity (v=0.001 m/s) in water with normal stress of 6 MPa and displacement of 0.5 m (s1698) shows two bands of localization that are distinguishable with difficult from the stratum embedded in between (Fig. 35a). These three layers present a similar degree of comminution and differ significantly from the boundary regions for clasts shape and porosity amount: the boundary band is characterized by thicker angular clasts and increased porosity. Fig. 35c shows an imbricate clast with dextral transport surrounded by more comminute angular clasts that constitute the sample matrix (Fig. 35d). Even in the right part of the gouge layer in Fig. 35a, the matrix is formed by angular sub-micrometric nanoparticles (Fig. 35b).

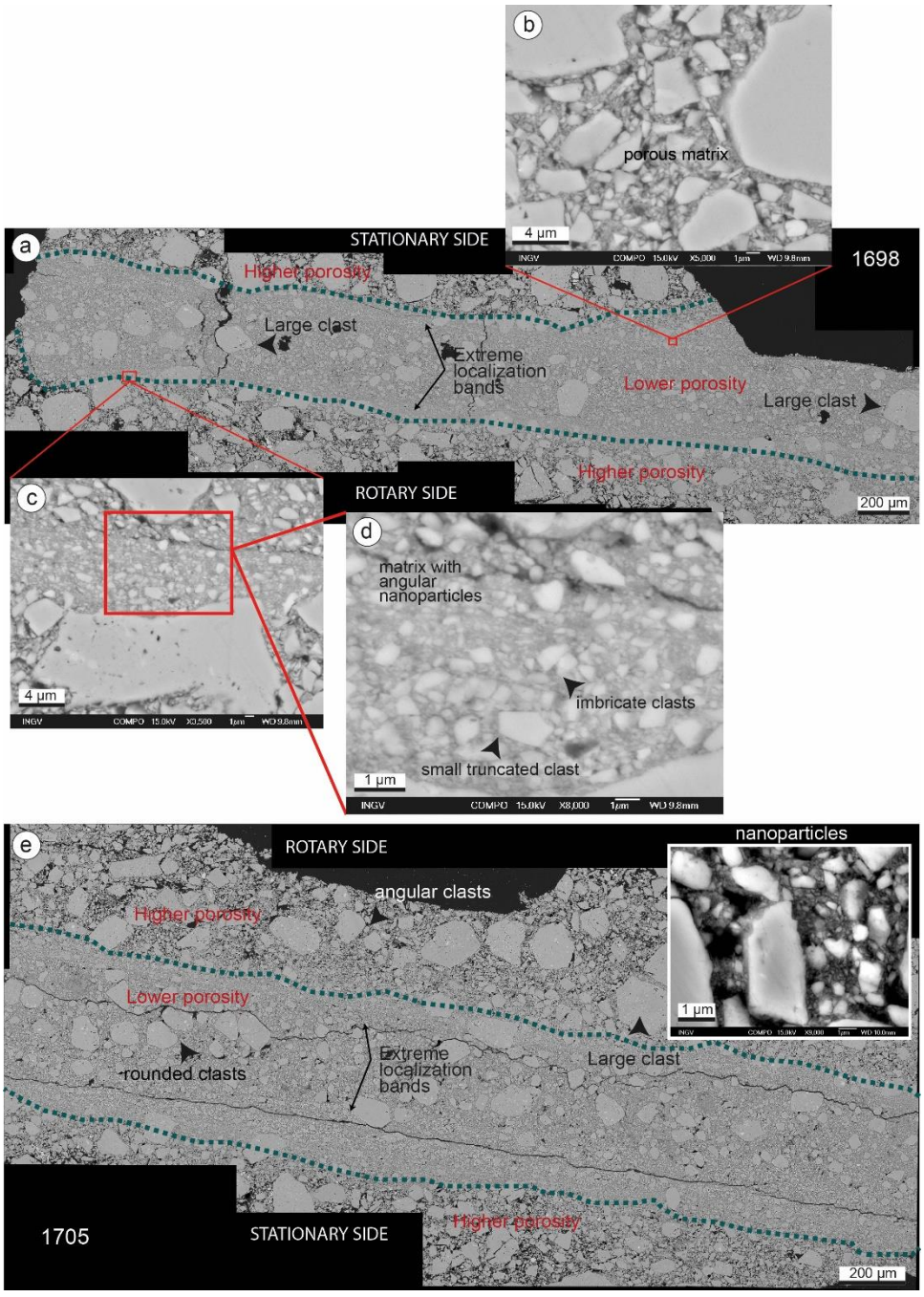

Figure 35: a) Photomosaic from scanning electron microscope (SEM) images showing sample deformed with experiments at v=0.001 m/s, σ_{neff} =5 MPa and water as pore fluid (s1698). b) detail on the porous matrix. c) detail on imbricate clast surrounded by the fine matrix of Fig. 12d. e) Photomosaic from scanning electron microscope (SEM) images showing sample deformed with experiments at v=0.001 m/s, σ_{neff} =5 MPa and Argon as pore fluid (s1705). In the small box on the right: detail on nanoparticles formed at these conditions.

Argon, 0.001 m/s (s1705). Microstructures formed at slow velocities in Argon (Fig. 35e) consist of a double band of extreme localization sandwiching a less localized low porosity band. The two bands of localization are both delimitated, towards the inner part of the thin section, by two thin fractures running parallel to the shear direction. In these bands, clasts are more comminute and

rounded than in the external part, where porosity is significantly enhanced. Even in this case, it is possible to observe the formation of nanoparticles with very angular shapes at the boundaries of big dolomite clasts (detail in Fig. 35e).

4.4.3.2 Comparison between experimentally produced microstructures and natural materials

In both sheared samples with SHIVA (Fig. 36a) and natural samples (Fig. 36b), we observed a redistribution of calcite along the slip surface and more generally in the gouge layer. Calcite forms a white and thin (few μm thick) layer parallel to the fault plane in the experiments with Argon as pore fluid (Fig. 36a). A similar situation is recognizable in some natural samples, where calcite forms bright, thicker (200 μm thick in Fig. 36b) layers close to the slip surface. Calcite also seals pores and fractures, resulting in a sort of cement crystallized between dolomite clasts (Figs. 36a, c, d), even in absence of water (Fig. 33). This cement was observed in several natural samples and then reproduced with both wet (water as pore fluid) and dry (Argon as pore fluids) experiments at high slip velocities (v=1 m/s).

During fast experiments (v=1 m/s) with Argon at high normal stress of 6 MPa, we observed some truncated clasts that usually occur at seismic slip velocities. In this case, truncated clasts are elongated in the shear direction (Fig. 36e). The same features can be observed in the natural samples, where clasts are often cut by the slip surface (Fig. 36f). In the natural material, we also found dolomite clasts surrounded by fluid-like structures (Fig. 36g). We observed similar structures near the dolomite clasts of the experimentally produced microstructures in dry conditions. These structures consist of dolomite clasts with sigmoidal contrails of very comminute and bright clasts at the SEM image (Fig. 36h).

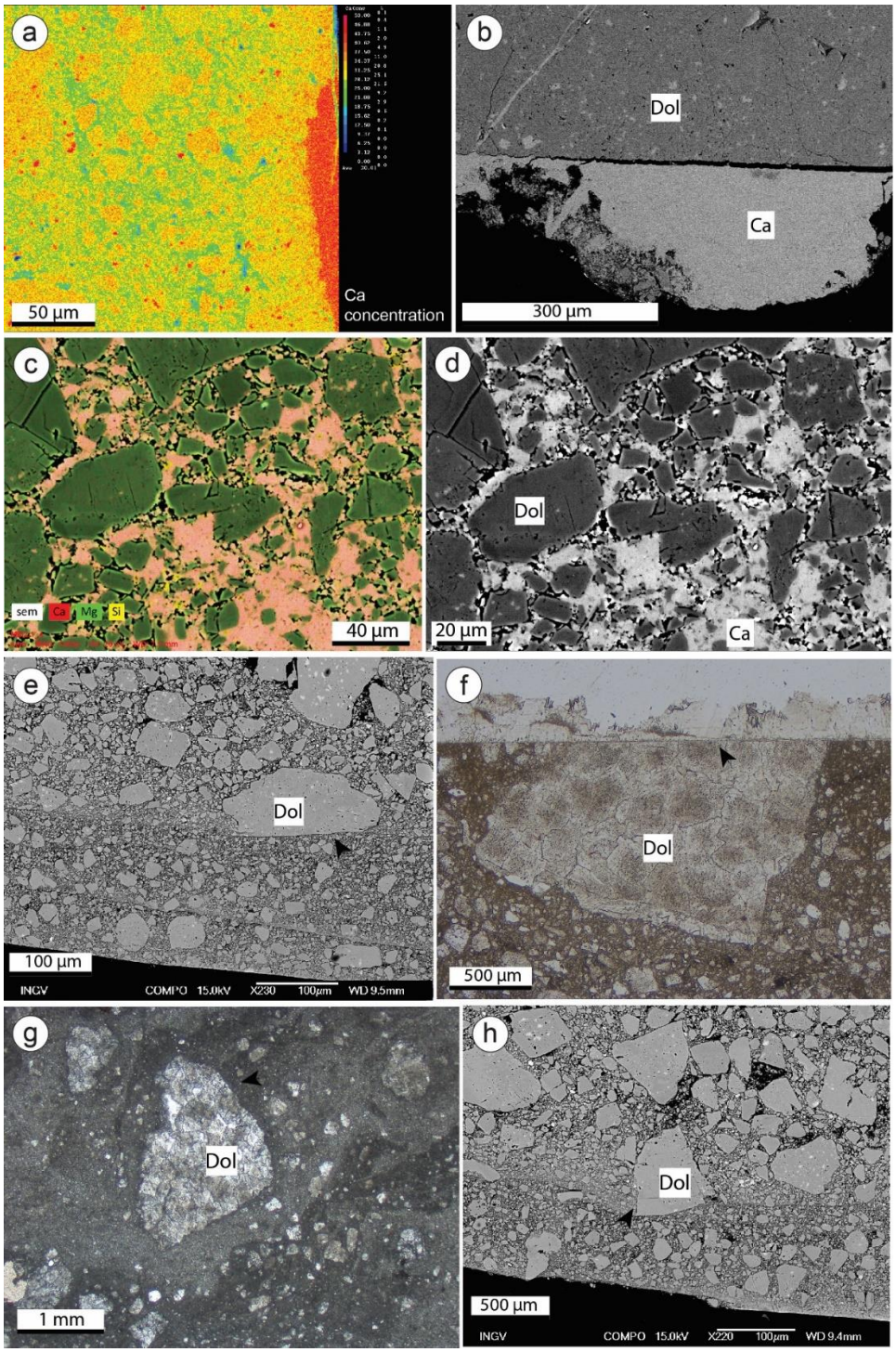

Figure 36: a) Compositional map representing Ca concentration and distribution after fast experiment (s 1706, see Table 2) with Argon as pore fluid. b) Scanning electron microscope (SEM) image showing distribution of Calcite along the slip surface and truncated clast of dolomite. c) Compositional map showing distribution of Calcium, Magnesium and Silicon on natural material collected along the Monte Marine Fault. d) Same sample with backscattered electron showing distribution of calcite cement among dolomite clasts. e) backscattered image of sample deformed by fast experiment with Argon as pore fluid (s 1706, see Table 2), with big dolomite truncated clast. e) Optical microscope image of natural sample with big dolomite truncated clast along the slip surface. f) Optical microscope image of natural sample with fluid-like structures around dolomite clasts. g) Scanning electron microscope (SEM) image of sample deformed with fast experiment (s 1706, see Table 2) and Argon as pore fluid showing sigmoidal contrails of small bright small clasts departing from dolomite clasts.

4.5 Discussion

4.5.1 Mechanical data

Preshear

During preshear at v=7 μm/s, samples have a slip-strengthening behavior. Samples compaction is significantly higher in wet conditions (water as pore fluid) than in dry conditions (Argon as pore fluid), independently of normal stress. This could be caused by the use of de-ionized water responsible for calcite dissolution. The different compaction curves surely produce some small heterogeneities in the studied samples that could affect the main pulse during the slow (0.001 m/s) and fast (1 m/s) experiments. Compaction and especially the low velocity applied are not large enough to cause fluid pressurization in the pore space. In fact, at V =7 μm/s the permeability of the gouge is high enough to continuously ri-equilibrate the pore pressure during shearing then the curve of pore pressure has a linear trend during the preshear. Preshear is important to equilibrate samples conditions before applying the main pulse, both from a mechanical and a structural point of view.

Slow slip rate experiments (main slip pulse at 0.001 m/s)

Even during slow experiments at v=0.001 m/s, pore fluid pressurization does not occur. In fact, the experiments were performed under drained conditions and shear compaction pressurization is fully compensated by the syringe pump B that equilibrates the pore pressure in the gouge layer. The velocity at which the shear stress is applied is not large enough to pressurize the water in the pore space. In fact, especially when Argon is used as pore fluid, sample strength has a velocity and slip neutral behavior.

Fast experiments (main slip pulse at 1 m/s)

During high velocity friction experiments (1 m/s) pressurization is activated after a first phase of dilation (Smith et al., 2015) during the experiment s1773. The phase of dilation in the experiment s1773 is almost instantaneous and lasts for less than 100 ms. Dilation is caused by grain interaction, work against the applied normal stress and grain fragmentation and is followed by a fast decrease in pore fluid pressure probably due to the increased pore volume. In the other three cases (s1774, s1775, s1706), when dilation is not measured, pressurization occurs in the first stages of shear stress application. Pressurization occurs when the pore fluid is compressed into the pore space due to fast shear compaction (Rempe et al., 2017). At high slip velocities, the gouge permeability properties do not allow for pore pressure ri-equilibration. Pressurization is strongly influenced by the properties of the pore fluid; pressurization is larger for liquid water than for Argon, which has a higher compressibility than the one of water. The larger compressibility of Argon in the pores results in

larger bulk compression of the gouge matrix. Moreover, calcite dissolution due to de-ionized water could contribute to sample shortening. With the same fluid, pressurization is directly proportional to normal stress and confinement pressure. The applied normal stress does not affect sample shortening neither in water, neither in Argon as pore fluid. In high velocity friction experiments, the trend of the normal stress curve is quite variable; this suggests that both the dilation and the pressurization occurring during shearing cause some instability in the piston, which fortunately does not affect the results of the experiments.

We can directly link the weakening in water experiments at the pressurization of pore water. The experiments show pressure drops with dilation (expansion of gouge) and then increases with compaction (reduction on pore volume). The mechanical data could be explained by a simple mechanical reduction of total stresses by pore fluid pressure. In fact, the measured shear stress (light green in color curve, Figs. 28, 29 and 30) is predicted by the Coulomb law: $\tau = \mu (\sigma n - Pf)$ from the normal stress σn and pore fluid pressure Pf measured experimentally and assuming a friction coefficient μ of calcite of 0.6, compatible with recent experimental measurements of ca. 0.65 (Scuderi et al., 2013). However, Coulomb law does not fully explain the evolution of shear strength during the dilatant acceleration phase (start of the experiment) and during the deceleration phase (end of the experiment).

4.5.2 The deformation processes active during the experiments

Despite this work provides for the first time a direct control of pore fluid pressure during high velocity friction experiments, in the past several experimental and microstructural studies investigated the mechanics of seismic slip in carbonate gouges of variable composition (100% calcite, 100% dolomite, dolomite-calcite mixtures, natural fault gouges), in a broad range of seismic slip rates (0.001 – 1 m/s) up to 26 MPa normal stresses. These studies tried to connect the dynamic weakening of experimental faults to the deformation processes controlling it (Table 4).

gouge	rh	rh vs wet	vd, rh, wet	fluid pressurized
100% cal	(Smith et al., 2013, 2015; Pozzi et al., 2018, 2019)	(Rempe et al., 2017)	(Rempe et al., 2014)	Rempe et al. (in proceedings)
50% cal 50% dol	(Smith et al., 2017) (Demurtas et al., 2019a)	(Demurtas et al., 2019b)		
20% cal 80% dol				This work
100 % dol	(De Paola et al., 2011b, 2011a; Fondriest et al., 2013)			
unclear	(De Paola et al., 2015)			

Table 4a: slow to high velocity friction experimental works on simulated or natural carbonate fault gouges.

rock	rh	vd, rh, wet	fluid pressurized, rh
carrara marble	(Han et al., 2007b, 2010; Spagnuolo et al., 2015)	(Violay et al., 2014)	(Violay et al., 2015)
dolomite marble	(Han et al., 2010)		

Table 4b: Slow to high velocity friction experimental works on simulated or natural carbonate fault rocks.

We should point out that our experiments using Argon as pore fluid are nominally dry and should compare with the experiments previously performed under room humidity conditions. At the same time, our experiments with water as pore fluid compare with the wet experiments. However, the previously published gouge experiments with water do not control the degree of saturation and most importantly do not measure the pore fluid pressure during slip. Moreover, thanks to the new experimental configuration and gouge holder (Fig. 26), fluid is confined within the gouge layer & downstream pore fluid circuit. So the fluid cannot escape from the gouge layer & sample holder interface as was the case of the previous experiments. This experimental configuration allows us, for the first time, to calculate the friction coefficient as $\mu=\tau/(\sigma n-Pf)$, though for comparison with available data from the literature we should consider the *apparent* friction coefficient $\mu a=\tau/\sigma$. In this framework, our results should be compared mostly with the published experiments on fault gouges with similar composition than ours: 50-50 dolomite-calcite mixtures (Demurtas et al., 2019a, 2019b) or 100% dolomite (De Paola et al., 2011b, 2011a; Fondriest et al., 2013), possibly at 5 MPa total normal stress (e.g. Demurtas et al., 2019b).

A widely observed feature found in all gouges and rocks tested under room or vacuum-dry conditions and approaching 1 m/s is the occurrence of nanoparticles, that develop from both calcite and dolomite (Han et al., 2007b; De Paola et al., 2011b, 2011a, 2015; Fondriest et al., 2013; Smith et al., 2013, 2015, 2017; Spagnuolo et al., 2015; Pozzi et al., 2018; Demurtas et al., 2019a). Among the several studies, Demurtas et al. (2019a) analysed a mixed fault gouge which is almost comparable to our material. Demurtas et al. (2019a) observed the formation of calcite along the PSZ during experiments in room-dry conditions and fast velocities (1.2 m/s). That material formed by rounded nanoparticles is similar to the white calcite layer formed along the slip surface in our fast

experiments at 1 m/s and normal stress of 6 MPa in dry conditions (Fig. 36). Since Demurtas et al. (2019a) studied the formation of nanoparticles during friction experiments on a crushed gouge of Carrara marble with 50% dolomite and 50% calcite, we can reasonably expect some differences with respect to our results. In fact, we used a natural fault gouge of similar composition (80% dolomite and 20% calcite) but different origin (the material is a natural fault gouge collected from the Monte Marine fault). Perhaps this could explain the angularity of some nanoparticles formed in our experiments, which are significantly different, at least in some areas of our samples, from the more equidimensional nanograins with prevalent 120° triple junctions observed by Demurtas et al. (2019a) (this is not the case of nanograins in the calcite layer). They recognized a decomposed layer and a partially decomposed layer of calcite near the PSS (Principal Slip Surface). We found a similar decomposed layer of calcite localized along the slip surface (Fig. 36d), while partly decomposed calcite material is concentrated at the boundaries between calcite and dolomite grains.

Fondriest et al. (2013) worked with a 100% dolomitic fault gouge in dry conditions. They produced mirror-like slip surfaces in dolostone gouge only when sheared at seismic slip rates and concluded that the presence of fault mirrors truncating dolomite grains could be a geological marker of seismic slip. Our experiments seem to confirm this hypothesis: given the imposed slip rate of 0.5 m, we produced mirror-like slip surfaces only during the experiment at 1 m/s in dry conditions and normal stress of 6 MPa (s1706). In the other cases, we could not form mirror-like slip surfaces.

Among the recent studies reporting results of experiments on carbonate gouges with variable water content, authors studied 100% calcite gouges (Rempe et al., 2014, 2017), 50-50% calcite-dolomite mixtures (Demurtas et al., 2019b). In particular, Rempe et al. (2014) focused on the occurrence of CCA (clast cortex aggregates) as possible evidence of coseismic slip. They conclude that the formation of CCA occurred at low normal stresses and dry conditions. However, our experiments show scarce occurrence of CCA, at either low (0.001 m/s) or high (1 m/s) velocities. In Rempe et al. (2017), they studied the progressive strain localization during high velocity shear experiments by using some strain markers. They focused on the different mechanisms of strain localization in both water-dampened and room-humidity conditions and found that faster dynamic weakening in water-dampened conditions happens because of a different, or more efficient, weakening mechanisms and not a faster localization in water. Nevertheless, during microstructural studies we found interesting bands of extreme localization alternated to bands of lower localization and higher porosity formed during experiments at 1 m/s in water-dampened conditions (s1699) that still need to be understood. We observed that the more comminute bands are thinner with respect to the

ones with higher porosity. This could mean that comminution is caused by a major localization of deformation in low porosity layers. In our case, the assessment on whether the degree of localization was enhanced under water-saturated conditions cannot be performed due to probable partial sampling of the argon-dry gouge layer. The compositional layering observed in water-dampened conditions at 5 MPa and 1 m/s (Fig. 31) is comparable to co-seismic foliations produced by Smith et al., 2017 that, differently from the other authors, worked in room-dry conditions using a 50% dolomite – 50% calcite gouge sheared at <1.13 m/s. The reproducibility at high slip rates of similar microstructures during our experiments testifies that, even if the foliations produced by Smith et al., 2017 differ for a smaller thickness and different orientation with respect to the principal slip surface, following Smith et al., 2017, compositional layering is an evidence of co-seismic slip in carbonate fault gouges.

Demurtas et al. (2019b) instead observed the development of a CPO by cataclasis in the surrounding of the localized PSZ, favoured by dolomite and calcite cleavage planes. However, they did not observe differences in dynamic weakening between dry and wet cases, probably related to fluid escape from the slipping zone during the loading at the high normal stress they used (17.5 MPa).

4.5.3 Friction experiments versus natural observations

The comparison between the microstructures obtained with the friction experiments and that observed on the natural cohesive samples demonstrates that friction experiments well describe the conditions of the MMF. In particular, the results of this study suggest that the fault was deformed under dry conditions. This is in agreement with the occurrence of huge amounts of loose material that could have created a sort of barrier for the flow of fluids. In this sense, detailed hydrogeological investigations on the circuits described by fluids across the MMF would be necessary to support this statement, in particular in the central part of the fault zone, where the structural architecture of the fault is very complex and the amount of shattered rocks is considerable. In fact, in this area we did not observed, at the outcrop scale, the same fluid-like structures found near Barete; this is a further sign of the absence of water during fault deformation in the step-over zone. In our experiments, we generally observed that slip produces cataclasites with different degree of comminution and amount of porosity. The same variability can be found in the natural samples collected from the MMF without alterned bands of different composition. It is important to remember that the microstructures found in the natural samples were probably orginated by multiple phases of fault deformation (fault reactivations), while the results of our experiments derive from a single pulse of

slip along a newly formed slip surface. In this sense, further experiments able to simulate fault reactivation would be recommended to validate the comparison between results from laboratory and nature.

4.6 Conclusions

In this paper, we performed innovative pressurized experiments on natural fault gouges from a carbonate-hosted natural fault (Monte Marine Fault, Cortinovis et al., 2018) to understand which where the active deformation processes during fault slip. The experiments were performed at effective normal stresses of 1 and 5 MPa, slip rates of 0.001 and 1 m/s (for 0.5 m of slip), and using either Argon and water as pore fluid. Our main conclusions are the following:

1. In experiments with water as pore fluid, cataclasis appears to dominate at both low (1 mm/s) and high (1 m/s) slip rates. Only at 1 m/s, pressurization of pore water controls the measured strength of the fault, which is instead fully drained at 0.001 m/s.

2. In experiments with Argon as pore fluid, cataclasis governs strength at low slip rates (1 mm/s) and thermo-mechanical processes dominate at high slip rates (1 m/s). In the latter, nanoparticle-rich volumes are associated to evidences of thermal decomposition of dolomite and calcite (bubbles in Fig. 33e) and sintering of calcite and dolomite grains. Grain size- and temperature-dependent processes weaken the solid matrix of grains and are associated to a negligible increase of the pore fluid pressure.

3. Natural gouges retrieved from the Monte Marine Fault appear to be similar to those produced in the experiments with Argon (room-humidity conditions). This is inferred by the comparison between experimentally produced microstructures and field evidences. Our observations help to constrain the conditions at which fault slip occurred along the MMF and hypothesize that the faults rocks found along the MMF were produced by seismic ruptures propagating in a fluid-poor environment at alternated high and slow slip rates during the seismic cycle.

4.7 Acknowledgements

E. Spagnuolo, B. Carpenter, M. Scuderi and G. Romeo are thanked for suggestions and help in the design of the pressurized gouge holder. L. Mantovani is thanked for her support during XRD analysis.

S. Aretusini and S. Cortinovis performed friction experiments and collaborated during microstructural studies. S. Cortinovis wrote this manuscript reviewed by S. Aretusini. M. Nazzari helped during SEM analyses and acquired compositional maps with EMPA. G. Di Toro and F. Balsamo critically reviewed this manuscript.

S. Aretusini and G. Di Toro were supported by the European Research Council Consolidator Grant Project No. 614705 NOFEAR.

5 General conclusions

The results of this PhD thesis confirm that seismogenic and active fault zones in complex structural settings (e.g. the Apennine fold-and-thrust belt) are influenced by multiple factors such as the presence of inherited structures, different lithology, different fault deformation rates (seismic vs aseismic slip along faults) and presence/absence of fluids during fault deformation.

In this thesis, we analysed all these mentioned factors and we list here, summarized in the following points, the main results arising from this study:

1) Analytical technique constitutes one of the major controls in the calculation of fractal dimension in carbonate rocks. The use of invasive analytical procedures can produce biases in the results due to sample deterioration and fragmentation during analyses. Among the methodologies available for the characterization of carbonate rocks, the multi-scale image analysis is the best tool to acquire precise data over different scales. Despite being a time-consuming methodology, image analysis gives to the operator a good control on the sample during analyses, especially in the case of heterogeneous carbonate rocks.
2) The Monte Marine Fault is a complex seismogenic area with a very old history (starting from the Jurassic). This fault is shaped by the occurrence of minor faults strands of different kinematics formed during the Apennine compression and the late Quaternary extension. The fault core of the Monte Marine fault is formed by cataclasites, ultra-cataclasites and breccias and changes in thickness along the fault strike. It is out of range with respect to the classical fault cores described in the previous works due to the presence of huge amounts of loose material that we classify as shattered rocks. Field observations linked with petrophysical analyses result in the formulation of a cyclic model that describes the evolution of the Monte Marine Fault with alternated phases of fault creeping, with progressive strain localization along the major slip surfaces, and earthquake ruptures, associated to the wave propagation and likely responsible for the formation of the shattered rocks.
3) Water plays an important role in driving co-seismic rupture. It can generate chemical-physical reactions that help to lubricate fault planes and favor samples weakening. The experiments performed in wet and dry conditions on the natural gouge from the Monte Marine Fault demonstrate that pressurization occurs in wet conditions at 1 m/s and different effective normal stress of 1 MPa and 5 MPa. Pressurization can occur even in dry conditions, when Argon is the pore fluid. Nevertheless, pressurization is significantly lower in dry conditions because Argon,

more compressible than water, allows for pore space deformation and consequent pore pressure reduction. Microstructural investigations show that nanoparticles can form in dry conditions at 1 m/s. Nanoparticles develop mainly in calcite for processes of decomposition and sintering. At high slip rates (1 m/s) we observed the formation of a compositional layering made by the alternation of Mg- and Ca- rich layers resembling the co-seismic foliations of Smith et al., (2017) formed in dry conditions. The comparison between experimentally and naturally produced microstructures proves that slip along principal and secondary slip surfaces along the Monte Marine Fault likely occurred in dry conditions.

6 Open questions and future perspectives

The conclusions listed in the previous chapter show that this thesis furnished some guidelines to classify fault core carbonate rocks, helped to increase the knowledge on the structural architecture and petrophysical properties of the Monte Marine fault, and was useful to better understand the role of fluids during the seismic cycle in carbonate rocks. Nevertheless, some questions remain open and a lot of work is still required to unravel the formation and evolution of the MMF, understand how shattered rocks form in many different settings along active/seismogenic faults, and interpret the role of fluid during the seismic rupture.

About the Monte Marine Fault, it would be interesting to extend the detailed field mapping to other interesting areas of the fault zone (e.g. the southern tip of the fault). It would also be useful to perform other structural cross sections across the main fault to better retrace secondary faults. Data collected in the field could be used to build a 3D model (e.g. using the 3D Move software) to better and easily represent the structure of the fault.

The use of geophysical tools such as geoelectric surveys could be useful to describe the deep structure of the fault and describe the relationships between the main fault and the minor fault segments (thrust faults, secondary extensional faults and strike slip faults). Moreover, geophysical investigations would be used to study if shattered rocks are present at depth.

About experimental studies, it would be interesting to repeat the same experiments on the sheared samples to simulate fault reactivation. Moreover, during experiments, it would be useful to measure temperature to investigate its variations at different slip rates.

Hydrogeological investigations on the MMF would also be interesting. Hydrogeological data would be fundamental to understand the role of the shattered rocks in controlling the fluid flow across the fault zone.

List of references

Agosta, F., Aydin, A., 2006. Architecture and deformation mechanism of a basin-bounding normal fault in Mesozoic platform carbonates, central Italy. Journal of Structural Geology 28, 1445–1467. https://doi.org/10.1016/j.jsg.2006.04.006

Agosta, F., Prasad, M., Aydin, A., 2007. Physical properties of carbonate fault rocks, fucino basin (Central Italy): Implications for fault seal in platform carbonates. Geofluids 7, 19–32. https://doi.org/10.1111/j.1468-8123.2006.00158.x

Allègre, C.J., Le Mouel, J.L., Provost, A., 1982. Scaling rules in rock fracture and possible implications for earthquake prediction. Nature 297, 47–49. https://doi.org/10.1038/297047a0

An Lin, J., Sammis, C.G., 1994. Particle Size Distribution of Cataclastic Fault Materials from Southern California: A 3-D Study. Pageoph. 143.

Anthony, J.L., Marone, C., 2005. Influence of particle characteristics on granular friction. Journal of Geophysical Research B: Solid Earth 110, 1–14. https://doi.org/10.1029/2004JB003399

Balsamo, F., Clemenzi, L., Storti, F., Mozafari, M., Solum, J., Swennen, R., Taberner, C., Tueckmantel, C., 2016. Anatomy and paleofluid evolution of laterally restricted extensional fault zones in the Jabal Qusaybah anticline, Salakh arch, Oman. Geological Society of America Bulletin 128, 957–972. https://doi.org/10.1130/B31317.1

Balsamo, F., Storti, F., 2011. Size-dependent comminution, tectonic mixing, and sealing behaviour of a “structurally oversimplified” fault zone in poorly lithified sands: Evidence for a coseismic rupture? Bulletin of the Geological Society of America 123, 601–619. https://doi.org/10.1130/B30099.1

Balsamo, F., Storti, F., 2010. Grain size and permeability evolution of soft-sediment extensional sub-seismic and seismic fault zones in high-porosity sediments from the Crotone basin, southern Apennines, Italy. Marine and Petroleum Geology 27, 822–837. https://doi.org/10.1016/j.marpetgeo.2009.10.016

Bigi, S., Pisani, P.C., 2005. From a deformed Peri-Tethyan carbonate platform to a fold-and-thrust-belt: An example from the Central Apennines (Italy). Journal of Structural Geology 27, 523–539. https://doi.org/10.1016/j.jsg.2004.10.005

Billi, A., 2010. Microtectonics of low-P low-T carbonate fault rocks. Journal of Structural Geology 32, 1392–1402. https://doi.org/10.1016/j.jsg.2009.05.007

Billi, A., Storti, F., 2004. Fractal distribution of particle size in carbonate cataclastic rocks from the core of a regional strike-slip fault zone. Tectonophysics 384, 115–128. https://doi.org/10.1016/j.tecto.2004.03.015

Blenkinsop, T.G., 1991. Cataclasis and processes of particle size reduction. Pure and Applied Geophysics PAGEOPH 136, 59–86. https://doi.org/10.1007/BF00878888

Boer, D.G.B.., Weerd, D.C., Thoenes, D., Goossens, H.W.J., 1987. Laser diffraction spectrometry : Fraunhofer diffraction versus Mie scattering. Particle and Particle Systems Characterization 4, 14–19. https://doi.org/10.1002/ppsc.19870040104

Burek, R., 1976. PARTICLE SIZE EFFECTS IN X-RAY ABSORPTION ANALYSIS: FORMULAE FOR SIZE DISTRIBUTIONS. Journal of Radioanalytical Chemistry 33, 263–264.

Caine, J.S., Evans, J.P., Forster, C.B., 1996. Fault zone architechture and permeability structure. Geology 24, 1025–1028. https://doi.org/10.1130/0091-7613(1996)024<1025

Calamita, F., Pizzi, A., 1992. Tettonica quaternaria nella dorsale appenninica umbro-marchigiana e bacini intrappenninici associati.

Carminati, E., Doglioni, C., Scrocca, D., 2004. Alps vs Apennines. Special Volume of the Italian Geological Society for the IGC 32 Florence-2004 141–151.

Carminati, E., Lustrino, M., Doglioni, C., 2012. Geodynamic evolution of the central and western Mediterranean: Tectonics vs. igneous petrology constraints. Tectonophysics 579, 173–192. https://doi.org/10.1016/j.tecto.2012.01.026

Cello, G., Mazzoli, S., Tondi, E., Turco, E., 1997. Active tectonics in the central Apennines and possible implications for seismic hazard analysis in peninsular Italy. Tectonophysics 272, 43–68. https://doi.org/10.1016/S0040-1951(96)00275-2

Chiodini, G., Cioni, R., 1989. Gas geobarometry for hydrothermal systems and its application to some Italian geothermal areas. 4, 465–472.

Choi, J.H., Edwards, P., Ko, K., Kim, Y.S., 2016. Definition and classification of fault damage zones: A review and a new methodological approach. Earth-Science Reviews 152, 70–87. https://doi.org/10.1016/j.earscirev.2015.11.006

Collettini, C., Barchi, M.R., 2002. A low-angle normal fault in the Umbria region (Central Italy): a mechanical model for the related microseismicity. Tectonophysics 359, 97–115.

Cortinovis, S., Balsamo, F., Storti, F., 2019. Influence of analytical operating procedures on particle size distributions in carbonate cataclastic rocks. Journal of Structural Geology 128. https://doi.org/10.1016/j.jsg.2019.103884

De Paola, N., Chiodini, G., Hirose, T., Cardellini, C., Caliro, S., Shimamoto, T., 2011a. The geochemical signature caused by earthquake propagation in carbonate-hosted faults. Earth and Planetary Science Letters 310, 225–232. https://doi.org/10.1016/j.epsl.2011.09.001

De Paola, N., Hirose, T., Mitchell, T., Di Toro, G., Viti, C., Shimamoto, T., 2011b. Fault lubrication and earthquake propagation in thermally unstable rocks. Geology 39, 35–38. https://doi.org/10.1130/G31398.1

De Paola, N., Holdsworth, R.E., Viti, C., Collettini, C., Bullock, R., 2015. Can grain size sensitive flow lubricate faults during the initial stages of earthquake propagation? Earth and Planetary Science Letters 431, 48–58. https://doi.org/10.1016/j.epsl.2015.09.002

Demurtas, M., Fondriest, M., Balsamo, F., Clemenzi, L., Storti, F., Bistacchi, A., Di Toro, G., 2016. Structure of a normal seismogenic fault zone in carbonates: The Vado di Corno Fault, Campo Imperatore, Central Apennines (Italy). Journal of Structural Geology 90, 185–206. https://doi.org/10.1016/j.jsg.2016.08.004

Demurtas, M., Smith, S.A.F., Prior, D.J., Brenker, F.E., Di Toro, G., 2019a. Grain size sensitive creep during simulated seismic slip in nanogranular fault gouges: constraints from Transmission Kikuchi Diffraction (TKD). Journal of Geophysical Research: Solid Earth.

https://doi.org/10.1029/2019jb018071

Demurtas, M., Smith, S.A.F., Prior, D.J., Spagnuolo, E., Di Toro, G., 2019b. Development of crystallographic preferred orientation during cataclasis in low-temperature carbonate fault gouge. Journal of Structural Geology 126, 37–50. https://doi.org/10.1016/j.jsg.2019.04.015

Di Luccio, F., Ventura, G., Di Giovambattista, R., Piscini, A., Cinti, F.R., 2010. Correction to "Normal faults and thrusts reactivated by deep fluids: The 6 April 2009 M w 6.3 L'Aquila earthquake, central Italy." Journal of Geophysical Research 115. https://doi.org/10.1029/2009JB007190

Di Toro, G., Niemeijer, A., Tripoli, A., Nielsen, S., Di Felice, F., Scarlato, P., Giuseppe, S., Alessandroni, R., Romeo, G., Di Stefano, G., Smith, S., Spagnuolo, E., Mariano, S., 2010. From field geology to earthquake simulation : a new state-of-the-art tool to investigate rock friction. Rendiconti Fisica Accademia Dei Lincei 21, 95–114. https://doi.org/10.1007/s12210-010-0097-x

Doglioni, C., 1991. A proposal for the kinematic modelling of W-dipping subduction - possible application to the Tyrrenian-Apennines system. Terra Nova 3, 423–434.

Epstein, B., 1947. The mathematical description of certain breakage mechanisms leading to the logarithmico-normal distribution. Journal of the Franklin Institute 244, 471–477. https://doi.org/10.1016/0016-0032(47)90465-1

Falcucci, E., Gori, S., Moro, M., Fubelli, G., Saroli, M., Chiarabba, C., Galadini, F., 2015. Deep reaching versus vertically restricted Quaternary normal faults: Implications on seismic potential assessment in tectonically active regions: Lessons from the middle Aterno valley fault system, central Italy. Tectonophysics 651, 186–198. https://doi.org/10.1016/j.tecto.2015.03.021

Ferraro, F., Grieco, D.S., Agosta, F., Prosser, G., 2018. Space-time evolution of cataclasis in carbonate fault zones. Journal of Structural Geology 110, 45–64. https://doi.org/10.1016/j.jsg.2018.02.007

Fondriest, M., Aretusini, S., Di Toro, G., Smith, S.A.F., 2015. Fracturing and rock pulverization along an exhumed seismogenic fault zone in dolostones: The Foiana Fault Zone (Southern Alps, Italy). Tectonophysics 654, 56–74. https://doi.org/10.1016/j.tecto.2015.04.015

Fondriest, M., Smith, S.A.F., Candela, T., Nielsen, S.B., Mair, K., Toro, G. Di, 2013. Mirror-like faults and power dissipation during earthquakes. Geology 41, 1175–1178. https://doi.org/10.1130/G34641.1

Fondriest, M., Smith, S.A.F., Di Toro, G., Zampieri, D., Mittempergher, S., 2012. Fault zone structure and seismic slip localization in dolostones, an example from the Southern Alps, Italy. Journal of Structural Geology 45, 52–67. https://doi.org/10.1016/j.jsg.2012.06.014

Frost, E., Dolan, J., Sammis, C., Hacker, B., Cole, J., Ratschbacher, L., 2009. Progressive strain localization in a major strike-slip fault exhumed from midseismogenic depths: Structural observations from the Salzach-Ennstal- Mariazell-Puchberg fault system, Austria. Journal of Geophysical Research: Solid Earth 114, 1–14. https://doi.org/10.1029/2008JB005763

Galadini, F., 1999. Pleistocene changes in the central Apennine fault kinematics: A key to decipher active tectonics in central Italy. Tectonics 18, 877–894.

Galadini, F., Galli, P., 2000. Active Tectonics in the Central Apennines (Italy) – Input Data for

Seismic Hazard Assessment. Natural Hazards 22, 225–270. https://doi.org/10.1023/A:1008149531980

Galadini, F., Messina, P., 2004. Early-Middle Pleistocene eastward migration of the Abruzzi Apennine (central Italy) extensional domain. Journal of Geodynamics 37, 57–81. https://doi.org/10.1016/j.jog.2003.10.002

Galadini, F., Messina, P., Irtr, C.N.R., Recente, T., Tor, R., 2001. Galadini_2001_Plio-Quaternary changes of the normal_Geodinamica Acta. 14, 1–24.

Galadini, F., Messina, P., Sposato, A., 2000. Tettonica quaternaria nell´Appennino centrale e caratterizzazione dell´attività di faglie nel Pleistocene superiore-Olocene. Gndt 1–12.

Galli, P.A.C., Giaccio, B., Messina, P., Peronace, E., Zuppi, G.M., 2011. Palaeoseismology of the L'Aquila faults (central Italy, 2009, Mw 6.3 earthquake): Implications for active fault linkage. Geophysical Journal International 187, 1119–1134. https://doi.org/10.1111/j.1365-246X.2011.05233.x

Ghisetti, F., Vezzani, L., 1999. Depth and modes of Pliocene-Pleistocene crustal extension of the Apennines (Italy). Terra Nova 11, 67–72.

Han, R., Hirose, T., Shimamoto, T., 2010. Strong velocity weakening and powder lubrication of simulated carbonate faults at seismic slip rates. Journal of Geophysical Research: Solid Earth 115. https://doi.org/10.1029/2008JB006136

Han, R., Shimamoto, T., Ando, J.I., Ree, J.H., 2007a. Seismic slip record in carbonate-bearing fault zones: An insight from high-velocity friction experiments on siderite gouge. Geology 35, 1131–1134. https://doi.org/10.1130/G24106A.1

Han, R., Shimamoto, T., Hirose, T., Ree, J.-H., Ando, J., 2007b. Ultralow Friction of Carbonate Faults. Science 316, 878–880.

Hausegger, S., Kurz, W., Rabitsch, R., Kiechl, E., Brosch, F.J., 2010. Analysis of the internal structure of a carbonate damage zone: Implications for the mechanisms of fault breccia formation and fluid flow. Journal of Structural Geology 32, 1349–1362. https://doi.org/10.1016/j.jsg.2009.04.014

Heilbronner, R.R., Keulen, N., 2006. Grain size and grain shape analysis of fault rocks. Tectonophysics 427, 199–216. https://doi.org/10.1016/j.tecto.2006.05.020

Keulen, N., Heilbronner, R., Stünitz, H., Boullier, A.M., Ito, H., 2007. Grain size distributions of fault rocks: A comparison between experimentally and naturally deformed granitoids. Journal of Structural Geology 29, 1282–1300. https://doi.org/10.1016/j.jsg.2007.04.003

Kimura, S., Ito, T., Minagawa, H., 2018. Grain-size analysis of fine and coarse non-plastic grains: comparison of different analysis methods. Granular Matter 20, 50. https://doi.org/10.1007/s10035-018-0820-3

Kostakioti, A., Xypolias, P., Kokkalas, S., Doutsos, T., 2004. Q Uantitative Analysis of Deformation Along the Fault Damage Zone of the Klimatia Thrust (Nw Greece , Ionian Zone). Society XXXVI, 1643–1651.

Ma, S., Andrews, D.J., 2010. Inelastic off - fault response and three - dimensional dynamics of earthquake rupture on a strike - slip fault. 115, 1–16. https://doi.org/10.1029/2009JB006382

Mavko, G., Mukerji, T., & Dvorkin, J. (2009). The Rock Physics Handbook: Tools for Seismic Analysis of Porous Media. Cambridge: Cambridge University Press. doi:10.1017/CBO9780511626753

Micarelli, L., Benedicto, A., Wibberley, C.A.J., 2006. Structural evolution and permeability of normal fault zones in highly porous carbonate rocks. Journal of Structural Geology 28, 1214–1227. https://doi.org/10.1016/j.jsg.2006.03.036

Micarelli, L., Moretti, I., Daniel, J.M., 2003. Structural properties of rift-related normal faults: The case study of the Gulf of Corinth, Greece. Journal of Geodynamics 36, 275–303. https://doi.org/10.1016/S0264-3707(03)00051-6

Miller, S.A., Collettini, C., Chiaraluce, L., Cocco, M., Barchi, M., Kaus, B.J.P., 2004. Aftershocks driven by a high-pressure CO2source at depth. Nature 427, 724–727. https://doi.org/10.1038/nature02251

Mitchell, T.M., Ben-Zion, Y., Shimamoto, T., 2011. Pulverized fault rocks and damage asymmetry along the Arima-Takatsuki Tectonic Line, Japan. Earth and Planetary Science Letters 308, 284–297. https://doi.org/10.1016/j.epsl.2011.04.023

Mizoguchi, K., Hirose, T., Shimamoto, T., Fukuyama, E., 2007. Reconstruction of seismic faulting by high-velocity friction experiments : An example of the 1995 Kobe Earthquake. Geophysical Research Letters 34. https://doi.org/10.1029/2006GL027931

Morewood, N.C., Roberts, G.P., 2004. Morewood_2000_The geometry kinematics and rates_Journal of Structural Geology. 22, 1–21.

Moro, M., Bosi, V., Galadini, F., Galli, P., Messina, P., Sposato, A., 2002. Analisi paleosismologiche lungo la faglia del M. Marine (Alta valle dell'Aterno): Risultati Preliminari. Italian Journal of Quaternary Sciences 15, 267–278.

Moro, M., Falcucci, E., Gori, S., Saroli, M., Galadini, F., 2016. New paleoseismic data across the Mt. Marine fault between the 2016 amatrice and 2009 l???aquila seismic sequences (central apennines). Annals of Geophysics 59, 1–7. https://doi.org/10.4401/ag-7260

Niemeijer, A., Di Toro, G., Griffith, W.A., Bistacchi, A., Smith, S.A.F., Nielsen, S., 2012. Inferring earthquake physics and chemistry using an integrated fi eld and laboratory approach. 39, 2–36. https://doi.org/10.1016/j.jsg.2012.02.018

Okubo, K., Bhat, H.S., Rougier, E., Marty, S., Schubnel, A., Lei, Z., Earl, E., Klinger, Y., 2019. Dynamics, radiation and overall energy budget of earthquake rupture with coseismic off-fault damage. Journal of Geophisical Research: Solid Earth.

Pace, B., Boncio, P., Lavecchia, G., 2002. The 1984 Abruzzo earthquake (Italy): An example of seismogenic process controlled by interaction between differently oriented synkinematic faults. Tectonophysics 350, 237–254. https://doi.org/10.1016/S0040-1951(02)00118-X

Papanikolaou, I.D., Roberts, G.P., Michetti, A.M., 2005. Fault scarps and deformation rates in Lazio-Abruzzo, Central Italy: Comparison between geological fault slip-rate and GPS data. Tectonophysics 408, 147–176. https://doi.org/10.1016/j.tecto.2005.05.043

Passelègue, F.X., Pimienta, L., Faulkner, D., Schubnel, A., Fortin, J., Guéguen, Y., 2018. Development and Recovery of Stress-Induced Elastic Anisotropy During Cyclic Loading Experiment on Westerly Granite. Geophysical Research Letters 45, 8156–8166. https://doi.org/10.1029/2018GL078434

Pizzati M., Balsamo F., Storti F., 2020. Displacement-dependent microstructural and petrophysical properties of deformation bands and gouges in poorly lithified sandstone deformed at shallow burial depth (Crotone Basin, Italy). Journal of Structural Geology.

Pozzi, G., De Paola, N., Holdsworth, R.E., Bowen, L., Nielsen, S.B., Dempsey, E.D., 2019. Coseismic ultramylonites: An investigation of nanoscale viscous flow and fault weakening during seismic slip. Earth and Planetary Science Letters 516, 164–175. https://doi.org/10.1016/j.epsl.2019.03.042

Pozzi, G., De Paola, N., Nielsen, S.B., Holdsworth, R.E., Bowen, L., 2018. A new interpretation for the nature and significance of mirror-like surfaces in experimental carbonate-hosted seismic faults. Geology 46, 583–586. https://doi.org/10.1130/G40197.1

Rempe, M., Mitchell, T., Renner, J., Nippress, S., Ben-Zion, Y., Rockwell, T., 2013. Damage and seismic velocity structure of pulverized rocks near the San Andreas Fault. Journal of Geophysical Research: Solid Earth 118, 2813–2831. https://doi.org/10.1002/jgrb.50184

Rempe, M., Smith, S., Mitchell, T., Hirose, T., Di Toro, G., 2017. The effect of water on strain localization in calcite fault gouge sheared at seismic slip rates. Journal of Structural Geology 97, 104–117. https://doi.org/10.1016/j.jsg.2017.02.007

Rempe, M., Smith, S.A.F., Ferri, F., Mitchell, T.M., Di Toro, G., 2014. Clast-cortex aggregates in experimental and natural calcite-bearing fault zones. Journal of Structural Geology 68, 142–157. https://doi.org/10.1016/j.jsg.2014.09.007

Rice, J.R., 2006. Heating and weakening of faults during earthquake slip. Journal of Geophysical Research: Solid Earth 111, 1–29. https://doi.org/10.1029/2005JB004006

Roberts, G.P., Michetti, A.M., 2004. Spatial and temporal variations in growth rates along active normal fault systems: An example from The Lazio-Abruzzo Apennines, central Italy. Journal of Structural Geology 26, 339–376. https://doi.org/10.1016/S0191-8141(03)00103-2

Sammis, C., King, G., Biegel, R., 1987. The kinematics of gouge deformation. Pure and Applied Geophysics PAGEOPH 125, 777–812. https://doi.org/10.1007/BF00878033

Sammis, C.G., Biegel, R.L., 1989. Fractals, Fault-Gouge, and Friction. Pageoph. 131.

Sammis, C.G., King, G.C.P., 2007. Mechanical origin of power law scaling in fault zone rock. Geophysical Research Letters 34, 2–5. https://doi.org/10.1029/2006GL028548

Savage, H.M., Brodsky, E.E., 2011. Collateral damage: Evolution with displacement of fracture distribution and secondary fault strands in fault damage zones. Journal of Geophysical Research: Solid Earth 116. https://doi.org/10.1029/2010JB007665

Schröckenfuchs, T., Bauer, H., Grasemann, B., Decker, K., 2015. Rock pulverization and localization of a strike-slip fault zone in dolomite rocks (Salzach-Ennstal-Mariazell-Puchberg fault, Austria). Journal of Structural Geology 78, 67–85. https://doi.org/10.1016/j.jsg.2015.06.009

Scuderi, M.M., Niemeijer, A.R., Collettini, C., Marone, C., 2013. Frictional properties and slip stability of active faults within carbonate-evaporite sequences: The role of dolomite and anhydrite. Earth and Planetary Science Letters 369–370, 220–232. https://doi.org/10.1016/j.epsl.2013.03.024

Sibson, R.H., 1992. Implications of fault-valve behaviour for rupture nucleation and recurrence.

Tectonophysics 211, 283–293. https://doi.org/10.1016/0040-1951(92)90065-E

Sibson, R.H., 1990. Rupture nucleation on unfavourably oriented faults. Bulletin - Seismological Society of America 80, 1580–1604.

Smeraglia, L., Aldega, L., Billi, A., Carminati, E., Doglioni, C., 2016. Phyllosilicate injection along extensional carbonate-hosted faults and implications for co-seismic slip propagation: Case studies from the central Apennines, Italy. Journal of Structural Geology 93, 29–50. https://doi.org/10.1016/j.jsg.2016.10.003

Smith, S.A.F., Di Toro, G., Kim, S., Ree, J.H., Nielsen, S., Billi, A., Spiess, R., 2013. Coseismic recrystallization during shallow earthquake slip. Geology 41, 63–66. https://doi.org/10.1130/G33588.1

Smith, S.A.F., Griffiths, J.R., Fondriest, M., Di Toro, G., 2017. "Coseismic Foliations" in Gouge and Cataclasite: Experimental Observations and Consequences for Interpreting the Fault Rock Record. Fault Zone Dynamic Processes: Evolution of Fault Properties During Seismic Rupture 81–102. https://doi.org/doi: 10.1002/9781119156895.ch5

Smith, S.A.F., Nielsen, S., Di Toro, G., 2015. Strain localization and the onset of dynamic weakening in calcite fault gouge. Earth and Planetary Science Letters 413, 25–36. https://doi.org/10.1016/j.epsl.2014.12.043

Soliva, R., Benedicto, A., Schultz, R.A., Maerten, L., Micarelli, L., 2008. Displacement and interaction of normal fault segments branched at depth: Implications for fault growth and potential earthquake rupture size. Journal of Structural Geology 30, 1288–1299. https://doi.org/10.1016/j.jsg.2008.07.005

Solum, J.G., Huisman, B.A.H., 2016. Toward the creation of models to predict static and dynamic fault-seal potential in carbonates. Petroleum Geoscience petgeo2016-044. https://doi.org/10.1144/petgeo2016-044

Spagnuolo, E., Plumper, O., Violay, M., Cavallo, A., Di Toro, G., 2015. Fast-moving dislocations trigger flash weakening in carbonate-bearing faults during earthquakes. Sci Rep 5, 16112. https://doi.org/10.1038/srep16112

Storti, F., Balsamo, F., 2010. Particle size distributions by laser diffraction: sensitivity of granular matter strength to analytical operating procedures. Solid Earth 1, 25–48. https://doi.org/10.5194/se-1-25-2010

Storti, Fabrizio, Balsamo, F., 2010. Impact of ephemeral cataclastic fabrics on laser diffraction particle size distribution analysis in loose carbonate fault breccia. Journal of Structural Geology 32, 507–522. https://doi.org/10.1016/j.jsg.2010.02.006

Storti, F., Balsamo, F., Salvini, F., 2007. Particle shape evolution in natural carbonate granular wear material. Terra Nova 19, 344–352. https://doi.org/10.1111/j.1365-3121.2007.00758.x

Storti, F., Billi, A., Salvini, F., 2003. Particle size distributions in natural carbonate fault rocks: Insights for non-self-similar cataclasis. Earth and Planetary Science Letters 206, 173–186. https://doi.org/10.1016/S0012-821X(02)01077-4

Stunitz, H., Keulen, N., Hirose, T., Heilbronner, R., 2010. Grain size distribution and microstructures of experimentally sheared granitoid gouge at coseismic slip rates - Criteria to distinguish seismic and aseismic faults? Journal of Structural Geology 32, 59–69.

https://doi.org/10.1016/j.jsg.2009.08.002

Tondi, E., Cello, G., 2003. Spatiotemporal evolution of the Central Apennines fault system (Italy). Journal of Geodynamics 36, 113–128. https://doi.org/10.1016/S0264-3707(03)00043-7

Turcotte, L., 1986. Fractals and Fragmentation. Journal of Geophysical Research 91, 1921–1926.

Vezzani, Livio & Festa, Andrea & Ghisetti, Francesca. (2016). Geological-Structural Map of the Central-Southern Apennines. Sheet1.

Violay, M., Di Toro, G., Nielsen, S., Spagnuolo, E., Burg, J.P., 2015. Thermo-mechanical pressurization of experimental faults in cohesive rocks during seismic slip. Earth and Planetary Science Letters 429, 1–10. https://doi.org/10.1016/j.epsl.2015.07.054

Violay, M., Nielsen, S., Gibert, B., Spagnuolo, E., Cavallo, A., Azais, P., Vinciguerra, S., Di Toro, G., 2014. Effect of water on the frictional behavior of cohesive rocks during earthquakes. Geology 42, 27–30. https://doi.org/10.1130/G34916.1

Violay, M., Nielsen, S., Spagnuolo, E., Cinti, D., Di Toro, G., Di Stefano, G., 2013. Pore fluid in experimental calcite-bearing faults: Abrupt weakening and geochemical signature of co-seismic processes. Earth and Planetary Science Letters 361, 74–84. https://doi.org/10.1016/j.epsl.2012.11.021

Zhong Yan Zhao, Yi, W., Xiao Han Liu, 1990. Fractal analysis applied to cataclastic rocks. Tectonophysics 178, 373–377. https://doi.org/10.1016/0040-1951(90)90159-6

7 Appendix: supplementary material to Chapter 2

7.1 Dry analysis

Parameters definition for dry laser granulometry

Air pressure determines the velocity at which the granular matter is lead into the system and ranges from 0 to 4 bar. Low air pressure values are generally recommended for fragile materials. Conversely, high air pressure values can exploit intraclast fractures to cause additional particle fragmentation during the migration of the material into the measure cell, significantly biasing the original grain size distribution. Feed rate determines the time required for the material to pass through the analyser and ranges from 0% to 100%. The proper feed rate is the one at which particles pass steadily from the sample lid into the analyser, allowing to achieve the appropriate range of laser obscuration required for reliable analyses. Measurement time control the duration of analysis (i.e. laser aperture).

Measurement time test

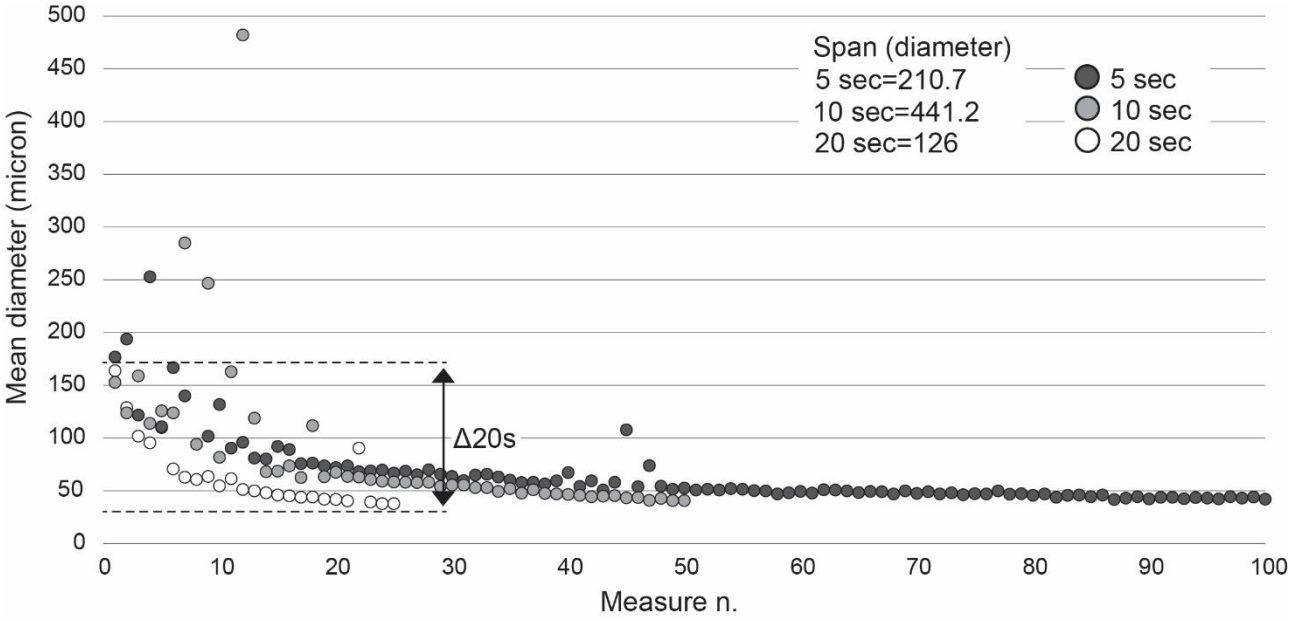

Figure S1: Results from measurement time test for dry laser granulometry plotted as mean diameter vs measurement number.

We performed three tests with different conditions and measurement duration: 100 measurements 5 seconds long, 50 measurements 10 seconds long, and 25 measurements 20 seconds long (Fig. S1). These three combinations of measurement number and duration ensure that sample is analysed for a total of 500 seconds in all the three cases. Looking at figure S1, from the first to the last measurement, we notice a variation of 126 µm in the clasts mean diameter in the 20s test; a

variation of 441.2 µm in the 10s test; and a variation of 210.7 µm in the 5s test. This means that, due to sample heterogeneities, 20s test minimizes diameter oscillations by averaging the grain size of clasts passing through the measurement chamber during laser aperture time. Vice versa, peaks observable in the 5s and 10s first measurements (up to ~470 m in the 10 sec test) are explainable assuming the passage of particularly big clasts in the measurement chamber during analysis. For these reasons, we can safely assume that fixing measurement duration at 20s ensures to acquire representative mean values of clasts diameter.

Air pressure, feed rate and reproducibility tests

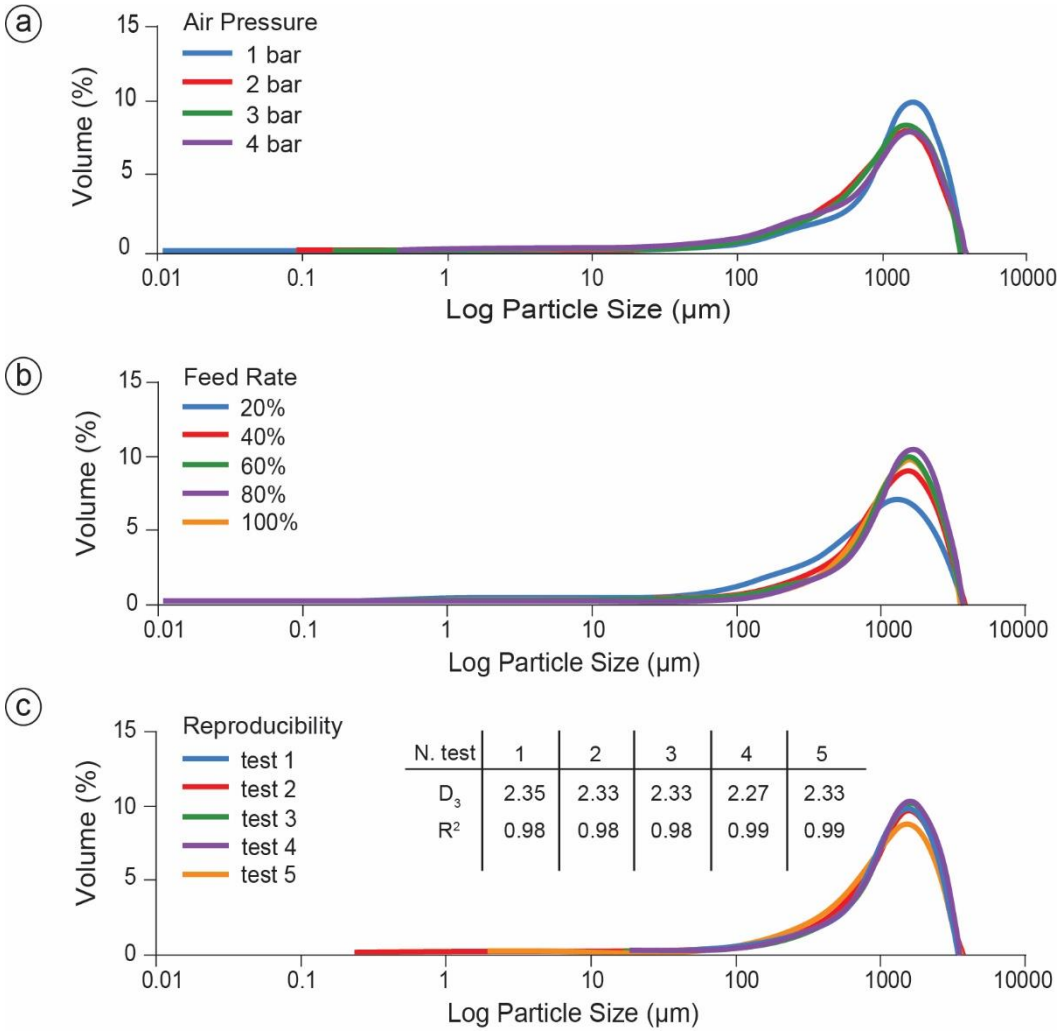

Figure S2: Results of dry analyses with laser granulometry during the definition of the SOP. Granulometric distributions obtained during the Air Pressure Test (a), the Feed Rate Test (b) and the Reproducibility Test (c). Values of fractal dimension (D3) obtained from the five repeated tests are reported in the table of Figure S2c.

Granulometric curves from the Air pressure test (Figure S2a) show very similar trends for grain size distributions at 2 to 4 bars of air pressure, while the curve obtained from measurements at 1 bar shows a higher abundance of particles coarser than about 1 mm of equivalent spherical

diameter. Data acquired at 2 and 3 bars show symmetric unimodal bell-shape distributions, with peaks at about 1500 µm. Conversely, data acquired at 1 and 4 bars have asymmetrical bell-shape particle size distributions, with peaks at about 1500 µm. The peak registered at 1 bar, which is significantly higher than the others, indicates that high air pressures induce particles breakage, responsible for decrease of peak value in tests performed at air pressures > 1 bar.

Granulometric curves from the feed rate test (Fig. S2b) show asymmetrical bell-shape distributions in all the tests. Nevertheless, data collected at 20% show lower amounts of particles coarser than about 1 µm and higher amounts of particles finer than this threshold value (Fig. S2b).

Results from the reproducibility tests (Fig. S2c) indicate that 4 out of the 5 measurements provided almost coincident curves of particle distribution. The only exception is represented by the curve associated with test 5 showing slightly lower amounts of coarse particles. The coincidence of the five D values supports the effectiveness of the selected operating procedure.

7.2 Wet analysis

Pump speed test

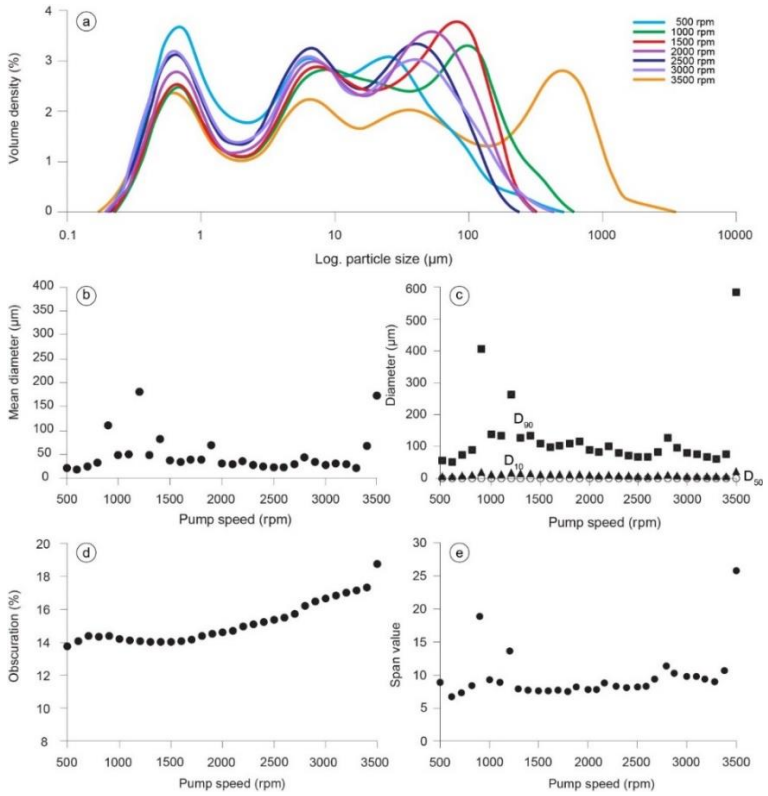

Figure S3: Volume density distribution versus log. particle size during pump speed test (a). Values of mean diameter (b), percentiles (c), obscuration (d) and span (e).

Pump speed test consists of performing measurement runs on sub-sample aliquots at different pump speed velocities and fixed measurement time. We decided to fix measurement time at 20s and increase pump speed from 500 rpm to 3500 rpm with incremental steps of 100 rpm (Fig. S3).

Granulometric curves represented in Fig. S3a, show trend variations at increasing pump speed, from 500 rpm to 3500 rpm (at intervals of 500 rpm). Overall, Fig. S3b shows around constant values of mean diameter that vary between 20 and 160 µm, even if many values vary just between ~18 and ~80 µm. Some exceptions are given by the values of 110 µm, 181 µm and 173 µm registered at respectively 900, 1200 and 3500 rpm. These high diameters represent particular coarse particles recirculating through the system. Fig. S3c shows the same situation but presenting data as percentiles: D_{10} and D_{50} are stable during the entire analysis, while D_{90} shows some oscillations that agree with the previous observations.

Values of obscuration in Fig. S3d vary from ~14% to ~19% are caused by sample deterioration in water. In fact, the increase in small particles number is directly proportional to the increase in laser obscuration. Sample deterioration causes an increase in fine particles number that is generated by particles disaggregation (i.e. production of small fragments due to opening of intraclast microfractures) and fragmentation (i.e. production of small fragments due to breakage of particles).

Measurement time test

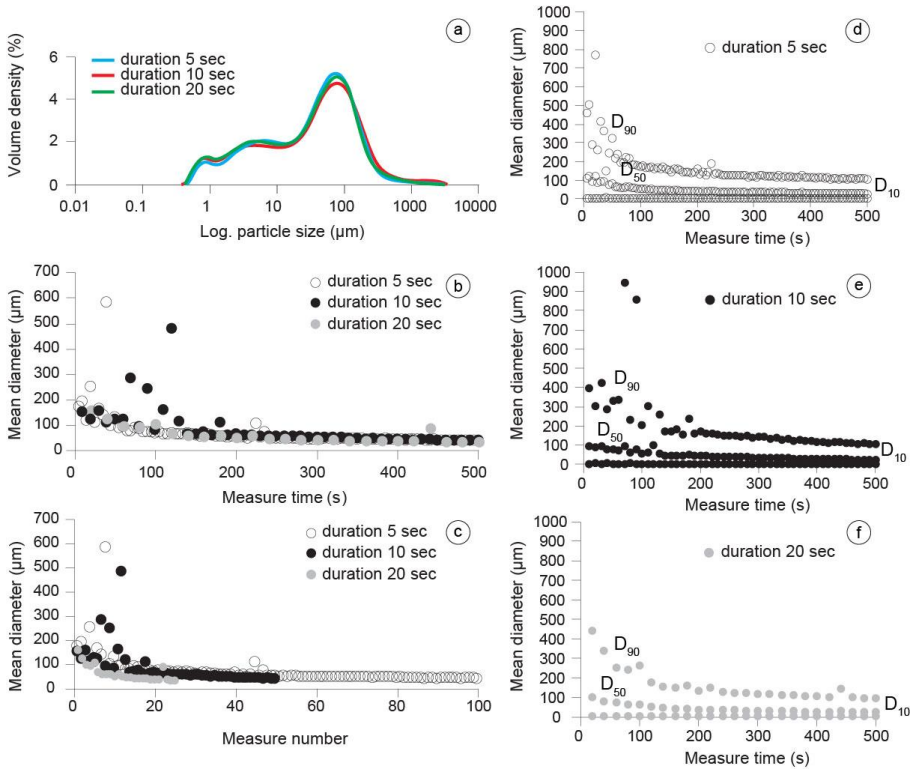

Figure S4: Volume density distribution versus log. particle size during the measurement time test. Values of mean diameter versus time (b) and measure number (c) and percentiles (d,e,f) are reported.

Measurement time test consists of changing sample duration at fixed pump speed velocity. We repeated the same test at three different durations (5s, 10s and 20s) and fixed pump velocity at 1700 rpm. Looking at granulometric distributions in Fig. S4a, results from the three different tests

seem to correspond. Nevertheless, values of mean diameter plotted versus measurement time (Fig. S4b) and versus number of measurements (Fig. S4c) are more scattered in the 5s and 10s tests than in the 20s test. In particular, 5s and 10s tests are characterized by anomalous amount of coarse particles (Figs. S4b,c). This is evident even in Figures S4d,e,f, which represent percentile values calculated over the 500 measures of each duration test. Data scattering registered during 5s and 10s tests suggests that duration <= 20s is not enough to acquire a complete grain size distribution calculated on a representative number of particles.

Ultrasonication test

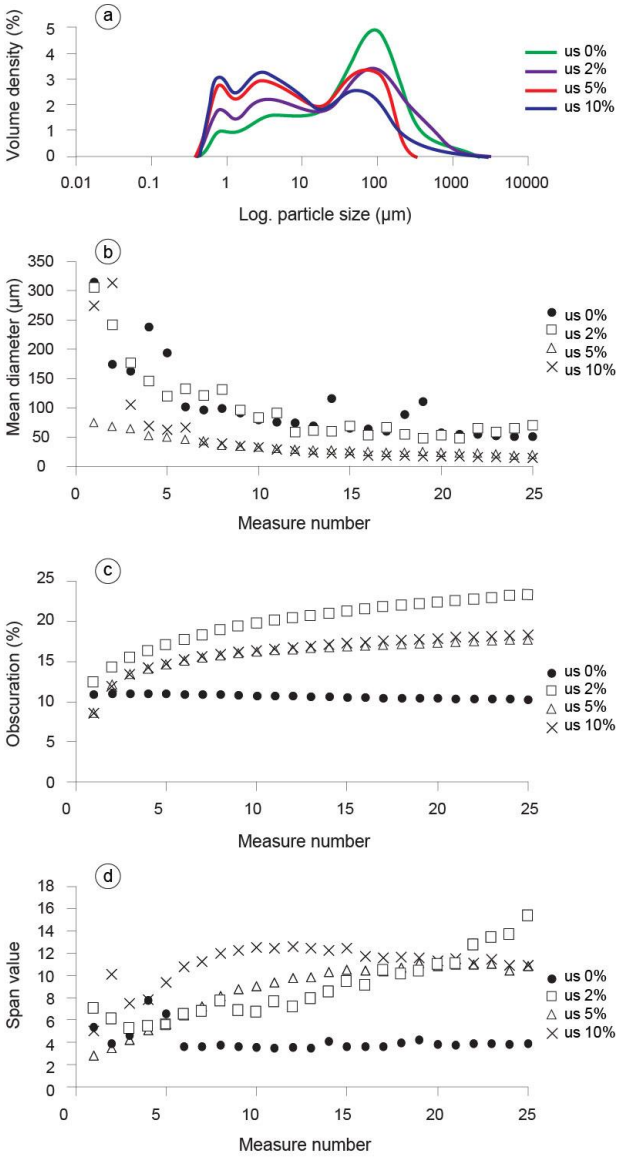

Figure S5: Volume density distribution versus log. particle size during ultrasonication test (a)t. Values of mean diameter (b), obscuration (c) and span (d).

Ultrasonication test consists of irradiating sample with different ultrasonication energies. We applied 0%, 2%, 5% and 10% ultrasound energy to test sample resistance through variations in mean

diameter, obscuration and span value. Results are firstly represented as volume density (%) versus log. particle size (Fig. S5a). Granulometric distributions show that the modal value shift towards fine particle size at increasing ultrasonication energy. (Fig. S5a). In accordance, even though mean diameter decreases at all the tested ultrasonication energies, the curve referred to the 0% ultrasonication test has, on average, higher mean diameters with respect to the 2%, 5% and 10% ultrasonication tests. This means that 0% ultrasonication test is less invasive than the others, where significative increase in fine particles causes increase in obscuration at ultrasounds >=2% (Fig. S5c). Related span values are reported in Fig. S5d.

Reproducibility test

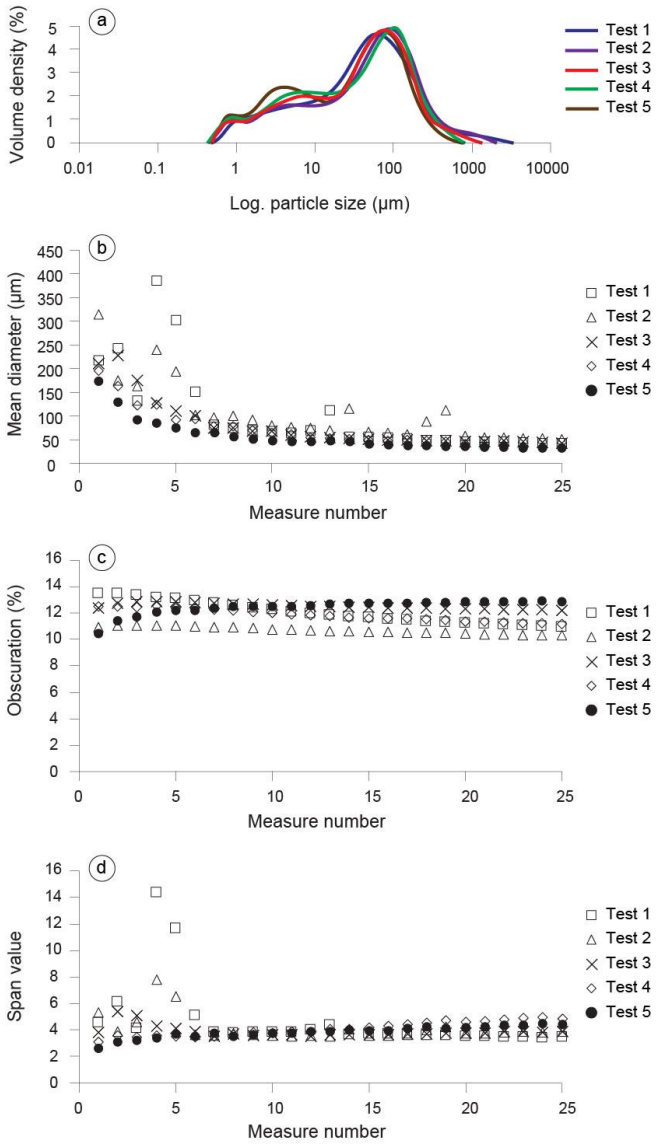

Figure S6: Volume density distribution versus log. particle size for the five reproducibility tests (a). Values of mean diameter (b), obscuration (c) and span (d).

The reproducibility test is performed to verify measure reproducibility. It consists of repeating the same analysis for five times with the same conditions of pump speed velocity (1700 rpm in this

case) and measurement duration (20s in this case) on identical sub-aliquots of the same starting granular material (Sample Fig. 1a). Results represented as volume density versus particle size almost correspond (Fig. S6a). Looking at mean values, some scattered value are recognisable mainly among the first measurements of tests 1 and 2 (Fig. S6b). Obscuration in Fig. S6c is stable for tests 2,3 and 4, decreases slightly during test 1 and increases slightly during test 5. This increase in finer particles is ascribable to sample disaggregation and fragmentation. Fig. S6d shows span values associated with the five tests. These values are constant in tests 3, 4 and 5 and display some outliers in tests 1 and 2, in accordance with the previous discussion.

Sample deterioration during analyses

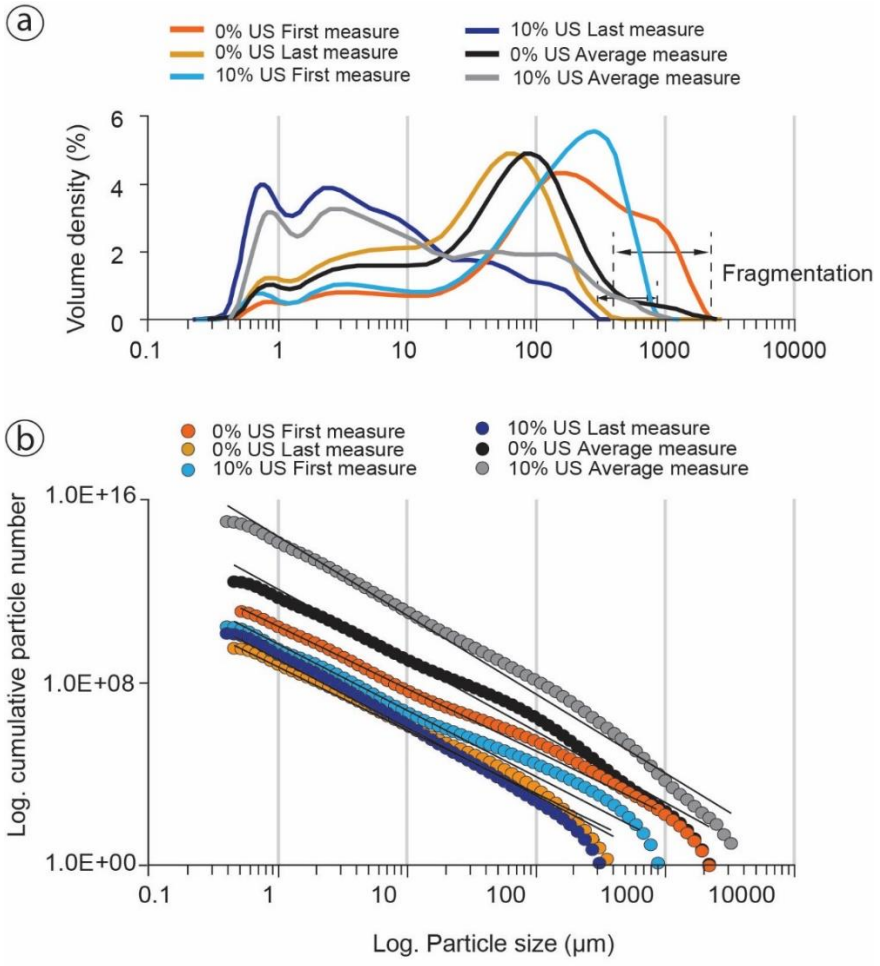

VALUES	0% US FIRST RUN	0% US LAST RUN	10% US FIRST RUN	10% US LAST RUN
D	2.76	2.87	2.80	3.37
R^2	0.99	0.98	0.99	0.99

Figure S7: volume density vs log. Particle size for wet laser granulometry (a) and log. Particle number vs log. Particle size for the same tests (b). In the table: related values of fractal dimension (D_3) and correlation coefficients (R^2).

The comparison between data of wet laser granulometry at 0% and 10% ultrasonication energy (first measure, last measure and mean values) is interesting to study the factors influencing sample deterioration during analysis, especially at high ultrasonication energies.

The first analysis by wet granulometry of the particle size distribution of sample FI1a without ultrasonication indicates the influence of the measurement time, during which sample fast recirculation through the dispersion unit can undergo fragmentation. Comparison between the granulometric curves obtained from the first and last run highlights significant differences, starting from the systematic shift of the latter towards finer size classes (Fig. S7a). The mean diameter obtained from the first run is six time coarser than the corresponding one in the last run (the modal size passes from 160 to 68.2 µm). The granulometric curve produced by averaging all 25 runs (black line in Fig. S7a) have a shape quite similar to that of the last run but shifted towards coarser size classes.

The use of 10% ultrasonication energy produced significant differences with respect to analyses without ultrasonication. The first run curve is very similar in the size classes smaller than 100 µm to the corresponding one without ultrasonication, whereas in the coarser size classes it shows the lack of coarsest particles and an increase of particle volume in the 100-600 µm size interval. Accordingly, the mean diameter passes from 315 to 185 µm, whereas the modal size passes from 168 to 291 µm (Fig. S7a). The last run curve (blue line in Fig. S7a) has a completely different shape from that obtained from the first run (light blue line in Fig. S7a). Bulk particle volume is dramatically shifted towards finer particles and, consequently, the modal size passes from 291 to 0.79 µm. Also in this case, the granulometric curve produced by averaging all 25 runs (grey line in Fig. S7a) has a shape quite similar to that of the last run but shifted towards coarser size classes.

Differences in granulometric curves produce a variety of fractal dimensions when cumulative data are plotted in a log-log diagram (Fig. S7b). Data averaged over the entire tests have the higher D-values, even higher than 3, when ultrasonication was used. On the other hand, first run data have the lower D-values, which are quite similar. The analysis of these values testify that the use of ultrasounds induces fragmentation and disaggregation of particles and thus is not recommended to preserve original samples in their best natural conditions.

7.3 Morphologi 4

Sample dispersion and areas of analysis

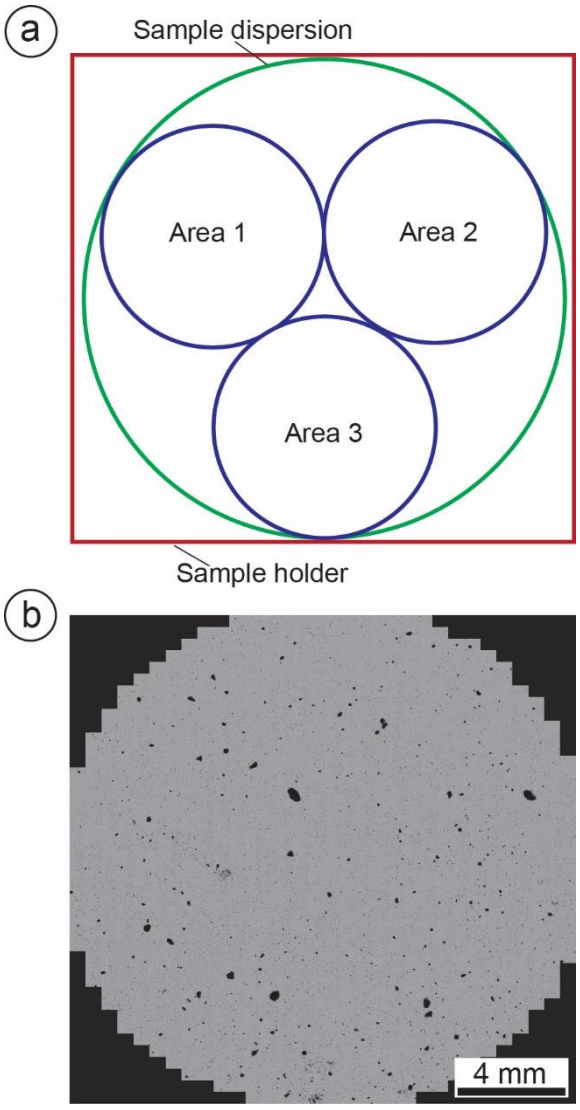

Figure S8: Areas analysed at the optical granulometry with indication of sample dispersion site and sample holder (a). Example image of sample dispersion at 2.5x with black points representing particles scattered over the sample lid (b).

Optical granulometry was performed on three circular areas of 380 mm^2 (r=11 mm) drawn on the same sample dispersion. We chose circular shape areas because Morphologi 4-ID work on circular areas. We chose to analyse more than one sector of the same dispersion to test measure reproducibility. Unfortunately, sample heterogeneity does not allow to obtain exactly the same results in the three areas analysed.

Calibration test

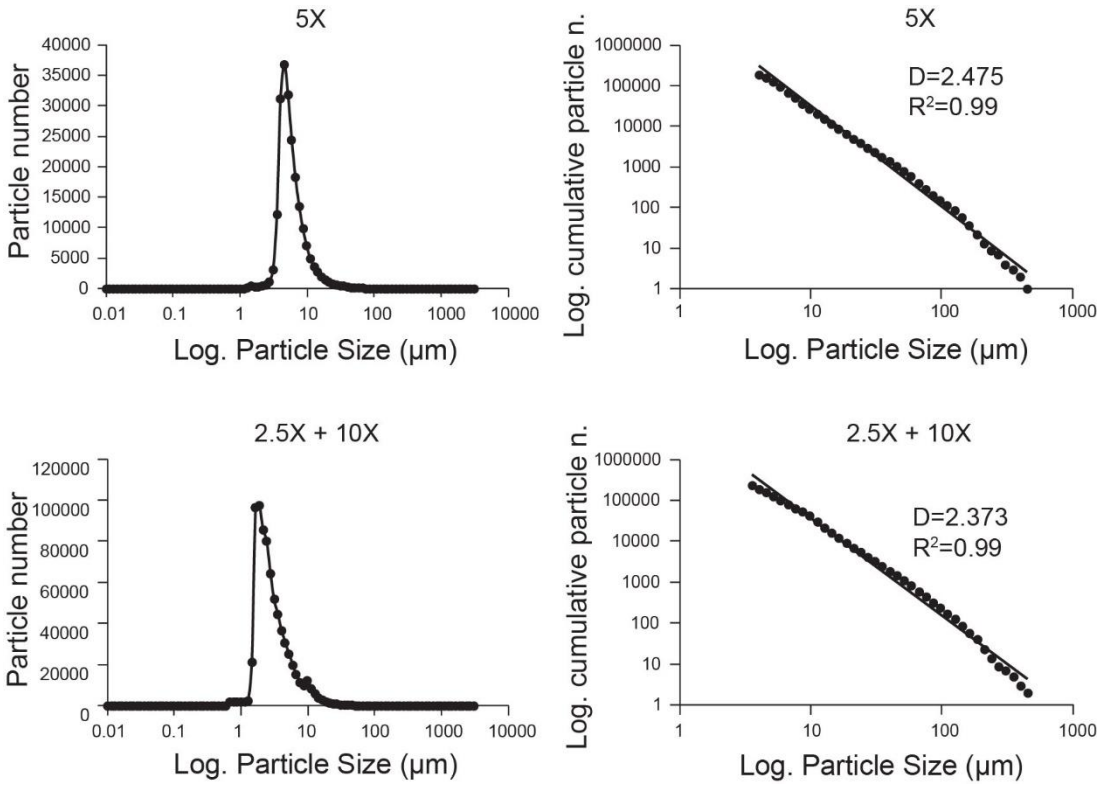

Figure S9: Frequency distribution of particles after calibration test with optical granulometer at two different magnifications (5x and 2.5+10x) (on the left). Log-log distribution of cumulative number of particles versus particle size at different magnifications and related values of fractal dimension and correlation coefficient (on the right).

Before measuring grain size distribution with optical granulometer, we made two tests to choose the best magnification to adopt in the analysis of our sample. The two tests are performed on the same area of the same sample dispersion. This gives us the possibility to compare results from the first test performed at 5x with results from the second test performed at 2.5x+10x. In fact, Morphologi 4-ID gives the possibility to merge automatically in an output data file results acquired with two different magnifications (e.g. 2.5x+10x). The use of merged magnifications gives the possibility to extend the investigated size range: in the first test with one single magnification (5x) we obtain a frequency distribution over the 1.27-438 µm size range; in the second test with two merged magnifications (2.5x and 10x), we obtain a frequency distribution over the 0.64-696 µm size range (Fig. S9). Nevertheless, this operation can cause some problems related with difficulties in merging data acquired at different magnifications. Due to this issue, frequency distribution can contain vertical drops where data acquired at different magnifications intersect. In our case, results obtained by plotting the cumulative number of particles versus particle size in a log-log diagram do not show significant differences between results acquired at 5x and 2.5x+10x. Moreover, no drops

are detectable into the frequency distribution of the second test. This suggests that results from both the two analyses are consistent and not biased. Basing on these assumptions, we decide to analyse our sample using the two merged magnifications (2.5x and 10x) that allow us to work over a wider size range.

Reproducibility test

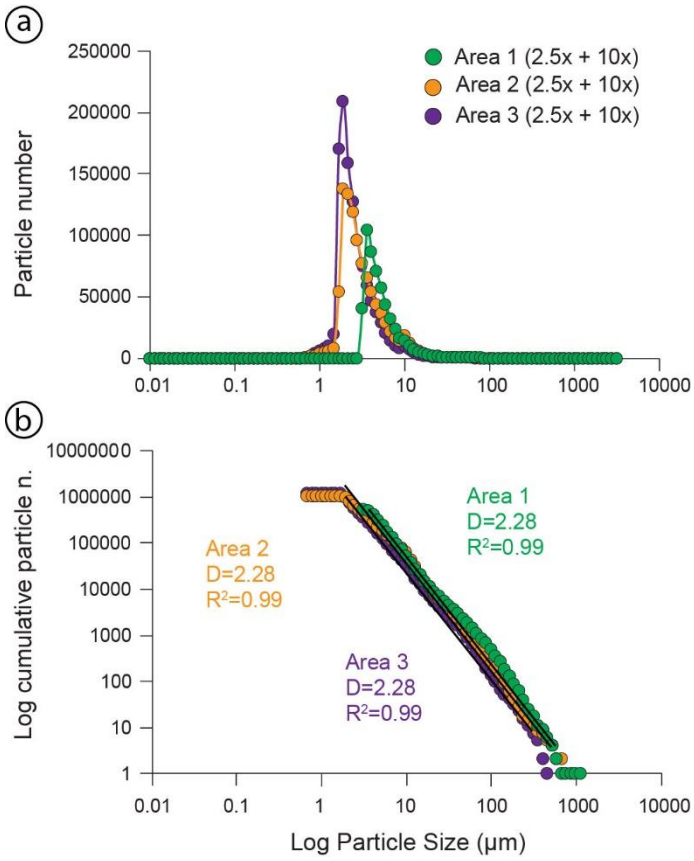

Figure S10: Frequency distribution obtained by analysing three different areas of the same sample dispersion (a) and corresponding values of fractal dimension obtained by plotting the cumulative number of particles versus particle size in a log-log diagram (b).

The reproducibility test for optical granulometry consists of calculating values of fractal dimension on three different areas (with r=11 mm) of the same sample dispersion. The number of particles analysed in each area is very high but changes significantly due to the casual dispersion of particles over the sample lid (i.e. each area reasonably contains a different number of particles and particles of different size). Despite these differences in particles distribution, results show that values of fractal dimension perfectly correspond (D_3=2.28) over the size ranges analysed. The analyses performed on areas 2 and 3, in the cumulative plot, have a lower fractal limit due to the occurrence of smaller particles with respect to area 1.

7.4 Multiscale image analysis

Scale factors for multiscale image analysis

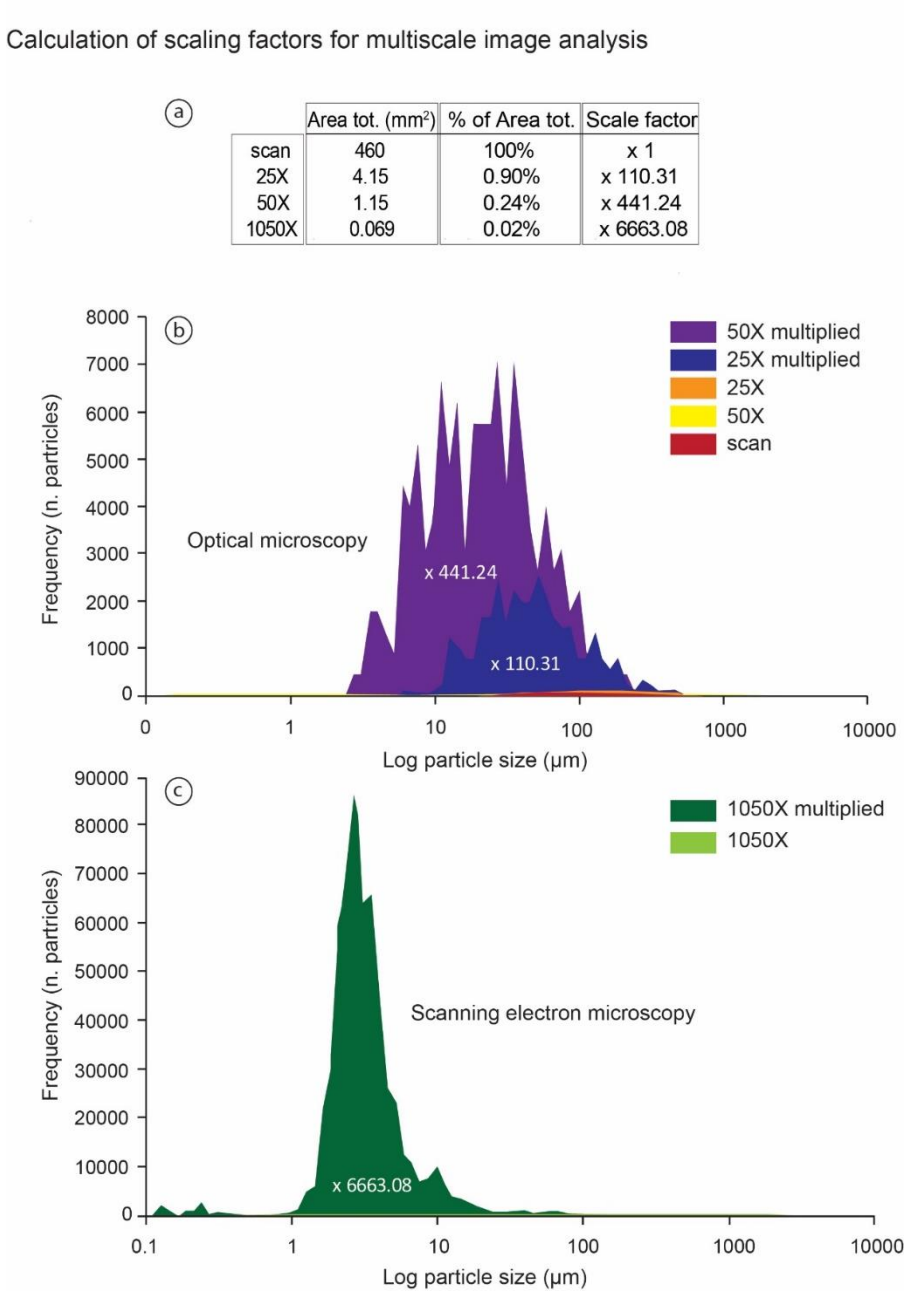

Figure S11: scale factors used in image analysis. Total area of thin section, area analysed (%) and scale factors for each magnification (a); frequency distributions from optical microscope (normal curves and curves multiplied for the scale factors) (b); and frequency distributions from SEM (normal curve and curve multiplied for the scale factor) (c).

Scale factors for image analysis are calculated firstly by dividing the total area acquired at each magnification for that occupied by the contoured clasts and then converting the obtain number in a percentage value. In Fig. S11a we report the total area calculated at each magnification, the area covered by clasts at each magnification (percentage value) and the corresponding scale factors. We represent number of particles acquired at each magnification multiplied for the corresponding

scale factor for scan image and optical microscopy (2.5x and 5x) in Fig. S11b, and for scanning electron microscope (1050x) in Fig. S11c.

Courses, seminars and conferences

First year

- "Giornata AIQUA", 19 Dicembre 2016, Firenze (It);
- "Study skills: English for Academic Purposes", Scuola di Dottorato in Scienze e Tecnologie, Università degli Studi di Parma. Lecturer Prof. Anila Scott-Monkhouse (UniPr);
- EGU General Assembly 23-28 April 2017, Vienna (AU);
- G. L. O. M. 7th July 2017, Parma (It).

Second year

- Seminar "Caratterizzazione dei materiali porosi" at FKV S.r.l., Bergamo (It);
- EGU General Assembly 8-13 April 2018, Vienna (AU);
- "From 1997 to 2016: Three Destructive Earthquakes Along the Apennine Fault System, Italy" 19th-22nd July 2017, Camerino (It);
- Short Course "Fault rock microstructures" Lecturer Prof. Renèe Heilbronner, Basel University, December 11 – December 12, 2017, Università di Parma (It);
- Structural geology school G. Pialli 2018. "Formation, deformation and geo-resources of Sedimentary Basins" Lecturer: François Roure IFP-EN. September 18-21, 2018 Università degli Studi di Perugia (It).

Third year

- Gruppo Nazionale di Geofisica della Terra Solida (GNGTS) 37° convegno nazionale, 19-21 Novembre 2018, Bologna (It);
- "Project Design and Grant writing" Lecturer Dr. Elisa Nicosia and Dr. Silvia Tavernini Università di Parma (It);
- Congresso nazionale SIMP-SGI-SOGEI 2019 "Il tempo del pianeta Terra e il tempo dell'uomo: le geoscienze tra passato e futuro", 16-19 Settembre 2019, Parma (It).

Publications on peer review journals

- **S. Cortinovis**, F. Balsamo, F. Storti (2019). Influence of analytical operating procedures on particle size distributions in carbonate cataclastic rocks, Journal of Structural Geology, Vol. 128, 103884 https://doi.org/10.1016/j.jsg.2019.103884.
- **S. cortinovis**, F. Balsamo, M. Fondriest, F. La Valle, G. Di Toro. Structural architecture and in-situ shattering along the active Monte Marine Fault, Central Apennines (Italy) (in preparation).
- S. Aretusini, **S. Cortinovis**, G. Di Toro, F. Balsamo. High velocity friction experiments on the Monte Marine fault gouges under fluid pressurized conditions: observations on mechanical data and experimentally produced microstructures (in preparation).

List of conference contributions

- "Microstructural investigations on carbonate fault core rocks in active extensional fault zones from the central Apennines (Italy)" EGU General Ass. 2017, 23-28 Aprile 2017 - Vienna – Cortinovis S., Balsamo F., Storti F. [Abstract + Poster].
- "Structural architecture and petrophysical properties of the cataclastic rocks along the Monte Marine extensional fault zone, Central Apennines (Italy)" From 1997 to 2016: THREE DESTRUCTIVE EARTHQUAKES along the Central Apennines fault system, Italy. July 19th-22nd 2017 International Field Trip – Cortinovis S., Balsamo F., Storti F. [Abstract + Poster];
- "Architecture and microstructural properties of the seismogenetic Monte Marine extensional fault affecting partially dolomitized carbonate rocks, Central Apennines (Italy)" EGU General Assembly 2018, 8-13 April 2018 - Vienna – Cortinovis S., Balsamo F., Storti F., Di Toro G. [Abstract + Poster];
- "Architecture and fault rocks of the seismogenic Monte Marine fault zone (Central Apennines, Italy" 37° Convegno Nazionale del Gruppo Nazionale di Geofisica della Terra Solida (GNGTS) , 19-21 Settembre 2018, Bologna – Cortinovis S., Balsamo F., Storti F., La Valle F., Fondriest M., Di Toro G. [Abstract + presentazione orale];
- "Structural architecture and microstructural properties of the seismogenic Monte Marine fault zone, Central Apennines (Italy)" Congresso Società Geologica Italiana, 16-20 Settembre 2019, Parma – Cortinovis S., Balsamo F., Fondriest M., La Valle F., Di Toro G. [Abstract + IES presentation];